EVALUATING THE EFFECT OF LAND-USE AND LAND-COVER CHANGE ON CLIMATE IN THE GREATER PHOENIX, AZ, REGION

by

MATEI GEORGESCU

A Dissertation submitted to the

Graduate School-New Brunswick

Rutgers, The State University of New Jersey

in partial fulfillment of the requirements

for the degree of

Doctor of Philosophy

Graduate Program in Atmospheric Science

written under the direction of

Dr. Christopher P. Weaver

and approved by

_____

_____

_____

_____

_____

New Brunswick, New Jersey

[May, 2008]

ABSTRACT OF THE DISSERTATION

Evaluating the Effect of Land-Use and Land-Cover Change on Climate in the Greater Phoenix, AZ, Region

by MATEI GEORGESCU

Dissertation Director:
Professor Christopher P. Weaver

The effect of land-use/land-cover change (LULCC) on the summer climate of one of the nation's most rapidly expanding metropolitan complexes, the *Greater Phoenix*, AZ, region, is investigated.

The initial part of this study evaluates the first-order effect of LULCC over *Greater Phoenix* using high-resolution (2-km grid spacing) Regional Atmospheric Modeling System (RAMS) simulations of three "wet" and three "dry" summer seasons. Experiments were carried out with two different landscape reconstructions for the region: a circa-1992 representation based on satellite observations and a hypothetical "pre-settlement" scenario where the anthropogenic landscape of irrigated agriculture and urban pixels was replaced with current semi-natural vegetation. The main findings are:

- The presence of extensive irrigated agriculture adjacent to the urban area dampens the regional-mean warming due to urbanization.
- The imposed LULCC produces a systematic increase in precipitation to the north and east of the city during dry summers.

Guided by these findings, the impact of the actual landscape evolution, using LULC reconstructions based on circa-1973, circa-1992, and circa-2001 satellite data, on the

Greater Phoenix regional climate was examined, and the relevant atmospheric dynamical processes investigated. The main findings are:

- From 1973 to 2001, areal coverage of irrigated agriculture declined and that of urban areas increased, resulting in significantly greater simulated regional-mean temperatures for the 2001 than for the 1973 LULC.
- As with the 1992 to pre-settlement comparison, precipitation is enhanced for the 2001 compared to the 1973 landscape during dry summers. In addition, rainfall enhancement relative to the 1973 LULC is increased for 2001 relative to the 1992 LULC.
- Heterogeneity in the surface fluxes produces preferentially located mesoscale circulations on most days that are stronger for the 2001 compared to the 1973 LULC, due to the increased planetary boundary layer (PBL) heating via enhanced turbulent heat flux.
- The effect of these stronger circulations is to warm and dry the lower part of the PBL and moisten the upper part of the PBL for 2001 relative to 1973.
- The precise physical pathway(s) whereby precipitation enhancement occurs with evolving landscape reveals a complicated interplay among scales that warrants future research.

Acknowledgements

I would like to express my deepest thanks to the best parents anybody could have. Without them, none of this, that, or the other would be possible. Their encouragement, support, love, and belief in me, got me through all this and I owe them more than words can express.

I would like to thank Prof. Christopher Weaver, my Ph.D. advisor. His tough love at critical moments proved decisive in the seemingly decades worth of time that I have been at Rutgers. I owe him much more than that, however, because upon the completion of my M.S. thesis, he did not have to take any students – but I got lucky.

Dr. Gonzalo Miguez-Macho is likely as familiar with my work as anyone. His expertise and personal assistance has been absolutely invaluable and this work would not have been complete without his help.

I would like to thank Prof. Tony Broccoli for all of our great talks, about science or about sports, through the years. Those particular times of levity I will remember with special fondness.

Special thanks to all my committee members - Jim Miller, Gera Stenchikov, Tony Broccoli, Gonzalo Miguez-Macho, and Chris Weaver.

Table of Contents

List of Tables

List of Illustrations

Chapter 1 - Introduction

Assessment of anthropogenic influences on climate has primarily focused on changes in globally averaged metrics (e.g., temperature, tropospheric radiation balance) resulting from emissions of well-mixed greenhouse gases (IPCC, 2007). However, sub-global-scale forcings and their impacts are also important. For example, the spatial gradient of heating on regional and local scales is responsible for driving atmospheric circulations that affect regional weather and climate. In addition, understanding regional climate change is important in its own right, as this is the scale of many impacts of concern for human and natural systems. Anthropogenically induced changes in climate at regional scales include the effects of both global-scale anthropogenic forcing, e.g. due to increases in greenhouse gas concentrations, and any regional-scale anthropogenic forcings. Consequently, in monitoring and anticipating the fingerprint of climate change, we must also account for these contributions from sub-global-scale forcings. This thesis will address this issue through analysis of the regional-scale impacts of one of the most important regional climate forcings: land-use/land-cover change (LULCC).

Recent work has emphasized the importance of LULCC as a contributor to anthropogenic climate change across the globe (Feddema, 2005) while at the same time suggesting that accurately assessing the impact of LULCC on climate requires a perspective appropriate to this forcing. Due to the heterogeneous nature of regional climate drivers, such as the patchwork of surfaces resulting from landscape alteration, in contrast to the effect of well-mixed greenhouse gas concentrations such as CO_2, a focus only on globally averaged metrics can lead to overlooking important regional effects. For example, it has been pointed out that the traditional metric of globally averaged,

tropospheric radiative forcing is not well-suited to capturing the full effects of LULCC (NRC, 2005; Davin et al., 2007), as such an approach does not adequately account for the modification of the surface energy balance, biogeophysical impacts, large contrasting regional signals that average out to a relatively small global effect but are nevertheless significant regionally (Myhre and Myhre, 2003; Feddema et al., 2005), circulation changes (Matsui and Pielke, 2006), and teleconnections to remote regions (Pielke et al., 2002). Consequently, regional-scale studies that quantify the effects of LULCC and other regional climate forcings through a regional lens have the potential to improve our overall understanding of the full spectrum of anthropogenic climate change, its impacts and consequences.

The effects of LULCC in urban/sub-urban areas, or areas that are rapidly being developed and converted in this way, are particularly important, because this is where the majority of the world's population resides (Jin and Shepherd, 2005) (and the percentage is growing (Arnfield, 2003)). Increased scientific emphasis on these areas is required to address the wide-ranging implications, for sectors like public health (e.g., heat and air pollution), water resource management (e.g., high water demand and extensive impervious surface), and conservation (e.g., habitat fragmentation and loss in the face of development), of continued urbanization.

Inhabitants of large and expanding urban complexes located in arid and semi-arid regions are especially vulnerable to any changes in climate (either globally or regionally driven), due to reliance on increasingly limited water supplies. For example, the state of Arizona recently developed its first drought plan, hoping to mitigate economic and societal effects of current and anticipated future droughts (Jacobs et al., 2005).

Motivated by these issues, therefore, the focus of this work will accordingly be to quantify the effect of LULCC on regional climate over a rapidly urbanizing, water-stressed, metropolitan complex. This research blends numerical modeling with remotely sensed observations from NASA satellites to address a trio of research objectives:

(1) to characterize, using satellite data, the LULCC in the *Greater Phoenix,* Arizona area as a result of the explosive growth and urbanization that occurred between the middle 1970's and today;

(2) to quantify, using a high-resolution regional climate model, the impacts of LULCC on local and regional weather and climate, with a particular emphasis on changes during the summer season, when the North American Monsoon System (NAMS) is active;

(3) to uncover the specific land-atmosphere interactions influenced by differential landscape change and the pathways of interaction with the large-scale NAMS environment to produce these simulated impacts on local and regional weather and climate.

The *Greater Phoenix* region is the focus of this study. *Greater Phoenix* is located in the semi-arid Sonoran Desert, has a regional population of nearly 4 million, and was recently ranked as the 14th largest metropolitan city in the U.S. (GP Regional Atlas, 2003). This population increase, in conjunction with shifts in economic priorities from agriculture to technology, has driven rapid territorial expansion of urban and suburban land use types (Knowles-Yanez et al., 1999). The potential impacts of this development raise concerns about future water supplies (Grimm and Redman, 2004) and anthropogenic air pollution (Lee et al., 2003). Understanding the consequences of this

major conversion of the land surface on atmospheric processes, the hydrologic cycle, and regional climate, is a key issue, as accelerating sprawl continues not only in Phoenix, but throughout the U.S. and the world.

Perhaps the most important climate variable in any arid or semi-arid region is precipitation. In the Phoenix area, a significant amount of the annual precipitation (about 40%) falls during one period of the year, that of the NAMS (Adams and Comrie, 1997). This 3-month period (July, August, and September) is characterized by a large-scale circulation pattern responsible for enhanced moisture transport from the tropical eastern Pacific, Gulf of California, and to a lesser extent, the Gulf of Mexico. This moisture transport, coupled with intense heating of the land-surface, serves to decrease atmospheric stability and causes frequent convection. Because the bulk of NAMS rainfall is convective, it is highly variable in space and time, and the response of the surface- and sub-surface hydrology (e.g., flash floods) is extremely sensitive to this. Changes in either the mean or variability of this rainfall have a strong potential for impacts on water resources and the public. This sector is already increasingly stressed as Phoenix' development, combined with the climatological scarcity of water, poses a growing challenge for water management. Therefore, one major focus of the work is to assess whether mean rainfall, or its variability, might have been impacted by LULCC in this region (and may continue to be impacted), specifically by understanding how changes in differential land-use patterns over time may affect the mechanisms that control convective precipitation.

The assessment of the effect of LULCC over the *Greater Phoenix* area in this work is based on a number of experiments with a numerical model. These experiments make use

of different sets of landscape reconstructions based on LULC observations from NASA satellites. In addition, to distinguish whether a particular landscape-induced signal in the meteorology operates during dissimilar large-scale settings, we simulate both "dry" and "wet" NAMS seasons, i.e., by experimental design, we simulate periods both when the large-scale signal is weaker, and when it is stronger. The issue of scale interaction is an important one, and we made an effort to ensure that the clear identification of the local/mesoscale landscape signal is distinguishable from the forcing of the large-scale.

In Chapter 2, we discuss the general control of the surface on local/regional weather and climate, review the climatology of the *Greater Phoenix* area and the evolution of the NAMS circulation, and highlight the specific land-atmosphere interactions of urbanized regions, including their influence on the thermal field and impact on precipitation. The integration of LULC satellite data into our numerical model and the evolution of the *Greater Phoenix* landscape with time, from the 1970's through today, are examined in Chapter 3. The description of the model and the experimental design, including the selection criteria for the years of simulation, and underlying assumptions made, are addressed in Chapter 4. Chapter 5 discusses the evaluation of the model's performance, with an emphasis on its ability to reproduce the regional climate with respect to observations of temperature, dew-point, and precipitation. In Chapter 6, the possible existence of a first-order impact of the area's landscape alteration on regional climate, through an investigation of observed circa-1992 LULC versus a hypothetical, "pre-settlement," landscape is assessed. The impact of the area's known evolving landscape from the early 1970's through today, and the role of the large-scale in modulating this impact, is addressed in Chapters 7 and 8. In Chapter 7, the effect of increasing urban

land in conjunction with decreasing plots of irrigated agriculture is examined through their collective and individual impacts on the surface radiation balance, while their impacts on atmospheric dynamical processes and convection, and the interactions between the turbulent-, meso-, and large-scale dynamics over the monthly timescale, are presented in Chapter 8. Finally, conclusions, implications and limitations of results, and possible future work, are discussed in Chapter 9.

Chapter 2 – Background

2.1 - Surface Energy Balance

The major conduit between the land surface and overlying atmosphere is the planetary boundary layer (PBL). Changes of the underlying landscape modify the surface energy and moisture budgets. These are in turn responsible for adjustments of fluxes of heat, water, and momentum to the overlying atmosphere, influencing key thermodynamic and dynamic properties of the air with important implications for convective activity. Below, we review the concepts of net radiation balance and net radiative budget. These two themes will be considered in the context of *Greater Phoenix'* landscape evolution in the succeeding results chapters.

The net flux of radiation at the earth's surface is determined by the balance between net fluxes of shortwave and longwave radiation. The total amount of absorbed surface shortwave radiation may be described as:

$$SW_{net} = SW\downarrow - SW\uparrow = (1-\alpha)SW\downarrow \qquad (1)$$

where SW_{net} represents the net surface shortwave radiation; the down and up arrows represent the downwelling and upwelling components, respectively; α is the representative material albedo and the quantity (1-α) represents the fractional component of shortwave radiation that is absorbed. The net longwave radiation balance at the surface may be described as:

$$LW_{net} = LW\downarrow - LW\uparrow = LW\downarrow - \varepsilon\sigma T^4 \qquad (2)$$

where LW_{net} represents the net longwave radiation; the down and up arrows represent the downwelling and upwelling components, respectively; ε is the representative material emissivity (for any real body the emissivity is less than 1); σ is the Stefan-Boltzmann constant; T is the absolute temperature of the surface of interest. The net surface radiation balance is given by the balance between net shortwave and net longwave radiation:

$$R_n = SW\downarrow(1-\alpha) + LW\downarrow - \varepsilon\sigma T^4 \quad (3)$$

where R_n refers to the net balance of incoming radiation received at the surface and all other variables are as described previously.

Accurately accounting for net radiation received at the surface, and its components, is critical as this energy in turn drives the weather and climatic fluctuations that most affect the habitation of the earth. The radiation received at the surface is redistributed into three separate components. Incoming radiation may be used to evaporate water, while a significant remainder is lost to the atmosphere as sensible heat. Additionally, net incoming radiation may be transferred downward into the earth's subsurface layers. In the absence of snow or ice, as may be expected during mid-latitude summer, the surface radiation balance may be written as:

$$R_n + L + H + G = 0 \quad (4)$$

where L represents latent heat flux (accounting for both direct evaporation of water and plant transpiration), H represents the sensible heat flux, and G is the soil heat flux.

Consequently, changes in land use will affect the surface radiation balance due to changes in both net shortwave and longwave radiation, thereby altering one or more of the variables in (4). Through the ensuing transport of heat and moisture, these changes influence key thermodynamic variables, such as potential temperature (θ), equivalent potential temperature (θ_e), Convectively Available Potential Energy (CAPE), the vertical stability profile, and the timing and location of convective activity. The proper representation of the land surface and its two-way interaction with the overlying atmosphere is thus essential for appropriately accounting for land-atmosphere interactions and their influence on local, regional, and large-scale climate (Pielke, 2001).

One of the most critical parameters that determines the absorption and partitioning of incoming radiation received at the surface is albedo, i.e., α in (1) and (3) above, as it establishes the amount of absorbed radiation. Consequently, understanding how albedo changes over time with LULCC, or across a heterogeneous, human-modified landscape, and accurately specifying this in regional and global climate models (RCMs and GCMs), is necessary for an improved understanding of land-atmosphere interactions and studies about the effects of LULCC. In addition, as will be discussed in more detail in later chapters, it is primarily through albedo changes that the specific impacts of LULCC in the *Greater Phoenix* area are felt, due to the dry, sparsely vegetated nature of the region. Therefore, here we briefly highlight a few recent examples of studies that address the issue of accurately representing albedo in climate models, particularly for arid and semi-arid regions.

Albedo varies with time of day, year, location, and in the case of soil, on its wetness and thus on its texture as well. Its representation in climate models has been the subject

of considerable recent advances as GCM development has benefited greatly from a new abundance of satellite data. It is generally accepted in the climate community that the global-mean albedo effect of anthropogenic LULCC in the industrial era is negative (i.e., an increase in albedo leading to net decrease in absorbed radiation), though relatively small (e.g., Hansen et al., 1998; Houghton et al., 2001; Feddema et al., 2005), and also relatively uncertain: IPCC [2007] affirms that globally averaged forcing resulting from albedo change due to total anthropogenic LULCC alone has a best-guess estimate of -0.20 $\pm$ 0.20 Wm^{-2}, and it further states that there is only "moderate confidence" in these values.

This uncertainty exists, in large part, because of the high sensitivity to assumptions about the albedos of different LULC types. For example, Myhre et al. (2005) used a radiative transfer model and Moderate Resolution Imaging Spectroradiometer (MODIS) data to study the impact of global anthropogenic vegetation change on global-mean surface albedo and found a net radiative effect weaker than -0.1 W m^{-2}, a value lower than most published results, and one they attribute to a generally reduced value of cropland albedo than previously thought. Myhre and Myhre (2003) highlight the importance of cropland albedo sensitivity by specifying three different values (0.15, 0.18, and 0.20) and achieving a range in global-mean radiative forcing of 0.23 W m^{-2}.

Large differences in albedo values specified and calculated within different models can be found when considering specific regions. For example, Wei et al. (2001) evaluated albedo over the desert areas of Africa calculated by two land surface models, the Biosphere-Atmosphere Transfer Scheme (BATS) and the NCAR Land Surface Model (LSM), and compared them to albedo maps developed from Advanced Very High

Resolution Radiometer (AVHRR) satellite data. Both land surface models had a tendency to overestimate the summer season albedo of 0.26, as observed by AVHRR, but beyond that there were large differences between the two models, with LSM having a value of 0.29 and BATS 0.33. Zeng et al. (2002) noted that introducing the Common Land Model (CLM) into the NCAR Community Climate Model (CCM) reduced albedo biases over the Australian shrublands, contributing to the elimination of surface temperature biases as large as 5ºC. Zhou at al. (2003) compared albedo values from MODIS with those of CLM and found some of the largest discrepancies in simulated albedo over desert and semi-desert regions during summer, when CLM displayed a negative bias of 0.1 in the shortwave part of the spectrum and a similar negative bias in the near-infrared.

These are just a few examples that highlight the continued uncertainty involved in obtaining appropriate representations of global and regional albedo in models and the resulting sensitivity of the surface radiation balance. In this context, a brief description of the modification of albedo (and additional biogeophysical parameters) from the default RAMS values to more accurately reflect those appropriate to the *Greater Phoenix* region is provided in Chapter 3, during the discussion of the incorporation of satellite data into RAMS.

2.2 - The Role of Land-Surface Heterogeneity

Beyond regional-mean values, properly accounting for the fine-scale variability of albedo and other land-surface characteristics is important, because such heterogeneity can drive the formation of atmospheric circulations that can exert a strong influence on local and regional climate. For example, Pielke et al. (1993) showed how surface heterogeneity

on length scales smaller than the local Rossby radius of deformation can lead to a non-linear atmospheric dynamical response. A well-known example of this phenomenon is the sea breeze circulation, driven by the pressure gradient between warmer land and cooler ocean, but there have also been a number of studies illustrating how similar diurnal mesoscale circulations can occur over inland heterogeneity due to gradients in LULC. Here we briefly review some of these findings since, as will be discussed in later chapters, the heterogeneity associated with the presence of *Greater Phoenix* creates such mesoscale circulations that influence the vertical transports of heat and moisture from the PBL into the free troposphere and consequently affect the vertical thermodynamic structure of the atmosphere.

Recent observational analysis using satellite data has shown how clouds preferentially form over patches of agricultural land in southwestern Australia (Lyons, 2002; Ray et al., 2003) and the Amazon (Negri et al., 2004). The pioneering work of Avissar and Pielke (1989) justified the need to account for subgrid-scale variability in land-surface parameters in GCMs to more accurately calculate mean surface fluxes over the model grid cell, proposing the "mosaic of tiles" type of land-surface parameterization. This type of parameterization is unable to account for the non-linear impacts of this surface heterogeneity on atmospheric dynamics, however, and higher-resolution simulations are required to capture the mesoscale circulations and their resulting impacts on clouds and precipitation as seen in the observations.

For example, using an idealized set of landscapes and high-resolution RAMS model simulations, Avissar and Liu (1996) found that precipitation is strongly affected by the heterogeneity in landscape structure. Specifically, they found that initial triggers of

mesoscale circulations favor cloud and precipitation formation over the initially dry part of the domain, where sensible heat fluxes are greatest, creating a negative feedback that dampens the initial soil moisture perturbation. The conventional wisdom derived from a number of similar modeling studies with idealized landscapes suggested that landscape-induced mesoscale circulations were likely only of local importance and only at certain very limited times when the large-scale background winds were extremely weak (see for example, Zhong and Doran, 1998). However, using high resolution RAMS simulations with a realistic, observationally derived landscape representation for the U.S. Southern Great Plains, Weaver and Avissar (2001) confirmed that observed clouds and rain matched up with the locations of the model-simulated mesoscale circulations even on days when background wind speed was large. Now, there is an increasing body of evidence suggesting that land-atmosphere interactions responsible for naturally occurring mesoscale circulations have important impacts at local and larger scales (e.g., Weaver and Avissar, 2001; Pielke, 2001; Baidya Roy and Avissar, 2002; Weaver, 2004a; Weaver, 2004b; Pielke et al., 2007).

2.3 - Urbanization as a Particular Example of Regional LULCC

As already emphasized in the Introduction, human-induced conversion of the landscape may be of greatest importance over urban/sub-urban areas, as this is where half of the world's population resides (Jin and Shepherd, 2005) and where present estimates suggest population will increase even further (Arnfield, 2003).

The urban heat island (UHI) is an extreme manifestation of LULCC that results from the modification of the energy balance terms discussed above. Historically, it has been illustrated as a near-surface air temperature excess in built-up areas relative to rural

environments. The UHI was first documented as a temperature difference between the city and the rural environment by Howard (1833). The term describing this temperature contrast - UHI - was defined by Manley (1958). Bornstein (1968) was the first to document the UHI over New York City, citing observational evidence of a greater than 3 ºC near-surface temperature excess (from near sun-rise) over the central urban area relative to the northern suburbs. The increased urban temperature, he noted, was a maximum near the surface and, on average, decreased to zero at 300 m, although on select days the UHI effect was observed to reach heights greater than 500 m.

Studies of the UHI have described a wide array of impacts, including evidence of increased mean and maximum diurnal temperature and a decrease in the diurnal temperature range (DTR) (Gallo et al., 1996; Gedzelman et al., 2003) and the modification of rainfall pattern and amount over and downwind of major metropolitan areas (Huff and Changnon, 1973; Shepherd et al., 2002; Shepherd and Burian, 2003; Burian and Shepherd, 2005). Arnfield (2003) presents an extensive review of urban climate research during the previous two decades and highlights some of the most relevant issues in the field today, including the still emerging definition of a surface, rather than near-surface, UHI, and the concerns about spatial and temporal inconsistencies of observation sites. Fine-scale heterogeneity in the thermal properties of urban surfaces, such as the existence of cool islands due to irrigated areas such as lawns and parks (Spronken-Smith and Oke, 1998), effects of paved areas and non-irrigated green space, and the radiative and dynamic interactions with neighboring surfaces are complicating factors in the numerical representation of the urban canyon. For example, Avissar (1996) used a high-resolution coupled land-atmosphere model to show the non-

linear response of turbulent fluxes and dynamical processes to linear changes in urban vegetation fraction. Finally, some investigators have suggested that the observed global surface temperature increase during the 20th century is in part the result of urbanization (Kalnay and Cai, 2003; Cai and Kalnay, 2004). The global impact of this aspect of human-induced landscape modification, however, remains a topic of significant uncertainty (Trenberth, 2004; Vose et al., 2004; Parker, 2006).

Due to computing restrictions the modeling community has been faced with a trade-off between assessing the local and short-term, versus the regional and longer-term, effects of urbanization. On the one hand, urban climate assessments that include full geometric representation, resolve the vertical structure of the urban core, and integrate the contributions of direct and diffuse radiation, solar shading, and the influence of the urban canyon effect, yield important insights into the urban footprint on the surface radiation balance, local temperatures, and fine-scale dynamics (e.g., Sailor and Fan, 2002). However, the complexity and resolution of such models has so far precluded investigations beyond that of the local spatial and short temporal scales. In this thesis work, we have attempted to push the limits of this trade-off by carrying out relatively high-resolution (2 km horizontal grid spacing) simulations for relatively long timescales (monthly) to more fully capture the longer-term interaction of the urban environment with atmospheric processes.

2.4 - Greater Phoenix' Landscape Evolution

There have been a number of recent modeling studies focusing on the impacts of historical LULCC on climate, using a variety of landscape reconstruction methods, at large- (Baidya Roy et al., 2003; Wang et al., 2003; DeFries et al., 2002) and regional

(Chase et al., 1999; Marshall et al., 2003; Marshall et al., 2004; Twine et al., 2004; Schneider et al., 2004; Wichansky et al., 2008) scales. All of these studies emphasize the close coupling between changes in the land-surface over time and atmospheric processes. This work helps provide a context for the investigation presented in this thesis, of the specific impacts of historical changes in the landscape of *Greater Phoenix* over time.

Rapid population increase and accompanying urbanization have been a common theme of Maricopa County throughout the twentieth century. Although the first permanent settlement of Phoenix took place in 1868 (Hsu, 1984), the town's population remained low (i.e., not exceeding six thousand inhabitants) until early the following century. Between 1900 and 1950, when agriculture became the mainstay of the area's growing economy, Phoenix' population grew from an estimated 5,544 to 106,818 inhabitants (Knowles-Yanez et al., 1999). The continued surge in both federal and private funding led to increasingly diverse economic priorities during the latter half of the century as construction, technology, and tourism became the area's economic foundation at the expense of a decrease in agricultural production. The low price of land, alluring tax rates, booming economic status, and attractive "valley" climate served as chief factors in the unrelenting growth spurt of Phoenix as the city's population increased to nearly 1.2 million by 1995 (Knowles-Yanez et al., 1999). As the population of Phoenix has begun to plateau, growth of adjacent satellite cities have started to carry a greater weight of the metropolitan area's continued expansion. For example, from 1950 to 1990 Glendale grew from a population of 8,179 to 147,864 (Knowles-Yanez et al., 1999), increased further by an additional 48% to nearly 220,000 people by 2000, and as of 2005 has reached nearly 240,000 inhabitants (U.S. Census Bureau, 2005). Located immediately

west of Phoenix Glendale has become Arizona's fourth largest city and serves as the archetype of the area's inexorable expansion in areas primarily to the northwest, northeast, and southeast of the original city center.

Initially, Phoenix's land was primarily agricultural. While the designated urban area expanded from an estimated 20 km^2 to 306 km^2 from 1912-1955, agricultural land increased from 1,026 km^2 to 1,583 km^2. Territorial coverage of agricultural land-use shows a varied response with time, increasing through the 1950's and 1960's, finally peaking in the mid 1970's and eclipsing 1,800 km^2 before decreasing toward 1912-like extent beginning in the 1980's (Knowles-Yanez et al., 1999). Estimates of increases in urban area, however, depict an exponential trend during the long-term period between 1912 and 1995 (Jenerette and Wu, 2001). With changing economic priorities, reliance on agriculture as a financial resource gave way to a shift of land use practices (Jenerette and Wu, 2001). During the first half of the century, expansion of the urban and suburban area occurred largely at the expense of decreases in the agricultural area immediately surrounding the urban core, while agricultural development and expansion continued at greater rates along the outer fringes of existing plots, serving to replace the pre-existing natural desert and shrubland cover. Throughout the second half of the century, urban and suburban development shifted toward increased conversion from formerly desert landscapes as opposed to agricultural areas (Grimm and Redman, 2004). Knowles-Yanez et al. (1999) estimate that between 1935 and 1955 agricultural land accounted for nearly 83% of all newly converted urban territory, but, in the subsequent pair of twenty-year periods (1955-1975 and 1975-1995), 60% and 58%, respectively, of all new urban land

originated from formerly desert landscape. This trend continues today, most noticeably in the northern and western regions of the *Greater Phoenix* area.

Chapter 3 provides a satellite-imagery-based look at this evolution of the *Greater Phoenix* landscape, over the timescale of the last three decades.

2.5 - Greater Phoenix' Climatology and NAMS Evolution

Phoenix and its surrounding satellite cities are located in the fairly low-level Salt River Valley, a broad and relatively flat plain. The city of Phoenix (elev. 344 m) is surrounded by rougher and higher terrain in all directions, including Camelback Mountain to the immediate north (elev. 824 m), the Sierra Estrella Mountains to the southwest (elev. 1400 m), the White Tank Mountains further to the northwest (elev. 1250 m) and the Superstition Mountains (elev. 1500 m) situated to the east. This characteristic geographic configuration coincides with nearly year-round high pressure and results in a high measure of percent of possible sunshine.

The region's climate is distinguished by its hot and relatively humid (compared to other Phoenix seasons) summers, mild winters, and two distinct rainfall seasons. The first such rainy season stretches from about November through March, with precipitation dominated by the passage of mid-latitude cyclones associated with the southern transit of the extra-tropical storm track. The mean monthly rainfall average at Sky Harbor International Airport peaks during December. Subsequently, the number of average days with at least a trace of precipitation decreases before bottoming out in June, the month with the highest average of percent possible sunshine out of the entire year (94%). During the July-August-September (JAS) time period, the *Greater Phoenix* area sees its second rainfall season. During this time the region is subjected to the influence of the

NAMS. Increased convective activity and rainfall occur and the combined effects of heating, increased moisture levels (due to the circulation's large-scale transport) and increased wind speeds makes summers particularly inhospitable (Balling and Brazel, 1986). Following the weakening influence of the monsoon circulation in September is a period of cooler temperatures and decreased rainfall activity. A quantitative rainfall assessment of the region is presented in Chapter 4.3.

This thesis is focused on the NAMS season because it is during this time of year when the atmospheric effect on the public sector is most adverse (i.e., excessive heat and locally intense and flood-producing rainfall). In addition, due to the convective nature of precipitating systems during this time of year, it is during the NAMS season when the surface forcing, initiated by intense heating of the land-surface, is expected to have the greatest impact on the atmosphere. Alternatively, the winter rainfall peak is dominated by the large-scale extra-tropical storm track, hindering our ability to distinguish a landscape-induced signal. Our hypothesis was that, during times of heavy and widespread rainfall (whether winter vs. summer or, alternatively, wet vs. dry summers), the regional contribution of the landscape will be more difficult to distinguish, given the large-scale forcing and atmospheric (as opposed to surface) control of precipitation, consistent with expectations based on previous work (e.g. Findell and Eltahir, 2003; Koster et al., 2004; Anyah et al., 2007).

Here, we briefly discuss the initiation and evolution of the monsoon circulation. Adams and Comrie (1997) provide a comprehensive review of the topic and much of the discussion below stems from their work.

The geographic boundary of the region affected by the NAMS circulation has been cited differently by various researchers. The climatic impacts are greatest in northwest Mexico, southern Arizona, and New Mexico, although monsoon literature has shown a significant geographical bias centered over the southwest (SW) U.S. (Adams and Comrie, 1997). In reality, the domain bounded by circulation changes resulting from NAMS extends westward into the Pacific Ocean, reaches southward toward the mouth of the Gulf of California, and stretches as far east as the central Plains and Gulf of Mexico (Adams and Comrie, 1997). The lowlands of northwestern Mexico, Arizona, California, and Nevada, and in particular, the Mojave, Sonoran, and Sinaloan deserts (*Greater Phoenix* lies in the northeastern reaches of the Sonoran desert), serve as a critical collective triggering point for the initiation of the monsoon circulation. The high sun angle and relatively cloud-free early summer heats the land surface, aiding in the formation of a surface thermal low that generally resides along the NV-CA-AZ border.

The development of a surface area of low pressure aids in the seasonal wind reversal responsible for the shift in air flow from a predominantly westerly to a primarily southerly direction. Accordingly, the circulation about the low assists in the transport of low-level moisture from the nearby Pacific Ocean and Gulf of California. Tropical easterly waves crossing south of the Gulf of California provide an important additional source of water vapor for the region. It is important to note that channeling of water vapor from the aforementioned source regions is not a continuous phenomenon but instead occurs on the synoptic timescale. Therefore “surges” (Brenner, 1974; Adams and Comrie, 1997) of water vapor transport, the majority of which occurs below 700 mb, are accompanied by intervening dry periods, with very low dew-point temperatures and,

hence, low relative humidity. Therefore, while summer season dew-point temperatures can often exceed 20°C the temporal extent of these moist episodes is intermittent and not characteristic of the entire season.

Although the large-scale circulation is principally responsible for broad atmospheric water vapor transport, predictability of summertime convective activity is complicated by the influence of the region's rough terrain. The elevated Mogollon Rim, situated to the northeast of *Greater Phoenix*, receives significantly more rainfall than the low-lying desert regions to the southwest due to terrain-induced flow modification. The diurnal peak in convective activity over the elevated terrain, however, occurs during the mid-afternoon hours, while rainfall occurring in and around Phoenix displays a maximum frequency during the nighttime (Balling and Brazel, 1987). Hales (1977) suggested that pockets of cool air from high terrain (i.e., along the Mogollon Rim) thunderstorms, originating from their outflow boundaries, flow into the valley and offer the opportunity for enhanced convection provided there is sufficient low-level dynamic triggering along the valley floors.

Synoptic-scale activity is modulated by seasonal and interannual variability of the NAMS circulation (Carleton et al., 1990; Maddox et al., 1995). Specifically, latitudinal shifts in the subtropical ridge, an extension of the Bermuda High, are associated with wetter Arizona summers during times of northerly displacement but drier summers during times of southerly displacement. Adams and Comrie (1997) noted that the 1990 monsoon season was an exception, as the center of the 500 mb High, typically located near the four-corners region during wet Arizona seasons, was instead shifted to the south.

In later chapters we will distinguish the influence of such longer-term variability in the varied impact of *Greater Phoenix* LULCC during drier as compared to wetter summers.

2.6 - Review: Effect of Phoenix' Development on Meteorology and Climate

The rapid growth and development of the *Greater Phoenix* area during the 20th century has led to an increased focus on the thermal impact of the metropolitan area's continuous expansion. A number of empirical studies examined surface temperature trends and attributed changes to the warming influence of urbanization. Cayan and Douglas (1984) found uniform warming at a number of SW urban sites, including Phoenix, based on data spanning the period 1933-1980. A comparison between 1969-80 means and 30-year climate means (1941-1970) revealed an increase in the diurnal, maximum, and minimum temperatures at Phoenix' Sky Harbor Airport. The increase in July minimum temperature of 2.4°C was greater than the 0.8°C increase noted for daily maximum temperatures. More recently, Brazel et al. (2000) showed that night-time urban minus rural minimum temperature differences, during May, have increased over time and attribute changes to population growth and urban/sub-urban development (they were not able to make a determination regarding the change in urban minus rural maximum temperature differences, however). Baker et al. (2003) has shown that the mean annual temperature at Phoenix' Sky Harbor International Airport has increased by 3ºC during the period 1948-1995. In addition to estimating trends representative during summer-time, Cayan and Douglas (1984) also observed positive temperature trends in January, though they were reduced in comparison, suggesting that the impact of urbanization on the thermal field, at least for *Greater Phoenix*, may be greater during summer rather than winter.

Investigations involving anthropogenic impacts on the local environment over the *Greater Phoenix* area also include the possible alteration of summer precipitation down-wind of the urban core (Diem and Brown, 2003; Shepherd, 2006; Diem, 2006), an influence on the stress levels of the Phoenix population resulting from excessive summer-time heat and its relation to changing land-use practices (Balling and Brazel, 1986), effects on air pollution and atmospheric ozone levels in the rapidly growing metropolitan area (Ellis et al., 2000), and the enhancement of the urban CO_2 dome over Phoenix (Idso et al., 1998).

There have been a limited number of numerical modeling studies aimed at improving our understanding of landscape controls on the diurnal cycle of the *Greater Phoenix* area. Zehnder (2002) used the Penn State/NCAR Mesocale Model Version 5 (MM5) and modified the urban landscape moisture availability, in conjunction with an improved specification of LULC, to better simulate the diurnal temperature cycle over Phoenix. They found that, while the distribution of latent and sensible heat fluxes across the urban canopy are important for accurate simulation of near-surface daytime temperatures, the contribution of these parameters does not significantly influence simulation of the nighttime low-level air temperatures. Grossman-Clarke et al. (2005), using a version of MM5 that incorporated an up-to-date LULC classification of the urban and surrounding rural area, accounted for the increased surface heat capacity of the developed urban core, assimilated anthropogenic heat production, and included longwave trapping through an estimate of the sky-view factor (SVF) to further improve the representation of the Phoenix diurnal temperature cycle. They found, in particular, that estimates of anthropogenic heating from traffic and electricity consumption, in conjunction with

adjustments to the outgoing longwave radiation through inclusion of the SVF, significantly improved simulated nighttime air temperatures.

The modeling work in this thesis aims to go beyond these studies to investigate the sensitivity of the atmospheric dynamics and thermodynamics over the *Greater Phoenix* area to the multi-decadal evolution of its landscape as a result of human activities.

Chapter 3 – *Greater Phoenix* Landscape Characterization and Classification

An initial task of this overall study is the evaluation of whether the *Greater Phoenix* area has indeed undergone an extensive landscape alteration beginning in the early 1970s, when satellite data first became available, and to quantify these changes. Accordingly, at the beginning of the project we purchased satellite data from the 1970s through the early 1990s to diagnose this landscape evolution (at the time, the raw circa-2001 data was not available). One commonly used standard image analysis technique, discussed in Chapter 3.1, was performed to identify whether and to what extent urbanization had occurred during this time interval. In Chapter 3.2, the mapping of available LULC reconstructions based on this satellite imagery onto the RAMS land-surface scheme to better match conditions appropriate for the *Greater Phoenix* region is presented. Chapter 3.3 uses these reconstructions to quantitatively describe the LULCC over the last three decades.

3.1 - Assessing Landscape Change from Satellite Imagery

At the beginning of the project we undertook an assessment of landscape change from the advent of the satellite era, in the early to middle 1970's to 1992. At the time, data availability precluded our ability to extend this analysis to more recent landscape representations. Nevertheless, the two-decade-long duration between these two periods was deemed sufficiently long to conclude whether landscape change was indeed occurring, to provide a backdrop and motivation for the model sensitivity experiments to be carried out. The results presented in this section illustrate one change detection technique commonly used in the remote sensing community to examine land cover change. In addition the following discussion reveals some of the issues involved during the initial steps of a LULC classification.

Satellite remote sensing data has become an effective tool for investigations focused on landscape change. The ability of satellites to observe the surface for extended periods of time make the resultant data a valuable tool in the analysis of both short and long-term change detection. There are two basic assumptions in LULCC detection: (1) any changes in surficial materials produce corresponding changes in satellite remote sensor radiance values, and (2) environmental characteristics (e.g., atmospheric conditions) and changes in satellite remote sensor system/characteristics (e.g. variability in spatial resolution or look angle) can be accounted for (Jensen, 1996).

North American Landscape Characterization (NALC) data, consisting of Landsat Multi-Spectral Scanner (MSS) time-series triplicates, were purchased from the Earth Observing System (EOS) Data Gateway (for more information see the web site at http://edcimswww.cr.usgs.gov/pub/imswelcome/). The triplicate set consisted of four separate images: two images from the 1970's and one each from the 1980's and 1990's. Data from the 1970's and the 1990's was used in an attempt to span the longest possible time interval.

The two 1970s images were for June 25, 1973 and July 31, 1975, each encompassing somewhat different geographical areas. To increase similarity, in terms of areal extent, we mosaicked the 1970s images into a single image (Figure 3.1 [a]). Figure 3.1 [a] shows that use of either of the single images alone would have allowed coverage of significantly less of the desired geographical area. The 1990s image was for July 26, 1992 (Figure 3.1 [b]). A comparison of both the mosaicked 1970s and 1992 images reveals that a northeast piece of data is absent from the 1970s imagery. This is the result of a slight shift in the satellite path that occurred between the dates of image acquisition.

We used ERDAS Imagine software for all the image analysis. Prior to performing change detection analysis, we normalized the mosaicked 1970s image to the 1992 image date to correct for differences in atmospheric influences and scene illumination. Ten normalization targets were identified as relatively time-invariant features. We used a simple linear regression method and calculated R-squared values to exhibit the strength of the relation that can be explained by the linear regression. Table 3.1 presents R-squared values obtained for each of the four MSS bands used in the analysis. Three of the four bands exhibited R-squared values at or above 0.90, while band 1 (green band of the electromagnetic spectrum) was slightly below. These values were deemed acceptable, and we determined that the normalized 1970s image accounted for the majority of environmental differences occurring between the two acquisition dates.

The type and extent of LULC over the *Greater Phoenix* area can be seen in Figure 3.1. Irrigated agricultural regions are represented by red pixels while the urban landscape is characterized by purple pixels. Figure 3.1 [a] also displays a small body of water (as denoted by black pixels near the center of the domain) that disappeared by the early 1990's (see Figure 3.1 [b]). Native vegetation is characterized by shrubland, seen as light aqua, while the dark patches illustrate the variable terrain and surround the metropolitan complex in all directions. Close examination of both images reveals the primary landscape change during this time interval: expansion of the urban area (purple pixels) at the expense of irrigated agriculture (red pixels).

We assessed changes over the *Greater Phoenix area* using a standard technique common among change detection analysts: image differencing (Jensen, 1996). Image differencing requires the subtraction of brightness pixel values from one band of imagery

from the same band of another image. The ensuing image results in positive and negative values depicting areas of radiance change and zero values for areas of no change. Initial 8-bit image pixel values, before band subtraction, range from 0 to 255, while difference values may range between -255 to +255 after band subtraction. Once image differencing occurs, it is assumed that the resulting differenced image exhibits a histogram with a bi-modal distribution. In the vicinity of the mode (i.e., values centered about zero) it is understood that little to no change of surficial materials has occurred. Most change between the two images occurs at the tails of the histogram. A complicating issue involved when applying this method deals with the determination of appropriate change thresholds (i.e., where to place threshold boundaries depicting change and no-change pixels in the histogram that determines the brightness values of the resultant image). There is no objective method to determine an absolute change threshold value, and most image analysts apply a trial and error approach so as to match reality. Abdullah (2000) used threshold values based on one standard deviation from the mean, for a semi-arid region (i.e., Las Vegas, NV), to determine threshold boundaries. We used a boundary located one standard deviation from the mean as well, given the geographical similarity between the two studies.

Figure 3.2 shows the red band differenced image (1992 MSS minus 1973 MSS). White areas are classified as no change between 1973 and 1992, as they are within one standard deviation of the mean. Red and green pixels are classified as one standard deviation below the mean and one standard deviation above the mean, respectively. Red pixels illustrate a decrease in red band reflectance from the 1970s to the early 1990s, while green pixels depict an increase in reflectance over time. Decreased reflectance

over time can be attributed to urban growth, while an increase in reflectance may be interpreted as cleared land.

Figure 3.2 indicates that significant urbanization and extensive clearing did occur during this time period. However, although this technique retrieves valuable change information, it is best applied when used in conjunction with other techniques. Unfortunately, all other techniques require some form of classification to one or both images, for which ground truth information is generally necessary, but was unavailable to us. The amount of change (in large part due to the threshold selected by the image analyst) is subjective and requires the user to be familiar with the area of interest. Specifically, image differencing does not provide any information on the nature of the change but only indicates areas that may have changed. For example, Figure 3.2 displays a significant amount of urbanization to the southeast, to the west and northwest of Phoenix (red pixels). Simultaneously, this area also observed significant clearing (green pixels in northeast quadrant of Figure 3.2), representing the decrease in agricultural acreage with time. However, extensive patches of green and red pixels are also evident in the western half of the geographical area as seen in Figure 3.2. This geographic area fell outside of the one standard deviation threshold and suggests an overestimate of landscape change (also noted from differences between Figure 3.1 [a] and Figure 3.1 [b]).

3.2 - LULC and Biophysical Parameters

Before being able to represent a landscape snapshot, as captured, for example, in the satellite images discussed above, in the land-surface scheme of a GCM or RCM, two important steps are required. First, the satellite imagery must be deconstructed into individual land-use or land-cover categories. Then, these categories must be given their

own characteristic biophysical parameters and mapped onto the model grid for use in the equations governing the surface energy, moisture, and momentum balances. Fortunately, step one, the derivation of independent landcover classifications for the 1970s, early 1990s, and the near-present, was not necessary. United States Geological Survey (USGS) Geographic Information and Analysis System (GIRAS) landscape data based on 1972 and 1973 aerial photography was obtained for central Arizona (Steyaert, personal communication). The data was based on a 1-km dominant land cover class that was previously extracted from 1:250,000 scale Land Use Data (LUDA) maps. USGS's digital reconstruction of the early 1970's landscape was based upon the retrieval of imagery from NASA's Landsat MSS, a sensor onboard Landsats 1 through 5 that acquired nearly continuous images of the Earth's surface beginning in July 1972. NASA's Landsat Thematic Mapper (TM), Enhanced Thematic Mapper (ETM), and ETM+ sensors followed, allowing for improved LULC reconstructions in subsequent decades. The Multi-Resolution Land Characteristics Consortium (MRLC) National Land Cover Dataset (NLCD) 1992 (Vogelmann et al., 2001), based on late 1980's/early 1990's Landsat TM imagery, was compiled for Arizona. The NLCD01 (Homer et al., 2004) was subsequently released based on late 1990's/early 2000's ETM+ imagery. Figure 3.3 presents an aerial view of the *Greater Phoenix* area as seen from recent Landsat 7 imagery. The image, taken on May 21, 2000, displays the agricultural envelopment (green pixels) of the urban landscape (turquoise pixels), all surrounded by natural shrubland (varying shades of brown). A comparison among Figure 3.1 [a], Figure 3.1 [b], and Figure 3.3 provides a complementary perspective on the evolution of landscape change in the area over nearly three decades. Agricultural fields nearly encapsulating the

relatively small urban area in the early 1970's has been diminished as the metropolitan complex has expanded in nearly all directions.

The acquisition of these three separate landscape datasets – early 1970's, early 1990's, and early 2000's – allowed us to proceed to step two, i.e., ingesting the reconstructed categories into RAMS, and the subsequent evaluation of the effect of landscape evolution on summertime climate over the *Greater Phoenix* area. Before incorporation into a numerical model, several key points regarding usage of this data were addressed. First, the original NLCD landscape reconstructions (i.e., NLCD92 and NLCD01) were constructed in an Albers Equal Area (i.e., a plane) projection with units of meters, while the original GIRAS data (hereinafter referred to as NLCD73 for consistency with the two more recent datasets) was projected onto a sphere. Therefore, the GIRAS data was re-registered using ERDAS-Imagine to conform to the pair of NLCD landscape reconstructions. Second, all three reconstructions used distinct LULC classes with the GIRAS data making use of Anderson Level II classes (Anderson, 1976). Consequently, NLCD73, NLCD92, and NLCD01 classes were all mapped onto a common set of LULC classes to be used in the land-surface component of our numerical model. Table 3.2 presents the common landscape classification set used for all three reconstructions.

Lastly, we carried out an additional landscape reconstruction to represent a hypothetical, pre-1900 dataset (hereinafter referred to as the Pre-Settlement case). This was achieved by modifying that part of the altered NLCD92 landscape attributed to anthropogenic influence (defined as irrigated agriculture and urbanized pixels) with semi-natural shrubland. We used NLCD92 reconstruction for this because, at the time (early in

the project), it was the single available dataset. A comparison between simulated regional climate for the hypothetical Pre-Settlement and actual NLCD92 LULC is presented in Chapter 6.

All three NLCD datasets were initially mapped with different methods and differing classes. Therefore, even after re-mapping onto a common set of LULC classes, a direct pixel by pixel class comparison of the existing classes and between the dated datasets was not recommended. However, we performed additional analyses of landscape trends, with time, to estimate the broad change of the landscape, as we discuss in more detail below (Chapter 3.3). We paid particular attention to trends associated with a general theme for which supporting evidence exists in the literature: the decline of agriculture at the expense of urban development and expansion (e.g. Knowles-Yanez et al., 1999).

As discussed in Chapter 2.1, when performing modeling studies, it is vital to account for the appropriate, regionally specific representation of important biophysical parameters that characterize the area's landscape. Accordingly, we used ancillary satellite data, including Normalized Difference Vegetation Index (NDVI) data from the Global Land-1km AVHRR Project (available freely online via the Earth Resources Observation and Science Data Center: http://edcsns17.cr.usgs.gov/1KM/comp10d.html) and the Moderate Resolution Imaging Spectroradiometer (MODIS) Land Product Subsets website (in conjunction with the North American Subsetting and Visualization Tool – http://www.modis.ornl.gov/modis/modis_subsets5.cfm) to help map the NLCD classes onto appropriate sets of physical and biophysical parameter values within the land-surface component of our model and to assist in establishing a final, ready-to-use, parameter table appropriate for the *Greater Phoenix* region (see Table 3.2). For example,

we followed the methodology of Zeng et al. (2000) and used the 90th percentile (based on the histogram of the seasonal NDVI maxima for each pixel) to calculate the appropriate vegetation fraction corresponding to the particular class of shrubland that predominates over the *Greater Phoenix* area. In addition, we carried out extensive analysis of the literature (e.g., Kuchler, 1964; Gibbens et al., 1996; Grimmond and Oke, 1999; Scurlock et al., 2001) to determine the most appropriate values of the other physical and biophysical parameters used by the land-surface component of the model.

3.3 - Quantitative Evaluation of Greater Phoenix' Landscape Evolution

The advent of the satellite era during the early to middle 1970s offered the possibility to quantify the effect of rapid population growth in terms of changing landscape patterns. The GIRAS LUDA product was the first effort aimed at digitizing landscape data and represents the initial such result based on actual satellite products and aerial photographs. The resulting NLCD73 landscape reconstruction prepared for this research, in conjunction with NLCD92, and NLCD01 reconstructions, allowed us to characterize landscape trends over time. The major landscape conversion themes are addressed below.

Figure 3.4 [a, b, c] presents the fractional landcover difference (NLCD01 fraction of total area minus NLCD73 fraction of total area) in (a) urban land area, (b) irrigated agricultural land area, and (c) shrubland area, while Figure 3.5 [a, b, c] presents the fractional landcover difference for NLCD92 minus NLCD73, also for (a) urban land area, (b) irrigated agricultural land area, and (c) shrubland area. We focus on these three landscape alterations, as they are the major LULCs undergoing conversion during this time.

Inspection of all images suggests a trend among the three landscape reconstructions. First, urbanization occurred to the northwest and southeast of central Phoenix as territorial expansion proceeded from NLCD73 to NLCD92. Urban sprawl continued unabated during the ensuing decade, as urban land expanded in nearly all directions. These results are consistent with findings discussed in Chapter 3.1 and highlight the importance of broad landscape comparison to complement pixel-by-pixel change assessments. The majority of the increase in urban land was at the expense of losses in plots of irrigated agriculture. However, gains in urban land also occurred at the expense of natural shrubland. This is especially evident in a region just east and north of the central business district of Phoenix (centered at about 33.6 N/112 W; see Figure 3.4 [c] for the difference between NLCD01 and NLCD73). To the north of *Greater Phoenix* (north of about 34° N latitude) large increases in natural shrubland occur over time, due to reduction in evergreen forest.

At this stage, we have characterized LULCC over the *Greater Phoenix* area and have LULC reconstruction datasets ready to be used in numerical model studies. Therefore, the subsequent chapters of this thesis will focus on the modeling: experiment design, evaluation of the simulations, and modeling results.

Chapter 4 - Model and Experiment Design

4.1 - RAMS Model

The Regional Atmospheric Modeling System (RAMS) version 4.3 (Walko and Tremback, 2000) was used for all experiments. RAMS is a non-hydrostatic model that solves the full nonlinear equations of motion, includes a comprehensive soil and vegetation component, the Land Ecosystem-Atmosphere Feedback Model (LEAF-2) (Walko et al., 2000), as well as multiple parameterization options for convection, turbulence, radiation and cloud microphysics.

LEAF-2 is prognostic in energy and water exchange between the land surface and overlying atmosphere. Notably, LEAF-2 allows for the division of each grid cell into multiple patches, and thus accounts for subgrid-scale landscape heterogeneity (assuming LULC data is indeed subgrid-scale relative to the model's resolution – this issue is further addressed in Chapter 4.2) with each patch interacting with the overlying atmosphere individually, based on the particular vegetation, soil textural class, and soil moisture representation.

The flexible horizontal and vertical resolution options available for RAMS allow for its use in a wide range of studies from the very small-scale (e.g., Avissar et al., 1998) to the climate scale (e.g., Liston and Pielke, 2000). In addition, two-way grid nesting gives RAMS users the option to embed high-resolution grids within larger, coarser grids. The nested grid approach and domain configuration are described in Chapter 4.2. Lastly, due to the regional nature of RAMS, large-scale meteorological analyses used to describe background flow are used to nudge the model. Several nudging choices are available to

the user, including at the lateral boundaries, at the top of the model, and within the simulation domain.

4.2 - Model Configuration

The simulation domain was centered over Phoenix' Sky Harbor International Airport located at 33.43°N and 112.02°W. Three multiple nested grids were used, permitting the downscaling of the large-scale synoptic flow from the coarse outer grid to the fine inner grid to better resolve the dynamic and thermodynamic details related to the imposed landscape change. The parent grid (grid 1) covers a significant portion of the NAMS region, including the majority of the Gulf of California and the eastern Pacific Ocean, and encloses a 1600-km x 1600-km domain using a 32-km grid spacing in the horizontal. The intermediate grid (grid 2) covers a 592-km x 592-km area using 8-km grid spacing, while the fine grid (grid 3) encloses a 204-km x 204-km domain using 2-km grid spacing. For each grid, 38 vertical levels were used, with a stretched vertical coordinate, ranging from $\Delta z = 50$m at the surface to $\Delta z = 1000$m at and above 5-km to the model top at 21.4-km. The lowest 1.5-km is resolved with the initial 15 vertical levels to capture the composition of the planetary boundary layer. A graphical representation of the model domain showing the topography and nested grid configuration is presented in Figure 4.1. The Kain-Fritsch convective parameterization scheme [Kain and Fritsch, 1992] is turned on for Grids 1 and 2, but it is off for Grid 3. We configured RAMS to use 11 soil layers, from the surface down to a depth of 2m.

The model landscape representation is examined next. NLCD73, NLCD92, and NLCD01 landscape data were used only on Grid 3. As LEAF-2 permits the division of each RAMS grid cell into multiple patches, each RAMS 2-km cell was further subdivided

into five patches of decreasing LULC fractional area (four plus water), thus retaining much of the information available in the higher resolution NLCD73, NLCD92 and NLCD01 data. Figure 4.2 [a, b, c, d] displays the dominant LULC classes for all four landscape reconstructions (Pre-Settlement, NLCD73, NLCD92, and NLCD01) used in the representation of the fine grid.

One important issue faced was how to appropriately represent the effects of extensive warm-season irrigation of the agricultural areas. To replicate these effects, we adopted the simple approach of forcing the soil moisture for each irrigated agricultural land cover grid cell (within grid 3 only) to saturation at each model time step. We discuss the sensitivity of the results to this assumption in more detail in Chapter 6.

For the outer two grids, in all experiments, the standard RAMS LULC dataset, based on the USGS 1-km Advanced Very High Resolution Radiometer (AVHRR) Olsen Global Ecosystem (OGE) land cover data (Olson, 1994) was used.

All experiments were initialized with surface (soil moisture and temperature) and lateral boundary (geopotential height, relative humidity, temperature, and horizontal winds) conditions extracted from the North American Regional Reanalysis (NARR) data (Mesinger et al., 2006) (available at http://www.emc.ncep.noaa.gov/mmb/rreanl/). All simulations were initialized on June 30, 00Z, forced at the lateral boundaries by NARR data, and continued through July 31, 12Z. The initial 30 hours were discarded prior to analysis and results were written out every three hours.

A total of 24 different simulations were produced for this study: four simulations each (corresponding to the four landscape scenarios) for Julys from six separate years. See Table 4.1 for a summary of all experiments performed. The choice of year for each

selected July was made according to their classification as either “wet” or “dry” summer seasons (see Chapter 4.3). The distinction between “wet” and “dry” monsoon seasons was made to better distinguish the effect of landscape-imposed forcing on the atmosphere. The hypothesis was that, during times of heavy and widespread rainfall, the regional contribution of the landscape will be difficult to distinguish given the large-scale forcing and atmospheric (as opposed to surface) control of precipitation, consistent with expectations based on previous work (e.g., Findell and Eltahir, 2003; Koster et al., 2004; Anyah et al., 2007). By keying on “wet” and “dry” NAMS conditions, the possibility of greater or lesser sensitivity to LULCC given contrasting hydro-meteorological regimes was more easily investigated.

The selection of the three wettest and three driest monsoon seasons (total of six seasons) during the time period for which NARR data were available (1979-present) was made according to the Daily UNIFIED Precipitation dataset (Higgins et al., 2000). The following section describes the methods involved in the selection process.

4.3 - Selection of Simulation Years

The selection of simulations was based on the determination of extreme NAMS precipitation years, as guided by an appropriate NAMS Index. We adopted such an approach to try to obtain a more robust signal from the subsequent simulation results among the different experiments. Moreover, this procedure allows for the interpretation of the impacts of small-scale forcing in the context of variable large-scale forcing, an important overall goal of this work. For example, is the temperature, or precipitation, response using NLCD73, NLCD92, and NLCD01 along with a "Hi- NAMS Index" large-scale forcing different when compared to a "Lo- NAMS Index" forcing?

We chose a number of case study years based on daily observed precipitation data encompassing the period 1948-1998. We used the Daily U.S. UNIFIED Precipitation dataset (Higgins et al., 2000), a 0.25 x 0.25 degree gridded dataset available from the Climate Prediction Center (CPC). Based on analysis of this data, appropriate years were incorporated into a low precipitation, or dry, NAMS sample and a high precipitation, or wet, NAMS sample. Diagnostic variables important to the NAMS circulation were selected and use of ECMWF ERA-40 Reanalysis data was made to demonstrate differences in the atmospheric pattern between the two samples (see below).

Different researchers have focused on variable geographic areas when discussing the climatology of the NAMS. Though the major (precipitation) signal observed over the SW U.S. is over Arizona, some have included locations as distant as California and Utah in their discussion of NAMS impacts (e.g., Adams and Comrie, 1997). As our primary geographical area of focus is the *Greater Phoenix* area we designate our analysis domain for calculation of the NAMS index to be centered over Arizona. The choice of box 10-degrees longitude x 8-degrees latitude is sufficiently large to capture a major component of the NW branch of the NAMS geographical area, including the primary focus area of this work.

Southwestern U.S. rainfall associated with the NAMS becomes apparent as rapid increases in precipitation, in late June/early July, following an extended period of relative dryness. Figure 4.3 [a] shows the long-term (1948-1998) mean yearly evolution of daily domain averaged precipitation (black contour) and seven day running mean (green contour) over the region of interest. The distribution of annual precipitation may be subdivided into two components: precipitation related to the NAMS and that resulting

from the equator-ward migration of the extra-tropical storm track during northern hemisphere winter. Succeeding the pole-ward migration of the jet stream is a period of low spring and early summer precipitation, followed by the abrupt onset of monsoon-related precipitation near the beginning of July.

The time-averaged (1948-1998) geographic distribution of annual precipitation is shown in Figure 4.3 [b]. Precipitation is highly dependant on the region's complex topography and is greatest along a northwest-southeast axis (values greater than 1 mm/day) along the length of the Mogollon Rim (extending from the Grand Canyon toward the White Mountains adjacent to New Mexico, the Mogollon Rim marks the southern edge of the Colorado plateau) and along the higher elevations near the U.S./Mexico border. Southwest of the Mogollon Rim, annual precipitation diminishes as mean elevation decreases. Indeed, along the California/Arizona border lies one of the driest regions in the United States: total precipitation values do not exceed 140 mm over a broad area, and in some locales are at or below 100 mm.

The seasonal, July-August-September (JAS), distribution of monthly precipitation shows a strong resemblance to the annual distribution (Figure 4.3 [c]). The monthly mean precipitation distribution shows two locations of relative maxima: along the Mogollon Rim and along the higher terrain alongside the U.S./Mexico border.

A chief characteristic of NAMS-related precipitation is its high degree of interannual variability. To diagnose the degree of variability of seasonal (JAS) domain-averaged precipitation, we calculated the departure from normal, using as the base mean the 1948-1998 domain average (Figure 4.4). Values above one correspond to wetter-than-normal

monsoon seasons, while values below one correspond to drier-than-normal monsoon seasons.

Several years were classified as extreme dry and wet NAMS precipitation years with the criteria that absolute quantities exceeded one standard deviation of the long-term precipitation mean. The one-standard deviation demarcation (sigma value of 0.22) corresponding to Figure 4.4 suggests several candidates above (below) the 1.22 (0.78) deviation value (corresponding to 22% above or below the long-term mean) of JAS-mean suitable as extreme precipitation years. Based on this criterion, seven individual member years were selected to make up the DRY sample and six members were chosen to make up the WET sample (see Table 4.2).

An apparent feature of Figure 4.44 is the high degree of variability visible on an interannual basis. Despite selecting individual monsoon years that were established as being sufficiently different, ascertaining whether the atmospheric behavior among these two samples was of a similarly different nature was deemed a necessary objective in the final selection process. Indeed, it is the effect of changing differential land-use patterns over time on local and regional climate in context of *variable* large-scale atmospheric forcing that is a chief purpose of this work. Therefore, we analyzed additional diagnostics related to the evolution of the NAMS to determine whether the atmospheric behavior leading to the resulting extreme precipitation was in reality, different.

The thermal contrast between the land and adjacent water body (i.e., the Gulf of California and the eastern subtropical Pacific Ocean) serves as the initial impetus for atmospheric moisture transport into the SW U.S. A considerable difference between wet and dry monsoon years is related to the date of onset. Monsoon years with earlier (later)

onset dates generally have higher than normal onset land surface/low-level temperature (lower than normal land surface/low-level temperature) and typically produce greater (lower) than normal total rainfall accumulations (Higgins et al, 1997; 1998). As the monsoon precipitation follows, the resulting rainfall prevents further land surface/low-level temperature warming, thus reducing the initial thermal gradient. Consequently, the early onset of monsoon rainfall, in concert with warmer than normal (initial) land surface/low-level temperatures, lead to a more rapid cooling of the land surface as compared to late onset monsoons. Therefore, we made use of the ECMWF ERA-40 Reanalysis data 2-meter temperature and 500-mb geopotential heights (relevance of this parameter was discussed in Chapter 2.5) to establish whether the selected anomalous NAMS precipitation years were related to a similarly dissimilar atmosphere.

Figure 4.5 [a] shows the seasonal average (JAS) of 2-meter temperature difference between DRY monsoon years and WET monsoon years. The red shading indicates the region where the difference in 2-meter temperature is statistically significant at the 90% level based on a two-tailed Student's t-test. Despite the coarse resolution of the Reanalysis data (2.0 x 2.5-degrees) statistically significant differences during the occurrence of the NAMS (it is important to distinguish this analysis from an examination of these variables at or before monsoon onset), are evident north of the Gulf of California, extending northward into extreme southern Nevada. It is this area that typically experiences the greatest land surface heating, leading to the amplified land/water thermal contrast responsible for the initiation and maintenance of NAMS-related precipitation. The dry monsoon years experience a statistically significantly warmer 2-meter temperature, as the early onset of the monsoon in the wet sample has led

to a reduction of 2-meter temperature during the NAMS compared to the dry sample. Figure 4.5 [b] shows the seasonal average of 500-mb geopotential height difference (dry monsoon sample minus wet monsoon sample). Again, red shading in Figure 4.5 [b] indicates areas where the difference in 500-mb geopotential is statistically significant. The increased land surface/low-level temperature apparent in the dry sample manifests itself as greater thicknesses, which in turn result in increased heights compared to the wet sample. Consequently, we are confident that the years we selected for our simulations do indeed represent dissimilar large-scale atmospheric forcing.

Chapter 5 - Model Evaluation

Before assessing the impact of hypothetical and actual landscape evolution, we present a comparison between the control simulation (see Table 4.1 for a summary of all experiments performed) and available observations. We begin with a comparison between RAMS-simulated 2-meter temperatures and observed temperatures from six stations in and around the *Greater Phoenix* area. Five of the stations were available courtesy of the Arizona Meteorological Network (AZMET) (http://ag.arizona.edu/azmet/) while the sixth station - Phoenix Sky Harbor airport – was available courtesy of the National Climatic Data Center (NCDC) and represents the only available first-order National Weather Service (NWS) station available within our Grid 3 domain. We note here that due to variability between actual station elevation and the surface elevation used in the RAMS model we retain only those stations where elevation differences are within 30 meters - of the seven available AZMET stations in operation during July 1990, we retained five.

Figure 5.1 [a] shows the comparison between AZMET observed, three-hourly air temperatures and RAMS simulated 2-meter air temperatures, while Table 5.1 shows a comparison between simulated and observed monthly averaged daily maximum and minimum air temperatures, for each station, for July 1990. We also present, in Table 5.2, a station-to-station comparison involving daily cooperative meteorological station (COOP) data (as before, we retain only those stations where elevation differences between model and station are within 30 meters). Overall, RAMS captured the roughly weeklong warm and cool periods, as well as the daily maxima and minima, with reasonable fidelity, though with a noted cool bias that is more pronounced in the

simulated minima (see Table 5.1), for the entire month, averaged across all 6 stations. We suggest two possible reasons for this disagreement. First, prior to 1994, the station at Sky Harbor airport was located at the airport's runway premises (Brazel et al., 2000), possibly contributing to an observed warm bias at that station due to a lower surface albedo (resulting in higher daytime temperatures) and enhanced night-time heat loss from an underlying paved surface (resulting in higher night-time temperatures). Probably due to nighttime heat loss from an extensive paved surface, we note that the modeled negative minimum temperature bias at Sky Harbor is roughly twice as large as that at other stations. Second, the lack of a sophisticated urban parameterization scheme within RAMS hindered our ability to account for some urban processes known to enhance the UHI effect, including daytime shadowing and heat trapping effects (that may increase daytime temperatures of stations within the *Greater Phoenix* limits), the impact of decreased nighttime urban longwave cooling as compared to rural localities, a characteristic largely attributed to the reduction in sky view factor (SVF) (e.g., Oke, 1987), and the impact of anthropogenic heat flux. Using an identical resolution over a similarly sized domain, Grossman-Clarke et al. (2005) conducted 72-hour simulations and noted that the effect of the SVF and anthropogenic heat flux parameters significantly improved their ability to model the nighttime temperature regime of the Phoenix urban area. As a result of the likely underestimate of urban warming, we suggest that the results presented in this thesis serve as a conservative estimate of the effect of LULCC on temperature in the *Greater Phoenix* area, a suggestion we raise again in later chapters.

Direct measurements of dew point are made only at Sky Harbor airport, while the AZMET stations measured relative humidity (RH) as their moisture metric (the COOP

stations do not have any sub-daily data). Using observed values of temperature and RH, dew point temperatures were calculated at each of the five AZMET stations according to the definition of saturation vapor pressure (1), RH (2), and an approximation of the Clausius-Clapeyron equation (3):

$$E_s = E_0 \exp[(\frac{L}{Rv}) * (\frac{1}{T0} - \frac{1}{T})] \quad (1)$$

$$RH = 100\% * \frac{E}{E_s} \quad (2)$$

$$E = E_0 * [(\frac{L}{Rv}) * (\frac{1}{T_0} - \frac{1}{T_D})], \quad (3)$$

where E_S is the saturation vapor pressure, E_0 is 0.611 kPa, L is the latent heat of vaporization, R_V is the gas constant for water vapor, T_0 is a reference temperature (273K), T is the observed temperature, E is the calculated vapor pressure, and T_D is the dew point. We note that calculation of dew point is sensitive to very low values of RH, as may be expected during dry breaks of the monsoon period.

As the AZMET site dew-points are derived and not directly measured, we compared the lowest atmospheric level (24.3m) simulated and observed dew-point separately for the AZMET stations (Figure 5.1 [b]) and Sky Harbor (Figure 5.1 [c]). It is evident that the control experiment does a reasonable job of capturing the day to day variability in low-level moisture throughout the month, including the gradual moistening during the first half of the month and the drying trend observed during the latter half of the month. We do note, however, that model simulated dew-point values fluctuating between 9 -

20°C from about July 27th onward are significantly higher than calculated values at the AZMET sites (Figure 5.1 [b]). We attribute this discrepancy to the sensitivity of our calculations to RH, which was frequently below 20% during this dry period and on several occasions closer to 10%. In contrast, directly measured dew point at Sky Harbor airport does indeed suggest that actual dew-point values were generally between 9-15 °C during this time (see Figure 5.1 [c]).

We next present a comparison between model simulated precipitation and available observations. First, we compare daily rainfall accumulation across the entirety of our fine grid against the 0.25° x 0.25° gridded Daily U.S. UNIFIED Precipitation dataset (Higgins et al., 2000) for July 1990 (Figure 5.2 [a]). The model is able to capture both the timing and magnitude of most precipitation events. More often than not, when precipitation occurred according to the UNIFIED dataset, RAMS was able to correctly reproduce this rainfall. However, a noted deficiency is evident over the last week to ten days as RAMS considerably underestimates the second largest rainfall event of the month. When comparing monthly accumulations, RAMS simulates a rainfall total of 64.5 mm as compared to 67 mm for the UNIFIED dataset.

Next, we show a station average of the three-hourly modeled and observed precipitation for the five AZMET locations and Sky Harbor for July 1990 (Figure 5.2 [b]). Again, more often than not, RAMS is able to simulate rainfall when it was observed. The model was able to capture the rainfall occurring over the initial two days of the month, the ensuing several-day-long dry episode, and the subsequent heavier rainfall toward the middle of the month. However, RAMS was not able to reproduce two of the more significant events observed to occur during the latter third of the month.

Among the AZMET stations and Sky Harbor airport, RAMS was able to simulate the monthly accumulated precipitation within 50% of each of the station's totals (not shown). At Phoenix Encanto, nearly 50% of the monthly rainfall total occurred during an isolated thunderstorm event that produced 45 mm, during the overnight of July 24th. This event produced more than seven times the amount of rainfall than at Phoenix Greenway (6.1 mm) and nearly five times more than was observed at Sky Harbor (9.9 mm), both roughly the same distance from Phoenix Encanto. RAMS was not able to reproduce this localized cell, underscoring the impact of solitary convective elements in this region and the difficulty in simulating such events at precise locations. The RAMS regional average precipitation total for July 1990, however, does compare favorably with the regional average of both the monthly station and gridded product data, thereby providing an increased level of confidence for the precipitation analysis based on RAMS simulations with each of the land cover reconstructions.

Chapter 6 - First-Order Effect of LULCC

6.1 - Effect on Simulated Temperature and Dew-point

Before examining the effect of actual landscape evolution during the last three decades on the *Greater Phoenix* area meteorology and climate, we addressed the subject of hypothetical landscape change. The rationale behind this approach was that, if the mere presence of *Greater Phoenix*, versus its absence, produced no change on the regional climate, less significant landscape shifts (such as the actual evolution during the last 30 years) might be expected to produce a correspondingly smaller effect. Accordingly, this Chapter discusses the impact of two sets of experiments: six simulations with the NLCD92 landscape representation versus six simulations with the Pre-Settlement landscape representation.

RAMS simulated ensemble differences (i.e., NLCD92 minus Pre-settlement) in first atmospheric level air temperature and dew-point, for the WET and DRY years, are presented in Figure 6.1 [a, b, c, d]. A dipole pattern of differences is visible for both temperature and dew-point. For the WET years, the largest positive differences [> 0.5 °C] in temperature occur over the central urban area, with lower magnitude cooling [-0.1 to -0.2 °C] located south of the metro area, primarily over the plots of irrigated agriculture. This pattern is reversed for dew-point, which shows a decrease over urban areas of greater than 0.6 °C and increases, primarily over plots of irrigated agriculture, of at least 0.2 °C. These findings are in qualitative agreement with the magnitude of the Phoenix UHI ascertained from previous transect measurements over this area (Hedquist and Brazel, 2006). The same patterns, but with more pronounced maxima and minima, are evident for the DRY year simulations for both temperature and dew-point (compare

Figure 6.1 [c, d] to Figure 6.1 [a, b]). Maximum warming for the DRY years exceeds 0.7 °C over urban areas while irrigation-induced cooling is enhanced and covers a greater fractional area of the domain. Due to the increased surface-to-air water vapor concentration gradient experienced during dry atmospheric regimes, enhanced urban drying and increased moistening over irrigated agriculture occurs.

This leads us to the following result: in a regional-mean sense (i.e., as in an average over the entire grid 3 domain), the competing impacts of irrigated agriculture and urbanization largely tend to counteract each other for both the WET and DRY sets of runs.

One concern is that the cooling resulting from irrigated agriculture, due to our assumption of soil saturation, may be overestimated. To test the sensitivity of this assumption, we performed a repeat of the NLCD92 experiment whereby we forced the irrigated agricultural land cover type to field capacity, instead of saturation, at each model time step. With this change, cooling from the agricultural zones decreased considerably, drying expanded accordingly over the domain, and the effects of urbanization tended to dominate the domain-average signal. However, the assumption of saturated soil in the irrigated agriculture grid cells may be more realistic, as it produced better simulation results compared to observations of temperature and dew-point. This may be because it effectively accounts for additional water sources not explicitly modeled, such as mesic landscaping and surface water reservoirs.

The landscape induced effects on near-surface temperature arise due to a variety of pathways, some resulting from changes in the local vegetation, others taking place due to atmospheric transport. We address some of these processes below.

Our experiments accounted for two main changes in land cover. The replacement of the urban landscape with semi-natural vegetation results in an increase in albedo, effectively reducing the surface absorbed energy for the Pre-Settlement experiments. Figure 6.2 [a, b] indicates a sharp decrease (for NLCD92 in comparison to Pre-Settlement) in albedo across the urban landscape as well as over the plots of irrigated agriculture. Minor differences in albedo between the WET and DRY years are due to variations in surface moisture, which is used to calculate albedo in LEAF-2. Incident radiation is correspondingly altered (see Figure 6.2 [c, d]) (where albedo decreases the incident radiation increases), though the signal is much more evident during the DRY rather than the WET years.

In addition to the signal resulting from the LULCC, incident radiation is also influenced by changes in cloud cover. The mixture of precipitating systems of various scales, and their associated cloudiness, is exhibited as more of a mixed signal for the WET years. Nonetheless, both sets of experiments indicate an increase in incident radiation for NLCD92 as compared to Pre-Settlement.

While the changes in albedo across the urban and agricultural areas reinforce their respective effects on simulated temperature (i.e., they both act to increase low-level temperature), we have seen previously (see Figure 6.1 [a, c]) that warming occurs over the urban landscape, while (lesser magnitude) cooling occurs over the adjacent agricultural areas. This is due to differences in the sensible heat flux resulting from changes in both incident radiation and vegetation. Specifically, the conversion of shrubland to irrigated agriculture in the NLCD92 landscape has decreased the Bowen ratio, acting to partition less energy into sensible heating (Figure 6.2 [e, f]) and more into

latent heating. The decrease in sensible heat flux outweighs the impact of increased incident radiation (i.e., counters the effect of decreased albedo) over the plots of irrigated agriculture, resulting in cooling over these areas.

6.2 - Effect on Simulated Precipitation

To assess whether the modern-day *Greater Phoenix* landscape exerts a discernible influence on modeled precipitation, we next present simulated differences (i.e., NLCD92 minus Pre-settlement) in accumulated monthly precipitation for both the WET (Figure 6.3 [a]) and DRY (Figure 6.3 [b]) simulation years.

Mean differences for the WET years show a patchwork of increases and decreases in precipitation and do not indicate a systematic alteration in rainfall pattern or magnitude related to the imposed change in landscape. Additionally, there is no uniformity of trend or pattern across individual simulation years (not shown). This may be because the sensitivity of convective precipitation to near-surface thermodynamic perturbations is generally reduced in moist regimes with strong atmospheric control of precipitation (e.g., Findell and Eltahir, 2003; Koster, 2004; Anyah et al., 2007).

This basic understanding of how and under what circumstances the land-surface influences convection is consistent with the fact that differences between the pair of ensembles for the DRY years present a much more coherent and consistent signal than for the WET years, both in ensemble mean (Figure 6.3 [b]) and across individual years [Figure 6.4]. The differences for the individual year simulations each illustrate an increase in total domain precipitation for the NLCD92 landscape, with regions of most pronounced rainfall enhancement (at least 20-40 mm) situated generally east and north of the urban area.

These results are also broadly consistent with recent observational analysis suggesting a *Greater Phoenix*-imposed enhancement of precipitation (Diem and Brown, 2003; Diem, 2006; Shepherd, 2006). Shepherd (2006) used a 108-year precipitation data record and noted that positive precipitation anomalies during monsoon season (July-September [JAS]) exist to the northeast of the Phoenix metro area in a "post-urban" period (defined as 1950-2003) as compared to a "pre-urban" period (1895-1949). Their analysis indicates that precipitation was enhanced from the pre- to the post-urban era in the Lower Verde basin, in particular. Significantly impacted monsoon stations located further to the south, east, west, and within urban Phoenix did not demonstrate this characteristic precipitation increase. A trio of stations, all located within the southern half of the Lower Verde basin, experienced the maximum increase in mean precipitation (post-urban period minus pre-urban period) - greater than 10% - Sunflower, Horseshoe Dam, Bartlett Dam. Three additional stations in addition to the Lower Verde stations – Carefree, Cave Creek, and Roosevelt Dam - exhibited modest increases in mean precipitation over the same time period (between 5% and 10%). Figure 6.3 [b] shows the consistency between the spatial pattern of model simulated precipitation enhancement and precipitation enhancement as depicted in the observations according to the analysis of Shepherd (2006), to the north and east of *Greater Phoenix*. The locations of the aforementioned six stations (CF – Carefree; CC – Cave Creek; H - Horseshoe Dam; B – Bartlett Dam; S – Sunflower; R - Roosevelt Dam), which comprised of all stations exhibiting greater than a 5% increase in rainfall during the post-urban period (all other analyzed stations showed little to no change or displayed a small decrease in precipitation), are included in Figure 6.3 [b]. The geographic agreement between modeled and observed precipitation

enhancement provide an additional level of confidence that our simulation results are able to capture the correct long-term precipitation trend based on available observations.

Despite this qualitative agreement between their study and our results, we advise caution on a quantitative comparison of precipitation differences. First, Shepherd (2006) compared monsoon season averages of two periods, each consisting of in excess of 50 years, while our analysis is based on two relatively short-term, single-month periods each consisting of 3 years (as the WET year results show no discernible signal). Second, our work isolates the impact of LULCC alone, whereas the Shepherd (2006) results include an assortment of effects due to both a shifting landscape and a shifting climate during and between each time segment.

To gain insight into the mechanism responsible for the simulated rainfall enhancement during DRY years, we focused our attention on the main area of observed increase to the north and east of the city. Here we show (Figure 6.5 [a]) vertical profiles of θ_e difference averaged over a 1º X 1.2º region (see the rectangular sub-domain in Figure 6.3 [b]) for three selected pre-storm cases. We selected one case, for each year, which best illustrates the degree of impact on total static energy for the area of interest. For each case subsequent rainfall accumulation for NLCD92 was significantly enhanced relative to Pre-Settlement. The trio of profiles exhibit considerable increase in conditional instability in or just above the PBL. The net difference in θ_e for all cases is large, on the order of 5 K. Over timescales longer than that of an individual storm event, assuming that the background synoptic-scale is not competing with the local/regional scale, the accumulated landscape signal may modify regional stability sufficiently to allow for repeated enhancement of storm cells. Figure 6.5 [b] shows that the net impact

of LULCC is systematic and not specific to preferentially selected events, and that the chief influence is an increase in moist static energy in the upper reaches of the PBL and/or lower free atmosphere. The monthly averaged net difference in θ_e for all 3 simulated Julys, at 17 LST (time of day when landscape effect is at its maximum) is on the order of 1 K.

Our hypothesis is that, over timescales longer than that of an individual storm event, the enhanced warming, due to the presence of the urban areas, and the enhanced moistening, due to the presence of irrigation, combine to increase the moist static energy of the PBL. Assuming that the background synoptic-scale is not competing with the local/regional scale, the accumulated landscape signal may modify regional stability sufficiently to allow for repeated enhancement of storm cells.

In the following two chapters, we examine in detail how these effects of moistening and heating on the vertical thermodynamic structure of the atmosphere play out over the course of the evolution of the *Greater Phoenix* landscape from the 1970s to the current decade.

One additional and important impact of the hypothetical LULCC is on the mesoscale atmospheric dynamics. The enhanced surface heterogeneity due to the contrast between natural shrublands, irrigated agriculture, and urban areas creates characteristic diurnal, mesoscale circulations (as described in Chapter 2.2) in the NLCD92 simulations that are not present in the Pre-settlement simulations. The role of these circulations in the vertical transport of heat and moisture, and their interaction with the turbulent surface fluxes and the large-scale NAMS environment over the diurnal to monthly timescales, is also presented in Chapter 8.

Chapter 7 - Impact of Historical Landscape Change: Surface Analysis

The previous chapter identified the effect of hypothetical LULCC on the region's climate. The presence of irrigated agriculture has a local cooling effect, while the urban area has a local warming effect. These effects tend to cancel each other, to an extent, so that the net impact averaged over the whole domain of both landscape conversion themes is smaller than either one individually. For precipitation, instead of competing, these heating and moistening effects reinforce each other, destabilizing the lower atmosphere and, during DRY years when the surface is able to exert some control on convection, lead to a systematic precipitation enhancement for the NLCD92 as compared to Pre-Settlement landscape.

In this chapter, and in Chapter 8, we present the results of RAMS simulations carried out with the NLCD73, NLCD92, and NLCD01 landscapes and discuss the land-atmosphere interactions and associated atmospheric dynamical processes, in more detail, in the context of the actual landscape evolution that occurred in the *Greater Phoenix* region over the last three decades.

7.1 - Effect on Simulated Temperature and Dew-point

Figure 7.1 [a, b, c, d] shows the RAMS simulated ensemble differences (NLCD01 minus NLCD73) for both air temperature [a, c] and dew-point [b, d], for all three WET and DRY years. For both the WET and DRY years, maximum warming, of the order of 1K, occurs over the areas of greatest urbanization. As was observed during our analysis of hypothetical landscape change, peak warming is enhanced during the DRY years. In contrast to the analysis presented in Chapter 6, however, the extent of cooling has diminished in size considerably for NLCD01, a trend reflective of the reduction in

irrigated agriculture during this period. The WET simulations reveal a combination of warming and cooling to the north of the *Greater Phoenix* area, while the DRY simulations show a widespread area of enhanced cooling over this same region. Both sets of experiments illustrate a regional warming of 0.12K during the roughly three decade period of landscape change, in qualitative agreement with recent estimates of urban heat island tendency over the Phoenix area (Stone, Jr., 2008).

The decrease in dew-point temperature (Figure 7.1 [b, d]) resulting from the rapid decline in irrigated agriculture is centered over areas that have experienced the greatest urbanization. Although both sets of simulations indicate a drying tendency, the DRY experiments illustrate a regional enhancement of roughly twice the magnitude seen in the WET experiments. Balling and Brazel (1986) analyzed 88 years (1896-1984) of dew-point and RH over the Greater Phoenix area, finding that RH values fell at a statistically significant rate over this time period, a decrease they attribute largely to increases in temperature. Despite contentions that dew-point was on the rise, the authors found no long-term trend to validate the assertion, but did find evidence of a recent downward trend which they attribute to decreased coverage of agricultural lands. Though changes in dew-point are nearly non-existent to the north of *Greater Phoenix* for the WET simulations, there is a pronounced moistening (in excess of 0.2K) for the DRY years, coinciding with the area of cooling noted previously.

Landscape modifications have also impacted the daily simulated monthly-average of maximum and minimum low-level air temperature (Figure 7.2 [a, b, c, d]). Daily maximum temperature (Figure 7.2 [a, c]) changes show similar patterns for both the WET and the DRY years, although as already noted with the mean daily temperature,

maximum temperature differences for the DRY simulations are enhanced relative to the WET year experiments. In contrast to simulated maximum low-level air temperatures, the greatest effect on minimum temperature changes (Figure 7.2 [b, d]) does not occur directly over those areas where the landscape was altered, but is shifted to the north of the *Greater Phoenix* area. In addition, the peak increase in minimum (i.e., night-time) temperatures is less than half the magnitude of the peak increase in maximum (i.e., daytime) temperatures. The regional night-time warming, however, is slightly greater than the daytime warming (0.02K), for both the WET and DRY year experiments, indicative of a decrease in the regional diurnal temperature range (DTR) over the entire domain.

Notwithstanding the regional decrease in the DTR, a result consistent with the phenomenon of urbanization (e.g., Kalnay and Cai, 2003), the precise locales where urbanization occurred actually produced an increase in the DTR, as maximum temperatures increased more than minimum temperatures. Daytime heating of the surface in this region coincides with weak wind flow, and the additional absorption of radiation by the landscape drive the local temperature response. As evening and night-time draw near, wind flow, in a climatological sense, increases. Therefore, advection plays an important role in translating and rearranging low-level air over our domain.

While this helps explain why maximum night-time warming does not coincide with the precise areas of greatest urbanization in our simulations, there is still the question of whether the simulated magnitude of warming and impact on the DTR over the city is realistic. The thermal field of the urban environment is in large part determined by the choice of building and road construction materials. In addition to anthropogenic heat

release, a characteristic not taken into account by RAMS, thermal properties such as thermal diffusivity, heat capacity, and surface emissivity of the three-dimensional urban framework may affect both the day- and night-time urban environment. Hamdi and Schayes (2007) made use of an urban surface exchange parameterization to better understand the impact of a number of urban characteristics on the UHI intensity. Implementing their urban scheme in a mesoscale model and conducting simulations in one-dimensional mode, they found that increasing the thermal diffusivity and heat capacity by an order of magnitude augments the night-time UHI by up to 1K. The effect during the daytime, however, is reversed, and UHI intensity is diminished. The impact of emissivity is minor in comparison, showing negligible effect during night-time. In addition, geometric effects of the city environment also play an important role, for example, through surface shading from and trapping of insolation during daytime. The geometric configuration, commonly referred to as the aspect ratio effect, also influences night-time emission of longwave radiation to space. The impact on longwave loss is directly related to the sky view factor, as discussed earlier (e.g., Oke, 1987). The lack of such a comprehensive urban canopy parameterization in RAMS, able to account for the presence of and interaction between building walls, roof-tops, road surfaces, and the overlying atmosphere, likely results in an underestimate of the nocturnal UHI intensity. Therefore, the effects of urbanization we simulate (on temperatures and atmospheric processes) likely represent underestimates as well.

7.2 - Effect on Simulated Albedo and Surface Energy Balance

To better understand the pathways by which landscape evolution has altered the near-surface temperature, we analyze the regional surface radiation budget. Recall the

summary of the chief components involved in the determination of the surface radiation balance presented in Chapter 2.1.

RAMS simulated ensemble differences in net surface broadband albedo are presented in Figure 7.3 for both the WET [a] and DRY years [b]. The regional difference in albedo pattern (NLCD01 minus NLCD73), for both hydro-meteorological regimes, is nearly identical, though peak values are enhanced for the DRY years. The greatest decreases in surface albedo are apparent over the center of the domain. This region underwent significant urbanization during the three-decade period we are considering. Landscape conversion occurred at the expense of natural shrubland, whose albedo values are greater than that of urban areas, resulting in a strong positive radiative forcing on the shortwave component of the surface radiative budget (Figure 7.4[a, b]). Over this region, the DRY years show peak shortwave absorption differences in excess of twice the magnitude of the WET years. Differences in incident radiation (NLCD01 minus NLCD73) for the DRY years are generally consistent with changes in land cover. Though the primary effect on the radiation budget is through changes in albedo, incident radiation is also influenced, to an extent, by changes in cloud cover, particularly during the WET years.

Surrounding this centralized region, and marking the extent of the *Greater Phoenix* metro limits, are smaller pockets of relatively minor increases and decreases in broadband albedo (±0.02). Though the landscape was significantly modified in these areas as well, urbanization occurred at the expense of irrigated agriculture (in contrast to the aforementioned changes at the expense of shrubland), a land-use class possessing similarly low values of albedo. Therefore, our results suggest that the net effect on the observed change in the shortwave component of the surface radiative budget over the

Greater Phoenix metropolitan area is, in large part, due to the conversion from natural shrubland to urban landscape.

To the north of the *Greater Phoenix* area, a considerable increase in simulated broadband albedo is noted for the DRY year experiments (see Figure 7.3 [b]). Flanked by these large pockets of albedo increase are relatively smaller patches of albedo reduction. This broad northern region saw significant increases in natural shrubland at the expense of evergreen needle-leaf forest from the 1970s to the present decade. While the WET years illustrate a patchwork of increases and decreases in incident shortwave radiation over this northern area, due to greater changes in cloud cover, the increased shrubland albedo results in a coherent decrease in incident shortwave radiation for the DRY years. Consequently, we attribute the decrease in low-level temperatures over the northern one-third of our grid 3 domain to changes resulting from decreased surface absorption of shortwave radiation due to the conversion from evergreen needle-leaf forest to shrubland.

RAMS-simulated ensemble differences in net longwave flux are presented in Figure 7.5 for both the WET [a] and DRY years [b]. The regional pattern for both hydro-meteorological regimes is particularly similar although, as before, the DRY year experiments show an enhancement of this radiation budget component. Peak longwave radiation loss occurs over those areas that witnessed the greatest urbanization. In particular, the conversion from irrigated agriculture to an urban landscape facilitated the removal of a significant amount of (low-level) atmospheric water vapor that otherwise, through increased downward longwave emission, maintained greater levels of surface longwave absorption.

The mean monthly differences in net (shortwave plus longwave) radiative flux are presented in Figure 7.6 for both the WET [a] and DRY years [b]. Both plots indicate increases and decreases over the *Greater Phoenix* area, illustrating the twin contributions of urbanization resulting from shrubland (causing an increase in net surface radiation) and urbanization resulting from extensive loss of irrigated agriculture (causing a decrease in net surface radiation). To the north of the *Greater Phoenix* area, the effect of higher shrubland albedo and its impact on net shortwave radiation results in an overall decrease in net surface radiation.

7.3 - Effect on Simulated Regional Surface Fluxes

RAMS simulated ensemble differences (NLCD01 – NLCD73) in surface sensible heat flux are presented in Figure 7.7 for the WET [a] and DRY [b] year experiments. The chief difference between the WET and DRY year experiments is the enhancement in the peak flux values. As a result of compensating increases and decreases in flux magnitude, regional averages are similar for both sets of experiments, though both indicate a small increase in sensible heating of the order of 1 W m^{-2}. Areas where mean monthly flux differences are greatest (60-100 W m^{-2}) coincide with those areas where maximum warming occurred for NLCD01 as compared to NLCD73.

Differences in latent heating (Figure 7.8 [a, b]) show a similar, but reversed pattern, with latent heat flux reduction (60-100 W m^{-2}) occurring primarily over regions where irrigated agriculture was converted to an urban landscape. Latent heat flux values also decreased over those areas where shrubland was converted to urban land, although the reduction in magnitude was generally less than half of that seen in the irrigated agriculture to urbanization conversion.

The change in net (sensible plus latent) surface heat flux is presented in Figure 7.9 for both the WET [a] and DRY [b] year experiments. Alternating pockets of higher and lower fluxes in net surface heat flux are evident over the *Greater Phoenix* area. Due to the increase in surface sensible heating, areas that underwent a conversion from natural shrubland to urban land saw an increase in surface heat flux. In contrast, regions to the northwest and southeast of Phoenix (recall that these areas underwent significant urbanization at the expense of irrigated agriculture) saw a considerable reduction in net surface heat flux, with peak decreases for the DRY year experiments in excess of 20 W m^{-2}.

7.4 - Effect on Simulated Diurnal Cycle

To better understand the impact of landscape evolution on the diurnal cycle, we now explore the individual effects of four distinct modes of landscape transformation that occurred over the *Greater Phoenix* area during this time period. In particular, we investigate the near-surface atmospheric effect resulting from two different types of urbanization: (1) conversion of shrubland to urban land and (2) conversion of irrigated agriculture to urban land, along with two different types of increase in natural shrubland conversion: (1) conversion of irrigated agriculture to natural shrubland and (2) conversion of evergreen forest to shrubland.

Here, we only show averages over those grid cells that exhibited a shift in dominant land cover. For example, Figure 7.10 [a, b] presents the RAMS-simulated time series of diurnally-averaged first atmospheric level temperature differences (NLCD01 minus NLCD73) for the WET years [a] and the DRY years [b], for those grid cells that had at least 50% natural shrubland fractional coverage in NLCD73 and more than 50% urban

fractional coverage for NLCD01, with similar curves for irrigated agriculture to shrubland, evergreen forest to shrubland, and agriculture to urban land conversions.

The net effect on near-surface temperature for all pixels depicts an overall warming that peaks in the late afternoon/early evening (dashed, black line for both plots). The greatest contributions to warming result from the shift in irrigated agriculture to urban land and from the conversion of shrubland to urban land. The previously noted albedo reduction due to forest-to-shrubland conversion results in a temperature reduction that coincides with the time of simulated maximum solar heating.

The simulated effect on dew-point temperature differences (NLCD01 minus NLCD73) for the same land cover themes is presented in Figure 7.11 for both the WET years [a] and DRY years [b]. For all pixels, drying is roughly twice the magnitude during the DRY years as compared to the WET years. The greatest contribution to drying results from the shift in irrigated agriculture to urban land and from the conversion of shrubland to urban land. The significance of the diurnal cycle is manifested as a rapid increase in the rate of drying near the time of simulated sun-rise (15Z, or 8 LST). The importance of surface absorbed solar radiation and its effect on evapotranspiration becomes most apparent for the irrigated agriculture-to-urban land conversion, as a dew-point temperature decrease of the order of 1K (1.5K) is noted from sunrise to mid-afternoon for the WET years (DRY years). The lone theme that contributes to low-level moistening, as opposed to drying, occurs due to the conversion of evergreen forest to shrubland. As noted previously the difference in albedo between the two surfaces lowers surface absorbed radiation for shrubland (see Figure 7.12 [a]), serving to decrease low-level temperatures. Consequently, the amount of energy required to sustain shrubland

evaporation (at the same level as over needle-leaf forest) is reduced. Due to the albedo effect already noted, peak moistening (which is enhanced for the DRY years) coincides with the time when the sun is at its highest point in the sky, and the corresponding effect on evapotranspiration is potentially greatest.

The diurnally averaged net surface shortwave radiative flux for all four land cover conversion themes is presented in Figure 7.12 [a, b], for the WET [a] and DRY [b] years. Differences in incident shortwave radiation, which occur only during daytime hours, are either positive or negative, depending on the particular land surface conversion of interest. Both modes of urbanization (conversion from either irrigated agriculture or shrubland to urban land) have a positive impact on this budget component, though the shrub-to-urban conversion results in a radiative forcing more than twice the magnitude of the agriculture-to-urban conversion. As expected and discussed previously, conversion of evergreen forest to natural shrubland occurring in the northern tier of the domain results in a negative effect on the diurnally averaged surface absorbed shortwave radiation. However, the loss of irrigated agriculture to shrubland also results in a decrease of absorbed shortwave radiation at the surface. For these reasons, the effect on diurnally-averaged surface shortwave radiative flux follows the change in albedo for the particular land-surface conversions involved. During DRY years, although the effect is more pronounced for all conversion themes, the magnitude of increase is larger for landscape conversions that increase fractional coverage of shrubland, resulting in an overall decrease in incident shortwave radiation across the domain (see also Figure 7.4 [b]).

The diurnally averaged net surface longwave radiative flux curves are presented in Figure 7.13 [a, b], for the WET [a] and DRY [b] years. The effect of low-level water vapor loss due to the decreasing fractional coverage of irrigated agriculture is evident, as the two conversion themes contributing most to the surface longwave loss are the irrigated agriculture-to-shrubland and irrigated agriculture-to-urban land shifts.

As seen in Figure 7.14 [a, b], total radiative forcing resulting from the net contributions of shortwave and longwave absorption display a slight decrease for the WET years [a] and a more pronounced decline during the DRY [b] years. The lone landscape theme contributing in a positive manner to the total radiative forcing is the shrub-to-urban conversion with maximum increases of nearly 60 W m^{-2} evident during the early afternoon.

Finally, the shifts in land-use alter the diurnal cycle of the partitioning between sensible and latent heating. Figure 7.15 [a, b] shows that the overall change in sensible heat flux is generally consistent with the warming and cooling noted previously. All surface conversion themes contribute to an increase in sensible heating, except for the evergreen-forest-to-shrub conversion. The removal of vegetation (i.e. irrigated agriculture) at the expense of increased coverage of urban land, shifts surface energy partitioning to increased sensible and decreased latent heat (see also 7.16 [a, b]), a result that is in agreement with previous numerical modeling studies. The agriculture-to-urban land conversion shows the greatest effect on the surface flux energy partitioning with increases (decreases) in turbulent sensible (latent) heating of about 100 Wm^{-2} between the WET and DRY years. The forest-to-shrub conversion is the lone conversion theme that

increases turbulent latent heating, though it only partially offsets the negative contributions from the remaining three themes.

Chapter 8 - Impact of Historical Landscape Change: Atmospheric Analysis

The partitioning of surface absorbed energy into sensible and latent heating has been shown to be a significant driver of atmospheric circulations and convective activity in many regions of the world and on a variety of scales (Pielke, 2001). Here we address the role of the previously discussed surface budget changes, the effect on convective rainfall and its association with the large-scale NAMS storm systems, the mesoscale dynamics of the region, and their interaction.

8.1 - Effect on Simulated Precipitation

Figure 8.1 [a, b] illustrates the RAMS simulated ensemble differences in total accumulated precipitation for all three WET and DRY years, respectively. Similar to the results presented in Chapter 6, the difference pattern for the WET years does not indicate a systematic landscape-induced impact on rainfall. The pattern for the DRY years, however, appears very similar to the ensemble differences noted between the NLCD92 and Pre-Settlement cases. To assess the possible impact of landscape evolution with time, we compare ensemble rainfall differences for our successive landscape reconstructions. We focus on each of the trio of DRY years, because, as discussed throughout, it is during this hydro-meteorological regime that convective triggering is most sensitive to land-surface changes.

Ensemble differences in total accumulated precipitation for 1979 are presented in Figure 8.2 [a] for the difference between NLCD92 and NLCD73, and in Figure 8.2 [b] for the difference between NLCD01 and NLCD73. Precipitation enhancement for NLCD92 relative to NLCD73 is apparent to the north and east of the *Greater Phoenix* area. The magnitude of increase is generally in excess of 20 mm, with local differences

reaching as high as 60-80 mm. This same pattern of precipitation enhancement is apparent for the NLCD01-minus-NLCD73 difference, but with the positive difference values expanded in territorial coverage and increased in magnitude. This systematic strengthening of the precipitation signal from the NLCD92 to the NLCD01 landscapes suggests a consistent response of the atmosphere to the land-surface forcing.

We next present ensemble differences in total accumulated precipitation for 1989 (Figure 8.3) and 1994 (Figure 8.4). For 1984, although precipitation differences are negative between NLCD92 and NLCD73, NLCD01 does indicate an enhancement (relative to NLCD73), of generally 20 mm, to the north and east of *Greater Phoenix*. For 1994, any coherent landscape-induced effect on precipitation seems much weaker. In several ways (e.g., precipitation amounts, large-scale NAMS dynamical environment), 1989 and 1994 are significantly more "WET" as compared to the dominant "DRY" year of 1979 - this will also be apparent below, when we discuss the signal of the landscape changes and the effect on the mesoscale atmospheric dynamics.

We next examine these mesoscale dynamics to perhaps gain some insight into the dynamical impact of the evolving landscape and factors that may be responsible for producing these differences in convective rainfall.

8.2 - Mesoscale Dynamics: Flow

Modifications of the underlying land surface, via effects on the surface radiation budget, are responsible for the creation of thermal gradients across the landscape and in the lower atmosphere. As discussed in Chapter 2.2, the reorganization of lower-tropospheric pressure gradients according to the pattern of landscape heterogeneity may

influence low-level wind flow: i.e., create diurnal mesoscale atmospheric circulations. Here we explore how the mesoscale dynamics are influenced by the landscape changes.

To highlight the impact of land surface heterogeneity the focus will be on the DRY years. We look primarily at early afternoon conditions when the thermal gradient is at its peak and landscape-induced circulations are expected to form.

Figure 8.5 [a] presents the monthly averaged wind speed difference (NLCD01 – NLCD73) for 1979, at 14 LST, for the lowest model atmospheric level. Overlaid are the monthly averaged wind vector differences (NLCD01 – NLCD73) for 1979, also calculated at 14 LST. Close inspection reveals well-defined areas of both convergent and divergent air flow. In the southwestern quadrant of the domain, the predominantly southwest flow of air displays directional (wind vectors are directed toward one another) convergence related to the presence of a small lake in NLCD73 that had dissipated in the NLCD01 reconstruction (compare Figure 3.1 [a] and [b] for verification of lake dissipation). However, changes in wind speed are not particularly large in this general region, and changes in wind direction are confined to a small area. In the southeast quadrant of the domain there is little change in either the speed or direction of the overall flow. For the most part, modifications to the low-level air flow occur only over those areas over the *Greater Phoenix* region that experienced changes in land cover. Once air enters the northern tier of the *Greater Phoenix* region, toward the central portion of the domain, an organized line of convergence at or just south of 33.7° N becomes evident. This predominantly southwesterly flow simulated during the NLCD73 experiment veers, due to a strengthened northerly flow, in direct response to the regional landscape discontinuity created by urban development. Despite the modest increase in the

roughness length resulting from increases in urban land and shrubland (at the expense of irrigated agriculture), it is the thermal gradient that is the driving influence on the changing wind flow. Landscape heterogeneity has also augmented the wind speed over this area (positive wind speed differences), adding to the overall convergence. In other words, shifts in both wind speed and direction have aided in the establishment of low-level wind convergence. This simulated convergence pattern is several tens of kilometers in length and delineates the northern extent of the transition of urban land to shrubland.

In the southeastern region of the *Greater Phoenix* area, centered about ~ 33.4° N/111.7° W (still examining Figure 8.5 [a]), a second, stronger region of enhanced low-level convergence is evident. Urbanization in this area resulted primarily from loss of irrigated agriculture. The near-present landscape (i.e., NLCD01) has urban areas flanked by natural shrubland to the east and southwest, and by still lingering plots of irrigated agriculture to the north and south. This particular landscape patterning (urban area bounded by irrigated agriculture to the north and south, and shrubland to the southwest and east) creates a particularly strong thermal gradient. Consequently, wind vectors that have a predominantly southwesterly flow in the NLCD73 simulation veer by more than 45° in the NLCD01 simulation (note the nearly opposing wind vectors centered about 111.7° W/33.4° N). In response to daytime heating of the urban area and relative cooling due to irrigated agriculture located to the south, winds back from the primarily southwesterly orientation and provide an increasingly southerly trajectory, just north of 33.2° N. The simulated readjustment of low-level atmospheric circulation in response to the horizontal variability in landscape heterogeneity results in a compact area of nearly completely opposing wind flow. Due to the enhanced thermal gradient, contribution to

the total convergence is again aided by the increase in local wind speed (note the positive wind magnitude difference over this area). Overall, the two convergence zones loosely define an extended line of enhanced convergence, oriented in a northwest to southeast fashion, in NLCD01 compared to NLCD73. That this enhanced convergence is such a distinctive signal on the monthly timescale provides confidence that it is a robust feature resulting from changes in the underlying landscape.

Figure 8.5 [b, c] presents the monthly averaged wind speed difference (NLCD01 - NLCD73) for 1989 and 1994, respectively, at 14 LST, for the lowest atmospheric model level. As before, simulated wind vector differences between the pair of landscape reconstructions are overlaid. Compared to 1979, the overall pattern is similar, though the signal of enhanced convergence is somewhat weaker and less extensive, particularly for 1994.

Figure 8.6 [a, b, c] shows the vertical-longitude cross-section of RAMS-simulated monthly averaged u-wind difference (NLCD01 – NLCD73) for 1979, 1989, and 1994, calculated at 14 LST along 33.65 N° latitude. This figure illustrates three main points. First, the increase in simulated low-level u-wind speed centered at about -112.3° W longitude, coupled with counter flow (i.e. negative differences in u-wind) further east, for each of the three years, along with opposing wind flow in the upper portions of the PBL (indicative of the diverging portion of the cell), clearly demonstrates the significance of the change in underlying land-surface for modulating PBL flow. Second, simulated wind speed differences are greatest for 1979, with variation between the simulations exceeding 1.25 m s^{-1}. Although the magnitude is weaker for 1989, differences still exceed 1.0 m s^{-1}, while variation between the pair of landscape reconstructions is weakest for 1994. Third,

it is evident that each of the circulations, for each of the trio of years, is tilted to the east, revealing the influence of the mean flow. In 1994, the convergent component of the mesoscale circulation shows evidence of being sheared apart, away from its low-level source region. The circulations for 1979 and 1989, though tilted to the east, remain united in a single, coherent element.

Figure 8.7 [a, b, c] shows a similar comparison as Figure 8.6, for each of the three DRY years, but computed along 33.4 N° latitude (i.e., the second focused area of convergent low-level wind flow). Results for 1979 again illustrate the presence of a classic landscape-heterogeneity-induced mesoscale circulation pattern, with a distinct region of low-level convergence in the lower portions of the PBL leading to an enhancement of upper-PBL divergence. Wind speed differences between the pair of land-surface reconstructions exceed 1.5 m s^{-1}. The circulation is similar in pattern, though weaker in magnitude for 1989, although wind speed differences between NLCD01 and NLCD73 exceed 1.25 m s^{-1}. Horizontal u-wind differences for 1994 retain similarity in both pattern and magnitude but also display evidence of shearing by the background wind. As a result, the circulation, to an extent, loses the classic appearance most evident in the 1979 experiment.

In order to assess the direct impact of landscape modified wind flow on changing vertical velocity, we next present simulated monthly averaged differences in w-wind (NLCD01 – NLCD73) for 1979, 1989, and 1994, at 14 LST, for our initially diagnosed region of interest at 33.65 N° latitude (Figure 8.8 [a, b, c]). Results for 1979 illustrate the formation of a focused area of upward motion. Monthly-mean differences between the two landscape reconstructions reach to nearly 0.3 m s^{-1}. Deviations between the two

sets of experiments are less for 1989 and 1994, though upward motion is clearly enhanced for NLCD01 relative to NLCD73, for both years. Monthly mean w-wind differences (NLCD01 – NLCD73), at 33.4 N° latitude, are presented in Figure 8.9 [a, b, c] for each of the three DRY years, also at 14 LST. All three years again illustrate the systematic enhancement of vertical velocity. Moreover, the circulation for 1979 is both stronger in magnitude (peak w-wind differences exceed 0.5 m s^{-1}) and penetrates higher into the atmosphere.

Recent modeling work has begun shifting community perception regarding the influence of the background wind on the creation and maintenance of mesoscale circulations (e.g., Weaver and Avissar, 2001). It was previously thought that only under highly idealized (i.e., very low horizontal wind) synoptic-scale conditions could landscape-induced circulations develop and maintain their integrity. Here we add to the recent body of evidence that suggests the background wind may work in concert with landscape-induced mesoscale circulations, in some cases reorienting and translating these cells across the landscape, away from the location of genesis (i.e., advecting and steering them as coherent dynamical objects). Figure 8.10 [a, b] shows the monthly averaged vertical velocity difference (NLCD01 – NLCD73), for 1979, at an altitude near the location of maximum w-wind difference (924 m), at 14 LST [a] and 17 LST [b]. As seen earlier in this section, two individual circulations are observed during the mid-afternoon hours, resulting from the preferential low-level air flow arising from the underlying landscape heterogeneity. Three hours later, these circulations have been advected eastward under the influence of the background flow. These circulations are generated and similarly translated to the east for both 1989 (see Figure 8.11 [a, b]) and 1994 (see

Figure 8.12 [a, b]), though variability in shape, strength, and rate of eastward translation exists among the three case study years due to variations in the prevailing large-scale wind.

8.3 - Mesoscale Dynamics: Moisture Transport

Landscape-induced mesoscale circulations are important because of their ability to transport heat, moisture, and momentum deeper into the atmosphere than turbulent-scale eddies (e.g., Weaver and Avissar, 2001; Weaver, 2004b). We have previously shown that the change in the distribution of sensible and latent heat flux across the developing *Greater Phoenix* landscape alters low-level air flow in such a manner as to trigger preferentially located areas of enhanced vertical motion. These focused areas of rising motion contain characteristics of air from locations adjacent to the rising branch of the cell, i.e., air that is advected into the mesoscale updraft through the low-level convergence. For example, the area of low-level convergence at 33.65° N latitude includes both warmer and drier air from the north of the convergence line and cooler and moister air originating southwest of the convergence line, from nearby plots of irrigated agriculture (e.g., recall Figure 8.5 [a]).

Figure 8.13 [a, b, c] shows the vertical cross-section of RAMS simulated water vapor mixing ratio difference (NLCD01 – NLCD73) for 1979, 1989, and 1994, calculated for the entire month at 14 LST along 33.65 N° latitude. In the lower half of the PBL, air adjoining the discontinuity in landscape properties is retrieved from nearby locations. Simultaneously, the vertical circulation cell moves moist air from near the surface to higher altitudes. Consequently, the upper parts of the PBL are moistened and the lower parts dried for each of the DRY case study years. Figure 8.14 shows the same mixing

ratio difference plots, but for the circulation cell originating at 33.4° N latitude. For both cells, maximum mixing ratio differences are once again greatest for 1979 and least for 1994.

Figure 8.15 shows the 1979 monthly averaged water vapor mixing ratio differences (NLCD01 – NLCD73) for 14 LST, 17 LST, and 20 LST at 1330 meters. This height roughly corresponds to the elevation above ground level where water vapor differences between the pair of experiments are greatest, allowing us to see the maximum effect. The dense area of enhanced moistening in the center of the domain, evident at 14 LST, is amplified by 17 LST, and is mixed with the ambient air and advected east/northeastward by 20 LST, under the influence of the background flow. Although dilution has occurred by 20 LST, due to mixing with drier air from above the PBL, the eastern half of the domain still remains moister for the NLCD01 experiment as compared to the NLCD73 experiment.

This general pattern of daytime PBL moistening is similar for both 1989 and 1994 (Figures 8.16 and 8.17). The pattern, and magnitude of differences, from the 1989 experiment most resembles those from the 1979 experiment, maintaining a positive water vapor difference in the eastern region of the domain well into the evening and nighttime hours. 1994 shows a more mixed signal: by the evening and nighttime hours, water vapor enhancement in the NLCD01 experiment has virtually dissipated.

We now examine a bit more systematically the role and significance of these mesoscale circulations in the overall water vapor transport in the domain over the course of the month. We focus on 1979, because this July provides the clearest illustration of the

influence of the surface forcing on the mesoscale dynamics, in the context of the evolving large-scale background meteorology.

Just to provide a reminder of the day-to-day context for the mesoscale dynamics, Figure 8.18 shows the three-hourly accumulated rainfall in the sub-domain of interest (over the identical 1º X 1.2º region analyzed in Chapter 6.2, as outlined in Figure 6.3 [b]), over the course of July 1979, for the NLCD73, NLCD92, and NLCD01 landscape reconstructions. This figure reveals two important features. First, the entire month may be broken down into three characteristic regimes: a dry regime present during the initial half of the month, when no rainfall occurs for any of the experiments; a less-than-one-week long wet period from about July 16-21; and a second, extended dry period continuing through the end of the simulation month. Inspection of upper-air Daily Weather Maps (courtesy of the online archive available at the NOAA Central Library: http://docs.lib.noaa.gov/rescue/dwm/data_rescue_daily_weather_maps.html) of July 1979 revealed that the westward expansion of the Bermuda High reached the general vicinity of the four corners area during a one week period from about July 16 through July 21. Consequently, it was during this six day period that a considerable majority of the precipitation in Arizona fell, and RAMS was able to correctly simulate this convective activity. Second, Figure 8.18 also shows that a series of three sizeable and distinct events propagated through the domain during the wet period, with domain averaged rainfall accumulations exceeding 1 mm $3hr^{-1}$ for all three sets of landscape reconstructions. For each of these events, however, NLCD01-simulated rainfall significantly exceeded accumulations in the NLCD92 and NLCD73 experiment. During the overnight of the 19^{th}, the domain-averaged precipitation exceeded 10 mm $3hr^{-1}$ for

NLCD01, more than twice the accumulation of NLCD92 and NLCD73. This particular event was the largest of the month for all sets of experiments. Although precipitation in the NLCD92 experiment was slightly less in comparison to that in NLCD73 for this event, rainfall was enhanced for the two remaining events, leading to an overall increase in monthly averaged rainfall for NLCD92 compared to NLCD73. Though domain-mean precipitation rates are not extreme for any of the experiments, local accumulations were significant, and the memory of the land-atmosphere system may have led to subsequent impacts of the initial rainfall events on the later ones (e.g., see Anyah et al., 2007).

As discussed previously, of the major characteristics of landscape-induced mesoscale circulations is their facility in transporting heat and moisture away from the surface and out of the PBL, into the lower free troposphere. For moisture flux, this "mesoscale flux" can be calculated by multiplying the instantaneous, grid-cell deviations from the large-scale average of vertical velocity and water vapor mixing ratio. For example, as discussed in Weaver (2004b):

$$F_q = \rho L \overline{w'q'} = \rho L \overline{(w - \overline{w})(q - \overline{q})} \qquad (5)$$

where ρ is air density, L is latent heat of evaporation, w and q are vertical velocity and mixing ratio, respectively. The overbar indicates averaging over the domain, while the prime represents the deviation at each grid cell from this average.

The three-hourly mesoscale moisture flux, Fq, averaged over the 1º X 1.2º sub-domain is shown in Figure 8.19 [a, b], for the duration of the month, for NLCD01 and NLCD73, respectively, while differences (NLCD01-NLCD73) between the pair of

experiments are presented in Figure 8.19 [c]. The emphasis is on these two experiments (i.e., NLCD01 and NLCD73) because they span the widest spectrum of variability in the mesoscale dynamics. During the dry periods before and after July 16-21, mesoscale moisture flux displays a characteristic diurnal cycle for both NLCD01 and NLCD73 (see 8.19 [a, b]). However, it is apparent that more moisture is transported to higher levels in the atmosphere for the NLCD01 experiment, consistent with previous results showing enhanced vertical velocities. These differences are in excess of 100 Wm^{-2} for several days, from about July 8 - July 11 and are magnified considerably during the convective period in the middle of the month.

During the wet period, the enhanced mesoscale moisture flux evident in Figure 8.19 occurs as a result of the deep convective elements propagating through the domain (e.g., Weaver (2004b)) and the extensive cloud cover and rainfall temporarily shuts off the energy supply, i.e., surface sensible heating, for the landscape-induced mesoscale circulations.

Due to the enhanced rainfall and wetting of the soil, resulting in reduced thermal gradients across the region, mesoscale moisture flux is initially less for NLCD01 relative to NLCD73, immediately after the conclusion of convective activity. As the surface dries out, however, positive differences reassert themselves during the remainder of the month.

While mesoscale circulations represent an optimal mechanism of moisture transport, enhanced mesoscale heat fluxes in NLCD01 relative to the NLCD73 landscape, are due to turbulent processes (Figure 8.20 [a, b, c]). Figure 8.20 shows mesoscale heat flux, calculated in the same way as moisture flux but with θ instead of q. As with the mesoscale moisture flux, mesoscale heat flux displays a diurnal signature, waxing and

waning with the onset of maximum sunlight and heating resulting from the expansion of the urban area. Again, there is an enhancement for NLCD01 as compared to NLCD73 of at least 20-40 Wm^{-2} during the dry periods in the months. However, distinct from moisture flux, the peak mesoscale heat flux is confined lower in the atmosphere, well within the PBL, (consistent with earlier work). Therefore, the vertical signature of the mesoscale circulations is significantly different for moisture than for heat, with potential implications for atmospheric vertical thermodynamic structure. We examine such changes in the vertical profiles, and discuss possible implications of these changes for convection enhancement, next.

8.4 - Vertical Thermodynamic Profiles and Rainfall Enhancement

Figure 8.19 shows a similar time series of sub-domain averaged water vapor mixing ratio to the mesoscale flux results presented in Figure 8.19 and 8.20. This is revealing, for two reasons. First, for the initial half of the month (through about July 16th), large-scale subsidence is evident, consistent with the large-scale dynamical situation and the monthly averaged precipitation time series (recall Figure 8.18). On July 16th, the atmosphere begins to moisten considerably as subsidence weakens with the approach of unsettled conditions. For the next several days, mixing ratio values are at their monthly peak, before a gradual decline commences once again after the conclusion of the convective period.

Second, the diurnal presence of the mesoscale circulations, and their enhancement from NLCD73 to NLCD01, are once again evident. In particular, the surface-layer drying and upper PBL and lower free atmosphere moistening effects are apparent (Figure 8.21 [c]). This characteristic pattern of low-level drying and upper PBL moistening

reverses immediately after the wet period concludes on about July 21st. Enhanced precipitation for the NLCD01 experiment wets the soil beneath, and it takes several days for evapotranspiration to occur and once again allow the rolls to resume their daily, pre-convective period, behavior.

During most days, free atmosphere water vapor shows a characteristic diurnal increase, but there is no ongoing accumulation from one day to the next day, building up a progressively moister layer. One thing that might be occurring is that at least some of the water transported vertically by the mesoscale circulations makes it high enough to escape the PBL into the free atmosphere, where it is more easily advected out of the domain by the large-scale background wind. Figure 8.15-8.17 provides some evidence for this occurrence.

Figure 8.22 [a, b, c, d] shows the vertical evolution of θ differences (NLCD01-NLCD73), averaged over the previously defined sub-domain of interest, from July 1-16 (i.e., during the pre-convection period) for 08 LST, 11LST, 14 LST, and 17 LST. The corresponding calculations for water vapor mixing ratio difference evolution and θ_e are presented in Figure 8.23 [a, b, c, d] and Figure 8.24 [a, b, c, d], respectively. Figure 8.22 demonstrates the full heating effect due to urban expansion and illustrates the evolving build-up of low-level dry static energy during the course of the day. This excess dry static energy remains confined to the PBL even during the night-time, though differences between NLCD01 and NLCD73 diminish to about 0.1K (as shown in Figure 8.20, the heat flux due to the mesoscale circulations is confined to these low levels).

By contrast, Figure 8.23 illustrates the dual upper-PBL-moistening and surface-layer drying as a result of the mesoscale dynamics. While the peak effect of turbulent heating

due to urban expansion is confined to the surface layer, peak moistening due to the mesoscale dynamics occurs in the vicinity of the PBL top. Contributions from both heating and moistening are shown in the evolution of the θ_e profile in Figure 8.24, illustrating the relative importance of the enhanced moisture transport due to the stronger mesoscale circulations in the NLCD01 simulation.

So, the final question is, what role, if any, do these mesoscale-induced changes in the vertical thermodynamic structure of the atmosphere play in the simulated enhancement of July 16-21 precipitation in the NLCD01 simulation? The NLCD01 profiles are warmer and drier in the lower PBL but significantly moister in the upper part of the PBL (between 1-2 km, as shown in Figures 8.23 and 8.24). While this additional moist static energy does not lead to convection on most days, since the atmosphere is too dry, it is plausible that, when a storm moves into the domain, the lifting of this moister layer releases additional instability, fueling stronger updrafts and hence more convective rainfall. Close inspection of the simulated storm cells, however, reveals that the preponderance of precipitation occurs during the night-time hours, primarily after local midnight. As noted in the thermodynamical profile presented in Figure 8.24, the land-surface impact on vertically distributed moist static energy is greatest during mid- to late afternoon, begins to dissipate during the evening, and is least during night-time (i.e., profile differences are smallest during the time of greatest rainfall frequency). Consequently, the direct dynamical forcing resulting from landscape forced mesoscale circulations does not seem to be the explanation for either the initial storm enhancement or the subsequent rainfall events.

Rainfall enhancement may also take place indirectly, through the gradual accumulation of moist static energy within the PBL. Figure 8.21 [c] does indicate that moisture transport is enhanced for the NLCD01 experiment, in the upper reaches of the PBL, relative to the NLCD73 experiment, on a diurnal basis. However, with the gradual waxing of moisture resulting from landscape-induced mesoscale circulations appears a waning of equal magnitude as the background flow advects the air out of the fine grid, suggesting that the indirect mechanism is also unlikely to play a large role in precipitation enhancement.

While the cause of initial triggering, and to a certain degree, the maintenance, of the precipitation enhancement remains unknown, one mechanism that is likely to play an important role in maintaining the difference in precipitation between NLCD01 and NLCD73 is recycling. Figure 8.25 shows the simulated domain averaged (refer to Figure 6.3 [b] for extent of averaging domain) latent heat flux difference (NLCD01 minus NLCD73) for 1979. Constantly negative values during the first half of the month indicate that NLCD73 evapotranspiration is greater than that of NLCD01, consistent with results presented earlier. As the ensuing period of convective activity approaches, however, differences become positive as NLCD01 evapotranspiration exceeds that of NLCD73. Immediately after the initially enhanced rain event, the subsequent day's additional water moistens the atmosphere and aids to further feed rainfall enhancement. As the convective period ends the diurnal pattern of greater NLCD73 evapotranspiration resumes again once the extra soil water from the additional rainfall has evaporated and moved out of the domain.

The importance of the large-scale environment, in terms of storm movement during 1979, and its effect on precipitation recycling requires further explaining. Precipitation recycling may be enhanced if cell motion follows similar trajectories over a period of several days, a feature that was noted during the 1979 simulations, but was largely absent during 1989 and 1994. During 1994, for example, convective elements moved through the domain from all directions with relatively equal frequency, while during 1979 convective elements traced out similar paths on successive days, feeding on the evaporated water from the previous day's rainfall.

We now briefly revisit the hypothesis outlined at the conclusion of Chapter 6 (i.e., that the accumulated landscape signal may modify regional stability sufficiently to allow for repeated enhancement of storm cells). Re-examination of the hypothesis based on the results presented in this Chapter reveals that the precise pathway(s) leading to precipitation enhancement resulting from the effect of enhanced warming (due to urban area expansion), and enhanced moistening (due to the presence of irrigation), is more complicated than their collective effect on the increase of moist static energy of the PBL. The interplay amongst the continuum of scales (from the turbulence to the large-scale) is more complicated than previously sketched out and warrants future research.

This chapter has showed how the interplay between three scales of motion, i.e., (1) background large-scale flow and the NAMS storm systems, (2) landscape-induced mesoscale circulations, and (3) differential turbulent heating and moistening of the PBL across the heterogeneous landscape, defines the regional weather and climate of *Greater Phoenix*, at least during climatologically dry summers. We now end with a summary of the results presented in this thesis and look ahead toward future work.

Chapter 9 - Summary and Conclusions

This thesis evaluates the climatic impact of land-use/land-cover change (LULCC) of one of the nation's most rapidly expanding metropolitan complexes, the *Greater Phoenix*, AZ, region. The focus is on the summer season, the time period wherein the North American Monsoon System (NAMS) is active and when climatic effects on the human and natural systems, due to excessive heat and flood-producing rains, are at their annual peak. We briefly summarize the most important conclusions drawn from this research.

After using satellite imagery to characterize the LULCC over the last three decades, and developing LULC classifications for our modeling work, we began by evaluating the first-order effect of LULCC over *Greater Phoenix* using high-resolution (2-km grid spacing) Regional Atmospheric Modeling System (RAMS) simulations of three "wet" and three "dry" summer seasons. Experiments were carried out with two different land cover reconstructions for the region: a circa-1992 representation based on satellite observations and a hypothetical "pre-settlement" scenario where the anthropogenic landscape of irrigated agriculture and urban pixels was replaced with current semi-natural vegetation. The main findings are as follows:

- The presence of extensive irrigated agriculture adjacent to the urban area dampens the regional-mean warming due to urbanization.
- The imposed LULCC produces a systematic increase in precipitation to the north and east of the city during dry summers.

Using the above methodology and results as a guide, we next examined the impact of the actual landscape evolution that occurred over the last three decades on the *Greater*

Phoenix regional climate. LULC reconstructions based on circa-1973, circa-1992, and circa-2001 satellite data were used. The main findings are as follows:

- From 1973 to 2001, areal coverage of irrigated agriculture declined and that of urban areas increased, resulting in significantly greater simulated regional-mean temperatures for the 2001 than for the 1973 LULC.
- As with the 1992 to pre-settlement comparison, precipitation is enhanced for the 2001 compared to the 1973 landscape during dry summers. In addition, rainfall enhancement relative to the 1973 LULC is increased for 2001 relative to the 1992 LULC.
- Heterogeneity in the surface fluxes produces preferentially located mesoscale circulations on most days that are stronger for the 2001 compared to the 1973 LULC, due to the increased planetary boundary layer (PBL) heating via enhanced turbulent heat flux.
- The effect of these stronger circulations is to warm and dry the lower part of the PBL and moisten the upper part of the PBL for 2001 relative to 1973.
- The precise physical pathway(s) whereby precipitation enhancement occurs with evolving landscape reveals a complicated interplay among scales that warrants future research.

Methodological factors that may affect these results include an underestimate of urban warming, as RAMS does not include a sophisticated urban parameterization scheme. This hindered our ability to account for some urban processes known to enhance the UHI effect. While RAMS was able to reproduce the daytime UHI effect with reasonable fidelity, the nighttime UHI had a cold bias, due to the lack of daytime heat

trapping within the three-dimensional urban complex and decreased nighttime urban longwave cooling as compared to rural localities, due to failure to account for a reduction in sky view factor (SVF). Coupling a comprehensive urban canopy model to the RAMS land-surface scheme would improve the model's overall capability for simulating the diurnal UHI, along with a number of other urban-scale meteorological processes and effects. As these model improvements would likely have resulted in an increased warming due to the presence of urban areas, we suggest that the findings from the simulations presented here represent a conservative estimate, or lower bound, on the impact of LULCC on near-surface temperature temperatures, mesoscale dynamics, and possibly rainfall in the *Greater Phoenix* area.

Additionally, cooling resulting from irrigated agriculture, due to our assumption of soil saturation, may be overestimated. To test the sensitivity of this assumption, we performed a repeat of the control experiment whereby we forced the irrigated agricultural land cover type to field capacity at each model time step. With this change, cooling from the agricultural zones decreased considerably, with widespread drying over a majority of the domain, and the effects of urbanization dominated the domain-average signal. Our assumption of soil saturated irrigated agriculture, however, produced better simulation results compared to observations of temperature and dew-point, possibly because it effectively accounts for additional water sources not explicitly modeled, such as mesic landscaping and surface water reservoirs.

With the goal of presenting a more unambiguous synopsis, Figure 8.26 illustrates a qualitative summary of the questions answered as part of this thesis along with some of the unresolved issues still remaining. The top row of rectangles defines the extent of the

fine grid domain and illustrates, in a qualitative manner, the quantity of irrigated agriculture and urban land (i.e. the two chief landscapes considered in this work) contained therein. The leftmost rectangle marks the earliest point in time, corresponds with our Pre-Settlement landscape (i.e. no irrigated agriculture and no urban land), while the rightmost rectangle marks the furthest point in time, corresponding to the NLCD01 landscape. The thermal impact of the evolution of the *Greater Phoenix* landscape may be subdivided into two primary elements: (1) the effect due to changing coverage of irrigated agriculture, and (2) the effect due to changing coverage of urban land, from the Pre-Settlement to the NLCD01 landscape. The thermal impact of continued urbanization has caused a constant increase in temperature while the effect of changing irrigated agriculture forced a non-linear response that initially resulted in lowered temperatures (due its initial presence) before warming ensued (due to decreases in irrigated agricultural coverage). The main question is what, if any, are the reinforcing/competing roles of urbanization and irrigated agriculture in driving changes in precipitation? While results presented from 1979, and to a lesser extent 1989, point toward a complex interaction between the turbulent, mesoscale, and large scales, pathways whereby this enhanced precipitation is initially triggered, and to some extent, maintained, remain elusive.

Finally, current population projections of the *Greater Phoenix* area suggest that the region may surpass 10 million inhabitants by 2050 (GP Regional Atlas, 2003). Continued landscape conversion, at the expense of both natural shrubland and still lingering plots of irrigated agriculture, is expected to parallel unrelenting population rise, despite the climatological scarcity of water. How future projections of the area's landscape would impact weather and climate is thus of vital concern. In particular,

analysis of the effect of future landscape change in context of future projections of large-scale climate (i.e., under a globally warmer scenario) may provide us with the ability to better understand the full range of anthropogenic impact over this area.

Through this work, we gained an improved understanding of how landscape conversion over the *Greater Phoenix* area may have influenced both the low-level thermal environment, the vertical thermodynamic environment, and the possible effect on convective rainfall. These climatological factors are of vital importance and should be directly investigated at the regional and local scales of human activity, as we have tried to do here. The use of high-resolution modeling, allowing us to investigate the interactions between three distinct scales of atmospheric dynamics – turbulent/boundary layer scales, the mesoscale, and the large-scale environment of the NAMS – and furthermore how the evolving landscape of Phoenix changed these interactions over time, has proven to be a valuable approach toward this end. With the IPCC (2007) suggesting increasingly warm and dry conditions in the U.S. Southwest over the next century, and no end in sight to the growth and development of *Greater Phoenix*, we will need to continue to focus on these issues and use all available approaches to improve our understanding of the complex system of climate change, LULCC, and human and natural impacts.

Appendix A

Mathematically, Pielke (2002) represents albedo, for use in regional models, as a linear sum of two components:

$$A = A_z + A_s \quad \text{(A.1)}$$

where A_z represents the effect of solar zenith angle and A_s is a function of the soil wetness. He notes that the addition to the total albedo due to variations in zenith angle may reach values as large as 0.1 for sun angles residing 10-degrees above the horizon. However, current estimates suggest that the contribution to surface absorbed net shortwave energy when solar zenith angle (SZA) is large is small compared to increases in absorbed shortwave near solar noon (Wang et al., 2005) implying that accounting for SZA variability may be of greater significance during mid-day hours when the impact on the surface radiation balance is greatest. Specifically, Wang et al. (2005) used MODIS data and a Bidirectional Reflectance Distribution Function (BRDF), in conjunction with in situ albedo data over thirty desert locations around the world, to document the dependence of reflectance on changing SZA. They derived a formulation to better account for this variability. Implementing their formulation into the Noah land-surface model, the authors found increases of absorbed surface solar radiation of 16, 20, and 38 W m^{-2} at times of high sun angle, with decreases less than 5 W m^{-2} at low sun angles, as less solar radiation is incident during this time, compared to a simulation with no SZA dependency. The majority of the additional solar energy (76%) is used to increase the sensible heat flux, 18% is transferred to the soil, and the remaining energy is used to

increase the ground temperature between 0.3 ºC and 0.7 ºC, for the three sensitivity tests using the SZA formulation. In addition, the authors also validated MODIS data with in situ measurements, including those made by Idso et al. (1975) over a bare Avondale loam soil in Phoenix, and they note the largest differences due to SZA (0.01) in the shortwave band occur near solar noon over a plot of dry soil, with MODIS estimates being lower in comparison to the in situ observations. Jin et al. (2003) also evaluated MODIS albedo data against site measurements at Surface Radiation Budget Network (SURFRAD) and Cloud and Radiation Testbed/Southern Great Plains (CART/SGP) stations and found surface shortwave summertime 16-day mean in situ measurements over a sparsely vegetated region in Desert Rock, NV, to be stable about a value of 0.21 and in good agreement with MODIS data. Albedo values lower than 0.2 were obtained at a site in Colorado exhibiting greater fractional vegetation, including a mixture of desert shrubs, cacti, and grasses.

The albedo dependency on soil wetness is an empirically derived function. Pielke (2002) describes this dependency, based on work by Idso et al. (1975) for an Avondale loam soil as:

$$A_S = \begin{cases} 0.31 - 0.34\eta/\eta_s, & \eta/\eta_s \le 0.5 \\ 0.14, & \eta/\eta_s > 0.5 \end{cases} \quad \text{(A.2)}$$

where η/η_s is a measure of the ratio of volumetric moisture content (η) to the soil porosity (η_s). The bare soil albedo is thus expected to be highest (lowest) for dry (wet) soils with a large (small) solar zenith angle. A.2 represents the manner in which RAMS calculates soil albedo. Clearly, the dependency of (A.2) is reliant on soil moisture and thus, on soil texture as well. Accordingly, for a Florida peat soil, the functional form of the albedo is

represented by a maximum value of 0.14, as opposed to the 0.31 specified in (A.2) (Pielke, 2002). Functional forms of albedo dependency on soil water content are not available for all soil texture types and much care must be taken when calculating albedo over distinctly different regions with other soil textures.

The measurements made and discussed by Idso et al. (1975) of an Avondale loam soil were conducted over the Phoenix area over a "smooth, bare field". To assess the impact on resulting albedo values due to a plot of soil with roughness elements on the order of 1 cm, additional observations were conducted that showed absolute soil albedo values decreased by 0.04 as compared to its smooth surface counterpart. The authors noted that the difference in measured albedo depended on the soil wetness and increased with drier soil – differences of 0.02 were determined for wet soil and 0.04 for initially irrigated soil allowed to dry for a period of five days. Thus, for a dry, non-smooth soil over the Greater Phoenix area, (A.2) may be re-written as:

$$A_S = \begin{cases} 0.27 - 0.34\eta/\eta_S, & \eta/\eta_S \le 0.5 \\ 0.12, & \eta/\eta_S > 0.5 \end{cases} \quad \text{(A.3)}$$

References

Abdullah, A. (2000), Monitoring land-cover change detection in an arid urban environment: a comparison of change detection techniques: Master's Thesis. West Virginia University, [On-line Abstract: https://etd.wvu.edu/etd/etdDocumentData.jsp?jsp_etdId=1410].

Adams, D. K. and A. C. Comrie (1997), The North American Monsoon, *Bull. Amer. Meteor. Soc.*, **78**, 2197-2213.

Anderson J. R., E. E. Hardy, J. T. Roach, and R. E. Witmer (1976), A land use and land cover classification system for use with remote sensor data. *U.S. Dep. Interior, Geol. Surv.*, Prof. Paper 964.

Anyah, R., C.P. Weaver, G. Miguez-Macho, Y. Fan, and A. Robock (2007), Incorporating water table dynamics in climate modeling: 3. Simulated groundwater influence on coupled land-atmosphere variability, *J. Geophys. Res.,* in press.

Arnfield, A. J. (2003), Two decades of urban climate research: A Review of turbulence, exchanges of energy and water, and the urban heat island, *Int. J. Climatol.,* **23**, 1- 26.

Avissar, R. and R. A. Pielke (1989), A parameterization of heterogeneous land surfaces for atmospheric numerical models and its impact on regional meteorology, *Mon. Weather Rev.*, **117**, 2113-2136.

Avissar, R. (1996), Potential Effects of Vegetation on the Urban Thermal Environment, *Atmos. Env.,* **30**, 437-448.

Avissar, R., E. W. Eloranta, K. Gurer, and G. J. Tripoli (1998), An evaluation of the Large-Eddy Simulation Option of the Regional Atmospheric Modeling System in a Convective Boundary Layer: A FIFE Case Study. *J. Atmos. Sci.*, **55**(7): 1109-1130.

Avissar, R. and Y. Liu (1996), Three-dimensional numerical study of shallow convective clouds and precipitation induced by land surface forcing, *J. Geophys. Res.,* **101**, 7499-7518.

Baidya Roy, S. B. and R. Avissar (2002), Impact of land use/land cover change on regional hydrometeorology in Amazonia, *J. Geophys. Res.,* **107** (D20), doi: 10.1029/2000JD000266.

Baidya Roy, S. B., G. C. Hurtt, C. P. Weaver, and S W. Pacala (2003), Impact of historical land cover change on the July climate of the United States, *J. Geophys. Res.,* **108,** (D24), 4793, doi: 10.1029/2003JD003565.

Baker, L. A., A. J. Brazel, N. Selover, C. Martin, N. McIntyre, F. R. Steiner, A. Nelson, L. Musacchio (2003), Urbanization and Warming of Phoenix (Arizona, USA): Impacts, feedbacks and mitigation, *Urban Ecosystems,* **6**, 183-203.

Balling Jr., R. C., and S. W. Brazel (1986), Temporal Analysis of Summertime Weather Stress Levels in Phoenix, Arizona, *Arch. Met. Geoph., Biocl.,* **36**, 341-332.

Balling Jr., R. C., and S. W. Brazel (1987), Diurnal Variations in Arizona Monsoon Precipitation Frequencies, *Mon. Wx. Rev*., **115**, 342-346.

Bornstein, R. D. (1968), Observations of the Urban Heat Island Effect over New York City, *J. App. Meteo.,* **7**, 574-582.

Brazel, A., N. Selover, R. Vose, and G. Heisler (2000), The tale of two climates – Baltimore and Phoenix urban LTER sites, *Clim. Res.*, **15**, 123-135.

Brenner, I. (1974), A surge of maritime tropical air – Gulf of California to the southwestern United States, *Mon. Wx. Rev.*, **102**, 375-389.

Burian, S. J., and J. M. Shepherd (2005), Effect of the urbanization on the diurnal rainfall pattern in Houston, *Hydrol. Process.,* **19** (5), 1089-1103.

Cai, M., and E. Kalnay (2004), Brief Communications: Cai and Kalnay Reply, *Nature*, **427**, 214.

Carleton, A. M., D. A. Carpenter, and P. J. Weber (1990), Mechanisms of interannual variability of the southwest United States summer rainfall maximum, *J. Climate*, **3**, 999-1015.

Cayan, D. and A. V. Douglas (1984), Urban Influences on Surface Temperatures in the Southwestern United States during Recent Decades, *J. Clim. and App. Meteor.*, **23**, 1520-1530.

Chase, T. N., R. A. Pielke Sr., T. G. F. Kittel, J. S. Barron, and T. J. Stohlgren (1999), Potential impacts on Colorado Rocky Mountain weather due to land use changes on the adjacent Great Plains, *J. Geophys., Res.,* **104** (D14), 16,673-16,690.

Davin, E. L., N. de Noblet-Ducoudre, and P. Friedlingstein (2007), Impact of land cover change on surface climate: Relevance of the Radiative Forcing Concept, *Geophys. Res. Lett.*, **34**, L13702, doi: 10.1029/2007GL029678.

DeFries, R. S., L. Bounoua, and G. J. Collatz (2002), Human modification of the landscape and surface climate in the next fifty years, *Global Change Biol.,* **8**, 438-458.

Diem, J. E., and D. P. Brown (2003), Anthropogenic Impacts on Summer Precipitation in Central Arizona, USA, The Prof. Geographer, 55(3), 343-355.

Diem, J. E. (2006), Anomalous monsoonal activity in central Arizona, USA, Geophys. Res. Lett., 33, L16706, doi: 10.1029/2006GL027259.

Ellis, A. W., M.L. Hildebrandt, W.M. Thomas and H.J.S. Fernando (2000), Analysis of the climatic mechanism contributing to the summertime transport of lower atmospheric ozone across metropolitan Phoenix, Arizona, USA, *Climate Research* **15** (2000) (1) 13–31.

Feddema, J. J., K. W. Oleson, G. B. Bonan, L. O. Mearns, L. E. Buja, G. A. Meehl, and W. M. Washington (2005), The Importance of Land Cover Change in Simulating Future Climates, *Science*, **310**(5754): 1674 – 1678.

Findell, K. L., and E. A. B. Eltahir, (2003), Atmospheric controls on soil moisture-boundary layer interactions. Part I: Framework development. *J. Hydrometeorol.,* **4**, 552-569.

Gallo, K. P., D. R. Easterling, and T. C. Peterson (1996), Notes and correspondence: The influence of land use/land cover on climatological values of the diurnal temperature range, *J. Clim.*, **9**, 2941-2944.

Gedzelman, S. D., Austin, S., Cermak, R., Stefano, N., Partridge, S., Quesenberry, S., and D. A. Robinson (2003), Mesoscale Aspects of the Urban Heat Island around New York City, *Theor. Appl. Climatol.*, **75**, 29-42.

Gibbens, R. P., Hicks, R. A., and W. A. Dugas (1996), Structure and function of C3 and C4 Chihuahan Desert Plant Communities: Standing Crop and Leaf Area Index, *J. Arid. Env.*, **34**, 47-62.

Greater Phoenix Regional Atlas (2003), *A Preview of the Region's 50-Year Future, Greater Phoenix 2100*, Arizona State University, Tempe, AZ, USA [www.gp2100.org].

Grimm, N. B., and C. L. Redman (2004), Approaches to the study of urban ecosystems: The case of Central Arizona – Phoenix, *Urban Ecosystems*, **7**, 199-213.

Grimmond, C. S. B., and T. R. Oke (1999), Aerodynamic properties of urban areas derived from analysis of surface form. *J. App. Meteor.*, **38**, 1262-1292.

Grossman-Clarke, S., J. A. Zehnder, W. L. Stefanov, Y. Liu, and M. A. Zoldak (2005), Urban Modifications in a Mesoscale Meteorological Model and the Effects on Near-Surface Variables in an Arid Metropolitan Region, *J. App. Meteorol.,* **44**, 1281-1297.

Hales, J. E. (1977), On the relationship of Convective Cooling to Nocturnal Thunderstorms at Phoenix, *Mon. Wx. Rev.*, **105**, 1609-1613.

Hamdi, R., and G. Schayes (2007), Sensitivity study of the urban heat island intensity to urban characteristics, *Int. J. Clim.*, in press, DOI: 10.1002/joc.1598.

Hansen, J. E., M. Sato, A. Lacis, R. Ruedy, I. Tegen, and E. Matthews (1998), Climate forcings in the Industrial era, *Proc. Natl. Acad. Sci. U.S.A.,* **95** (22), 12,753-12758.

Hedquist, B. C., and A. J. Brazel (2006), Urban, residential, and rural climate comparisons from mobile transects and fixed stations: Phoenix, Arizona, *J. Arizona-Nevada Academy of Science,* **38**, 77-87.

Higgins, R. W., Y. Yao, and X. L., Wang: Influence of the North American Monsoon System on the U.S. Summer Precipitation Regime. *Journal of Climate*, **10**: 2600-2622, 1997.

Higgins, R. W., K. C. Mo, and Y. Yao, Interannual Variability of the U.S. Summer Precipitation Regime with Emphasis on the Southwestern Monsoon. *Journal of Climate*, **11**: 2582-2606, 1998.

Higgins, R. W., et al. (2000), Improved US Precipitation Quality Control System and Analysis. NCEP/Climate Prediction Center ATLAS No. 7.

Homer, C., C. Huang, L. Yang, B. Wylie, M. Coan (2004), Development of a 2001 National Land Cover Database for the United States, *Photogram. Eng. Rem. Sens.*, **70**, 7, 829-840.

Houghton J. T., Y. Ding, D. J. Griggs, M. Noguer, P. J. van der Linden, X. Dai, K. Maskell, and C. A. Johnson (2001), *Climate Change (2001): The Scientific Basis – Contribution of Working Group I to the Third Assessment Report of the Intergovernmental Panel on Climate Change*, Cambridge Univ. Press, New York.

Howard, L.(1833), Climate of London deduced from meteorological observations. 3rd edition. Vol. 1. London: Harvey and Darton, 348 pp.

Huff, F. A., and S. A. Changnon Jr. (1973), Precipitation Modification by Major Urban Areas, *Bull. Amer. Meteor. Soc.,* **54**, 1220-1232.

Hsu, S. (1984), Variation of an urban heat island in Phoenix, *Prof. Geo.*, **36**(2), 196-200.

Idso, S. B., R. D. Jackson, R. J. Reginato, B. A. Kimball, and F. S. Nakayama (1975), The Dependence of Bare Soil Albedo on Soil Water Content, *J. Appl. Meteorol.,* **14,** 109-113.

Idso, C. D., S. B. Idso, and R. C. B. Jr. (1998), An intensive two-week study of an urban CO2 dome in Phoenix, Arizona, USA, *Atmos. Env.*, **35**, 995-1000.

IPCC, 2007: *Climate Change 2007: The Physical Science Basis. Contribution of Working Group I to the Fourth Assessment Report of the Intergovernmental Panel on Climate Change* [Solomon, S., D. Qin, M. Manning, Z. Chen, M. Marquis, K.B. Averyt, M. Tignor and H.L. Miller (eds.)]. Cambridge University Press, Cambridge, United Kingdom and New York, NY, USA, 996 pp.

Jacobs, L. K., G. M. Garfin, and B. J. Morehouse (2005), Climate Science and drought Planning: The Arizona Experience, *J American Water Resources Association* (JAWRA) 41(2): 437-445.

Jenerette, G. D., and J. Wu (2001), Analysis and simulation of land-use change in the central Arizona, Phoenix region, USA, *Landscape Ecology,* **16**, 611-626.

Jensen J. R.: *Introductory Digital Image Processing*, pp.318, Prentice Hall Series, 1996.

Jin, M., and J. M. Shepherd (2005), Inclusion of urban landscape in a climate model – How can satellite data help? *Bull. Amer. Meterol. Soc.,* **86**, 681-689.

Jin Y., C. B. Schaaf, C. E. Woodcock, F. Gao, X. Li, A. H. Strahler, W. Lucht, and S. Liang (2003), Consistency of MODIS surface bidirectional reflectance distribution function and albedo retrievals: 2. Validation, *J. Geophys. Res.,* **108** (D5), 4159, doi: 10.1029/2002JD002804.

Kain, J. S., and J. M. Fritsch (1992), The role of the convective trigger function in numerical forecasts of mesoscale convective systems, *Meteorol. Atmos. Phys.,* **49**, 93–106.

Kalnay, E., and M. Cai (2003), Impact of urbanization and land-use change on climate, *Nature*, **423**, 528-531.

Knowles-Yanez, K., C. Moritz, J. Fry, C. L. Redman, M. Bucchin, P. H. McCartney (1999), Historic Land Use: Phase I Report on Generalized Land Use, Central Arizona-Phoenix Long-Term Ecological research Contribution No.1., Arizona State University, Tempe, pp. 21.

Koster, R. D., et al., (2004), Regions of strong coupling between soil moisture and precipitation, *Science*, **305**, 1138-1140.

Kuchler, A. W. (1964), The potential natural vegetation of the conterminous United States: New York, American Geographical Society, Special Publication No. 36, scale 1:3,168,000.

Lee, S., H. J. S. Fernando, M. Princevac, D. Zajic, M. Sinesi, J. L. McCulley, and J. Anderson (2003), Transport and Diffusion of Ozone in the Nocturnal and Morning Planetary Boundary Layer of the Phoenix Valley, *Env., Fluid Mech.,* **3**, 331-362.

Liston, G. E., and R. A. Pielke (2000), A climate version of the Regional Atmospheric Modeling System. *Theor. Appl. Climatol.,* **66**, 29–47.

Lyons, T. J., (2002), Clouds prefer native vegetation, *Meteorol. Atmos. Phys.,* **80**, 131-140.

Maddox, R., D. McCollum, and K. Howard (1995), Large-scale patterns associated with severe summertime thunderstorms over central Arizona. *Wea. Forecasting*, **10**, 763-778.

Manley, G. (1958), On the frequency of snowfall in metropolitan England, *Quart. J. Roy. Meteor. Soc.*, **84**, 70-72.

Marshall, C. H., R. A. Pielke Sr., and L. T. Steyaert (2003), Crop freezes and land-use change in Florida, *Nature*, **426** (6), 29-30.

Marshall, C. H., R. A. Pielke Sr., L. T. Steyaert, and D. A. Willard (2004), The Impact of Anthropogenic Land-Cover Change on the Florida Peninsula Sea Breezes and Warm Season Sensible Weather, *Mon. Wea. Rev.,* **132**, 28-52.

Matsui, T., and R.A. Pielke Sr., 2006: Measurement-based estimation of the spatial gradient of aerosol radiative forcing. *Geophys. Res. Lett.*, **33**, L11813, doi:10.1029/2006GL025974.

Mesinger, F., et al. (2006), North American Regional Reanalysis, *Bull. Amer. Meteor. Soc.,* **87**, 343-360.

Myhre, G., and A. Myhre (2003), Uncertainties in radiative forcing due to surface albedo changes caused by land-use changes, *J. Climate.,* **16**, 1511-1524.

Myhre, G., M. M. Kvalevag, and C. B. Schaaf (2005), Radiative forcing to anthropogenic radiative change based on MODIS surface albedo data, *Geophys. Res. Lett.,* **32**, L21410, doi: 10.1029/2005GL024004.

Negri, A. J., R. F. Adler, L. Xu, and J. Surratt (2004), The impact of Amazonian deforestation on dry season rainfall, *J. Climate,* **17**, 1306-1319.

NRC (2005), *Radiative Forcing of Climate Change: Expanding the Concept and Addressing Uncertainties*. National Research Council, Washington, DC, http://www.nap.edu/catalog/11175.html

Oke, T. R. (1987), *Boundary Layer Climates, 2nd Edition.* Methuen, London.

Olson, J. S., 1994, Global ecosystem framework-definitions: USGS EROS Data Center Internal Report, Sioux Falls, SD, 37 p.

Parker, D. E. (2006), A demonstration that large-scale warming is not urban, *J. Climate.*, **19**, 2882-2895.

Pielke, R. A., J. H. Rodriguez, J. L. Eastman, R. L. Walko, and R. A. Stocker (1993), Influence of Albedo Variability in Complex Terrain on Mesoscale Systems, *J. Climate*, **6**, 1798-1806.

Pielke Sr., R.A., G. Marland, R.A. Betts, T.N. Chase, J.L. Eastman, J.O. Niles, D. Niyogi, and S. Running (2002), The influence of land-use change and landscape dynamics on the climate system—relevance to climate change policy beyond the radiative effect of greenhouse gases, *Phil. Trans. A. Special Theme Issue*, **360**, 1705-1719.

Pielke, R. A. (2001), Influence of the spatial distribution of vegetation and soils on the prediction of cumulus convective rainfall, *Rev. Geophys.*, **39**, 151-177.

Pielke, R. A. (2002), *Mesoscale Meteorological Modeling*, Academic Press, 676 pp.

Pielke R. A., J. Adegoke, A. Beltran-Przekurat, C. A. Hiemstra, J. Lin, U. S. Nair, D. Niyogi, and T. E. Nobis (2007), An overview of regional land-use and land-cover impacts on rainfall, *Tellus*, **59B**, 587-601.

Ray, D. K., U. S. Nair, R. M. Welch, Q. Han, J. Zeng, W. Su, T. Kikuchi, and T. J. Lyons (2003), Effects of land use in southwest Australia: 1. Observations of cumulus cloudiness and energy fluxes, *J. Geophys., Res.,* **108** (D14), 4414, doi:10.1029/2002JD002654.

Sailor, D. J., and H. Fan (2002), Modeling the diurnal variability of effective albedo for cities, *Atmos. Env.*, 36 (4), 713-725.

Schneider, N., W. Eugster, and B. Schichler (2004), The Impact of Historical Land-Use Changes on the Near-Surface Atmospheric Conditions on the Swiss Plateau, *Earth Inter.,* **8**, 1-27.

Scurlock, J. M. O., G. P. Asner, and S. T. Gower. 2001. Worldwide Historical Estimates and Bibliography of Leaf Area Index, 1932-2000. ORNL Technical Memorandum TM-2001/268, Oak Ridge National Laboratory, Oak Ridge, Tennessee, U.S.A.

Shepherd, J. M., H. Pierce, and A. J. Negri (2002), Rainfall modification by major urban areas: observations from spaceborne rain radar on the TRMM satellite, *J. App. Meteor.*, **41**, 689-701.

Shepherd, J. M., and S. J. Burian (2003), Detection of urban-induced rainfall anomalies in a major coastal city, *Earth Int.*, **7**, 1-17.

Shepherd, J. M. (2006), Evidence of urban-induced precipitation variability in arid climate regions, *J. Arid. Env.,* **67**, 607-628.

Spronken-Smith, R. A., and T. R. Oke (1998), The thermal regime of urban parks in two cities with different summer climates, *Int. J. Remote Sensing*, **19**, 2085-2104.

Stone, B. Jr. (2008), Short Communication: Urban and rural temperature trends in proximity to large US cities: 1951-2000, *Int. J. Climat.*, in press.

Trenberth, K. E. (2004), Brief Communications: Rural land-use change and climate, *Nature*, **427**, 213.

Twine, T. E., C. J. Kucharik, and J. A. Foley (2004), Effects of Land Cover Change on the Energy and Water Balance of the Mississippi River Basin, *J. Hydromet.,* **5**, 640-655.

U.S. Census Bureau (2005): http://www.census.gov/.

Vogelmann, J.E., S.M. Howard, L. Yang, C.R. Larson, B.K. Wylie, N. Van Driel, 2001. Completion of the 1990s National Land Cover Data Set for the Conterminous United States from Landsat Thematic Mapper Data and Ancillary Data Sources, *Photogr. Eng. Rem. Sens.*, **67**:650-652.

Vose, R. S., T. R. Karl, D. R. Easterling, C. N. Williams, and M. J. Menne (2004), Brief Communications: Impact of land-use change on climate, *Nature*, **427**, 213-214.

Walko, R. L., and C. J. Tremback (2000), *Regional Atmospheric Modeling System User's Guide: Version 4.*2, MRC, ASTeR internal report, ASTeR Div., Mission Research Corporation, Fort Collins, CO.

Walko, R. L., et al. (2000), Coupled-atmosphere-biophysics-hydrology models for environmental modeling, *J. Appl. Meteorol.,* **39**, 931–944.

Wang, H., A. J. Pitman, M. Zhao, and R. Leemans (2003), The Impact of Land-Cover Modification on the June Meteorology of China since 1700, Simulated using a regional climate model, *Int. J. Climat.,* **23**: 511-527.

Wang, Z., M. Barlage, X. Zeng, R. E. Dickinson, C. B. Schaaf (2005), The solar zenith angle dependence of desert albedo, *Geophys. Res., Lett.,* **32**, L05403, doi: 10.1029/2004GL021835.

Weaver, C. P., and R. Avissar (2001), Atmospheric Disturbances Caused by Human Modification of the Landscape, *Bull. Amer. Meteor. Soc.,* **82**, No.2, 269-281.

Weaver, C.P. (2004a), Coupling between large-scale atmospheric processes and mesoscale land-atmosphere interactions in the U.S. Southern Great Plains during summer: Part I. Mesoscale case studies, *J. Hydrometeorol., 5*, 1223-1246.

Weaver, C.P. (2004b), Coupling between large-scale atmospheric processes and mesoscale land-atmosphere interactions in the U.S. Southern Great Plains during summer: Part II. Large-scale-mean impacts of the mesoscale, J. Hydrometeorol., 5, 1247-1258.

Wei, X., A. N. Hahmann, R. E. Dickinson, Z.-L. Yang, X. Zeng, K. J. Schaudt, C. B. Schaaf, and N. Strugnell (2001), Comparison of albedos computed by land surface models and evaluation against remotely sensed data, *J. Geophys. Res.,* **106** (D18), 20,687-20,702.

Wichansky, P.S., L.T. Steyaert, R.L. Walko, and C.P. Weaver (2008), Evaluating the effects of historical land cover change on summertime weather and climate in New Jersey: Part I: Land cover and surface energy budget changes, *J. Geophys. Res.,* in press.

Zehnder, J. A. (2002), Simple Modifications to Improve Fifth-Generation Pennsylvania State University-National Center for Atmospheric Research Mesoscale Model Performance for the Phoenix, Arizona, Metropolitan Area, *J. App. Meteorol.,* **41**, 971-979.

Zeng, Z., M. Shaikh, Y. Dai, R. E. Dickinson, and R. Myneni (2002), Coupling of the Community Land Model to the NCAR Community Climate Model, *J. Climate*, **15**, 1832-1854.

Zeng X., R. E. Dickinson, A. Walker, M. Shaikh, R. S. DeFries, J. Qi (2000), Derivation and evaluation of global 1-km fractional vegetation cover data for land modeling, *J. App. Meteor.*, **39**(6), 826-839.

Zhong S., and J. C. Doran (1998), An evaluation of the importance of surface flux variability on GCM-scale boundary-layer characteristics using realistic meteorological and surface forcing, *J. Clim.,* **11**, 2774-2788.

Zhou, L., R. E. Dickinson, Y. Tian., X. Zeng, Y. Dai, Z.-L. Yang, C. B. Schaaf, F. Gao, Y. Jin, A. Strahler, R. B. Myneni, H. Yu, W. Wu, and M. Shaikh (2003), Comparison of seasonal and spatial variations of albedos from Moderate-Resolution Imaging Spectroradiometer (MODIS) and Common Land Model, *J. Geophys. Res.,* **108** (D15), 4488, doi: 10.1029/2002JD003326.

	R^2 Value	Equation
Band 1	0.89	y = 0.6953x + 17.422
Band 2	0.91	y = 0.8758x + 9.755
Band 3	0.90	y = 0.9039x + 7.3033
Band 4	0.90	y = 0.8976x + 7.6168

Table 3.1 R-squared values and corresponding equations obtained from selection of ten comparatively time-invariant features used in the normalization process of 1973 MSS image. Baseline image used was the 1992 MSS data. Values are rounded to the nearest hundreth of a decimal.

LEAF-2 Class	α	ε	LAI	vfrac	zo
Water	0.14	0.99	0.0	0.0	0.00
Barren	0.21	0.86	0.5	0.33	0.05
Shrubland	0.19	0.95	0.5	0.19	0.18
Urban Low Intensity	0.16	0.90	0.4	0.40	0.50
Urban High Intensity	0.16	0.88	0.2	0.26	0.50
Grassland	0.18	0.96	0.5	0.43	0.13
Irrigated Agriculture	0.18	0.95	6.0	0.75	0.06
Evergreen Needle-leaf	0.11	0.96	5.0	0.68	1.00

Table 3.2 Landscape classification used for all numerical experiments. Also shown are the biophysical parameters used in LEAF-2 land-use class description. α = albedo; ε = emissivity; LAI = Leaf Area Index; vfrac = vegetation fraction; zo = roughness length (m).

Landscape Conditions	Year from which Initial and Boundary Conditions were used to force RAMS	
	WET Years	**DRY Years**
Pre-Settlement	1990, 1984, 1983	1994, 1989, 1979
NLCD73	1990, 1984, 1983	1994, 1989, 1979
NLCD92	1990**, 1984, 1983	1994, 1989, 1979
NLCD01	1984, 1984, 1983	1989, 1989, 1979

Table 4.1 Summary of all 24 experiments performed. For each experiment, the analysis time consists of the period lasting from July 1, 12Z through July 31, 12Z. ** denotes experiment used as Control simulation and validated against observations.

Dry Monsoon Years	Wet Monsoon Years
1960	1963
1962	1967
1973	1983
1978	1984
1979	1986
1989	1990
1994	

Table 4.2 Years determined as unseasonably DRY or WET monsoons for a southwest U.S. region centered over Arizona and bounded by: lat. 30N-38N – lon. 117W-107W. All selected years, for both the dry and wet sample, were at least 1 standard deviation below and above the long-term (1948-1998) seasonal (JAS) precipitation mean, respectively.

Station	Latitude [°]	Longitude [°]	Simulated Average Daily Maximum [C]	Observed Average Daily Maximum [C]	Simulated Average Daily Minimum [C]	Observed Average Daily Minimum [C]
Sky Harbor	33.43	-112.02	37.7	39.7	24.2	29.1
Phoenix Encanto	33.47	-112.09	37.7	36.6	24.2	26.4
Phoenix Greenway	33.62	-112.10	36.6	36.1	23.1	27.0
Eloy	32.77	-111.55	33.0	35.9	21.7	25.4
Litchfield	33.47	-112.39	34.6	37.2	23.3	26.2
Maricopa	33.07	-111.97	34.2	35.8	22.8	24.3
Monthly Mean			35.6	36.9	23.2	26.4

Table 5.1 Daily maximum and minimum monthly temperature comparison between RAMS simulated control experiment, AZMET stations, and first order National Weather Service station (Sky Harbor) observations for July 1, 12Z - July 31, 12Z, 1990. Also shown is monthly accumulated precipitation [mm] and monthly averaged soil temperature [°C] comparison at two levels (see text for details).

Coop Station	Latitude [°]	Longitude [°]	RAMS Monthly Temperature Average [C]	COOP Station Montly Temperature Average [C]	RAMS Monthly Precipitation Total [mm]	COOP Station Monthly Precipitation Total [mm]
Buckeye	33.38	-112.58	27.0	32.7	18.0	54.1
Casa Grande	32.88	-111.75	26.1	32.3	37.0	35.6
Casa Grande National Monument	33.00	-111.53	25.4	31.7	59.3	38.9
Chandler Heights	33.22	-111.68	27.1	31.5	82.0	30.0
Florence	33.03	-111.38	24.9	31	70.1	75.7
Gila Bend	32.95	-112.72	30.8	34	3.5	30.2
Laveen 3 SSE	33.33	-112.15	25.9	33.3	40.2	70.9
Litchfield Park	33.50	-112.37	27.1	32.5	59.1	50.8
Maricopa 4N	33.12	-112.03	27	32.6	56.1	87.1
Phoenix City	33.45	-112.07	29.4	33.9	34.3	46.7
Sacaton	33.07	-111.75	27	32.6	57.3	12.7
Tempe ASU	33.42	-111.93	28.9	32.8	48.5	47.8
Monthly Mean			27.2	32.6		

Table 5.2 Monthly averaged temperature and accumulated precipitation [mm] comparison between RAMS-simulated control experiment and Cooperative (COOP) meteorological stations.

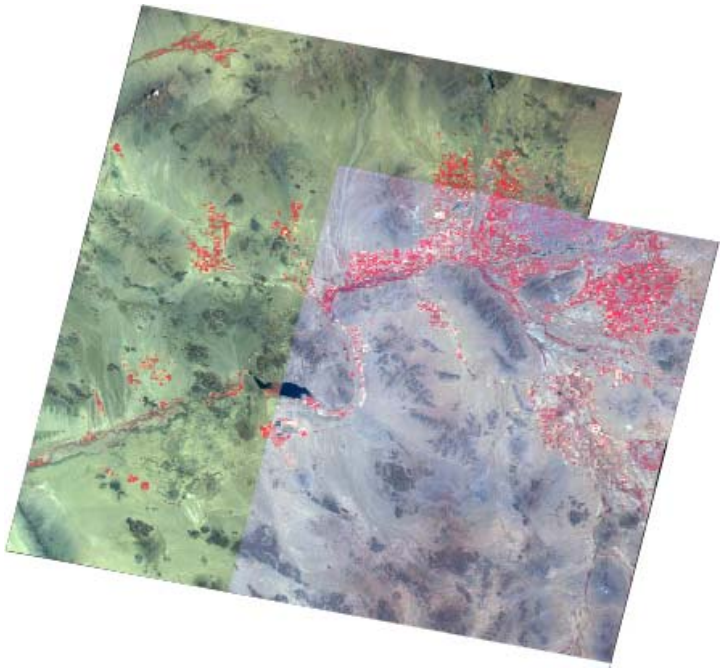

(a)

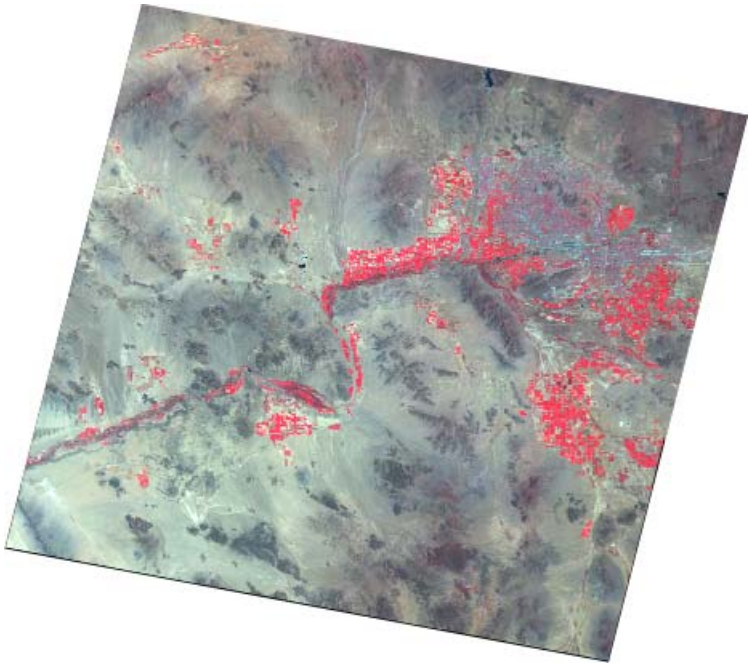

(b)

Figure 3.1 (a) Mosaicked MSS image, consisting of separate data obtained from 1973 and 1975. A 4-2-1 R-G-B (NIR band, red band, and green band, respectively) depiction is presented; **(b)** as (a) but for an image obtained on July 26, 1992.

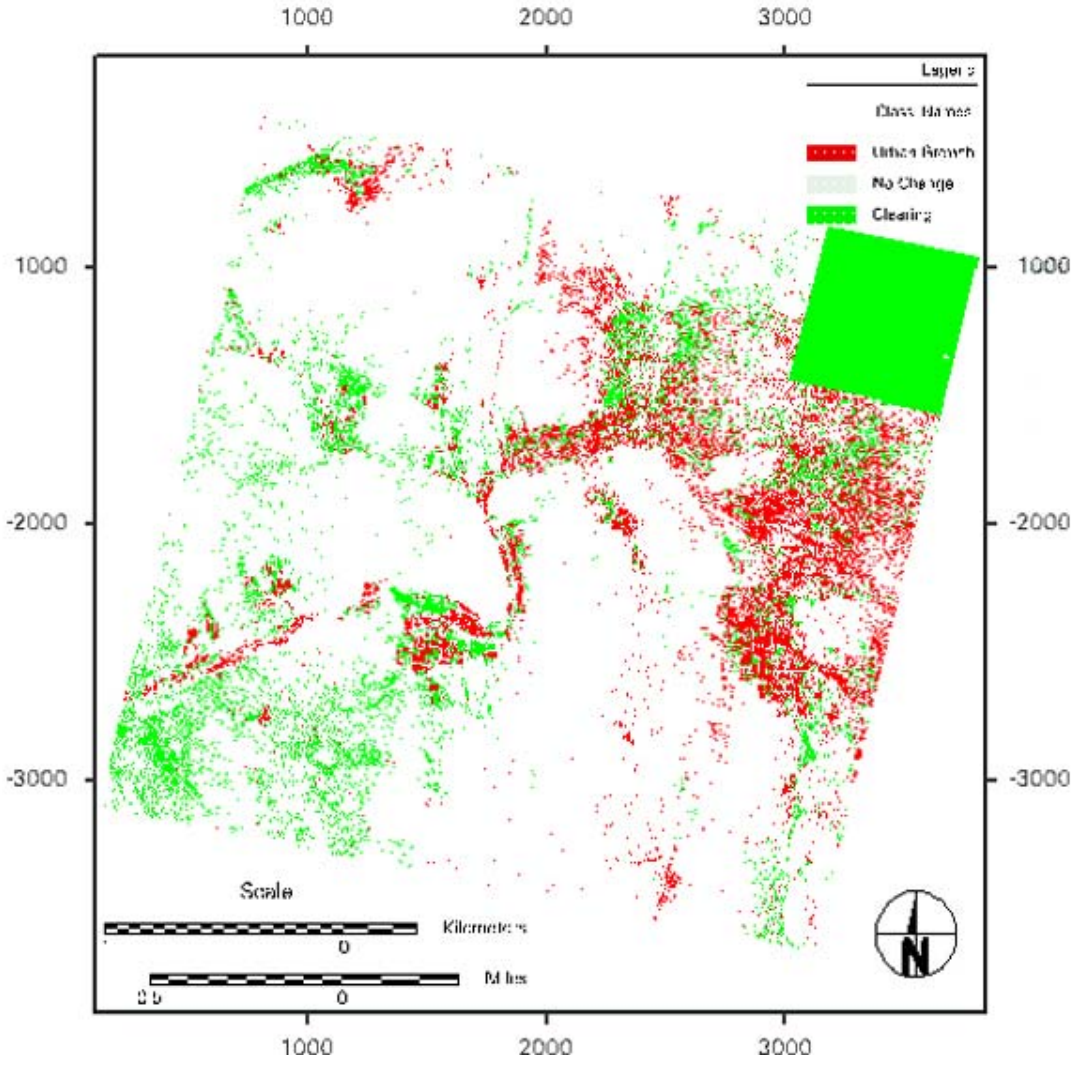

Figure 3.2 Red band differenced image: 1992 Landsat MSS minus mosaicked 1970s Landsat MSS. Red pixels were classified as a decrease in red band reflectance data with time and are commonly associated with urban growth. Green pixels were classified as an increase in red band reflectance data from 1973 to 1992 and are commonly associated with clearing.

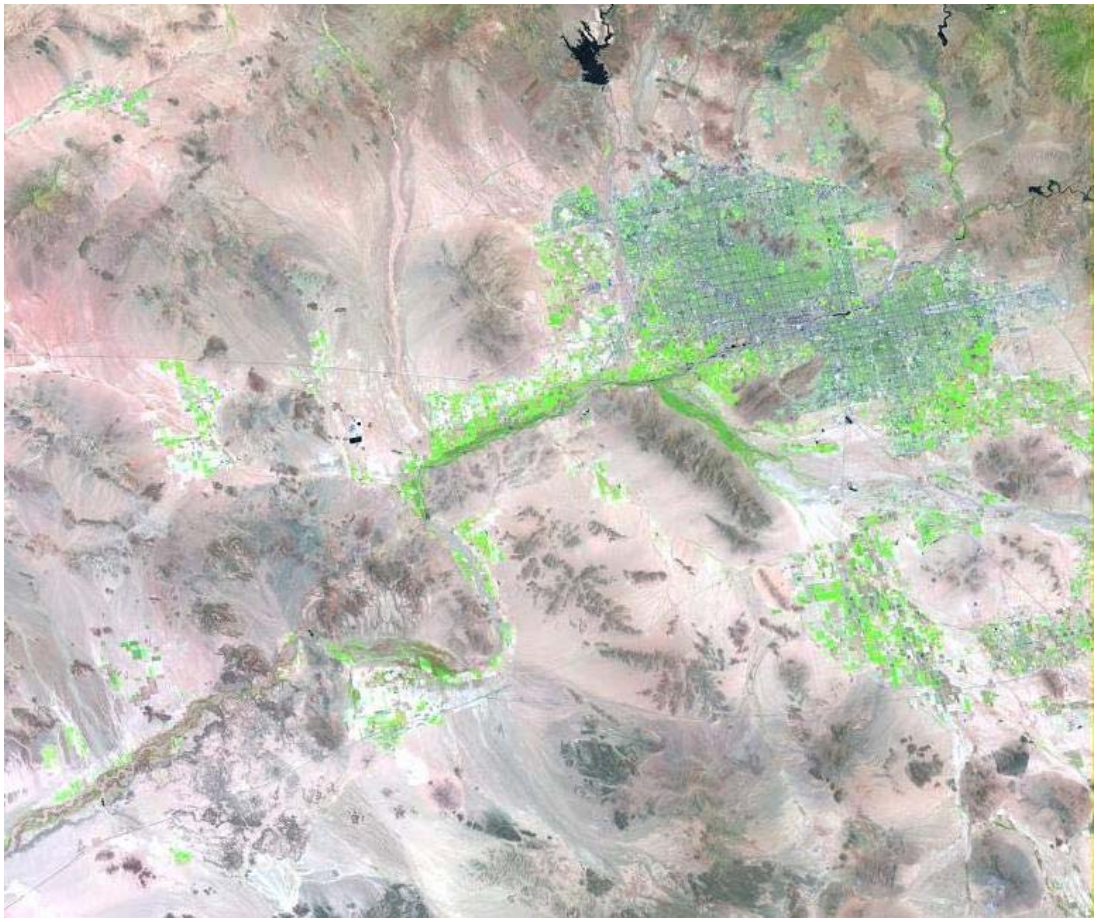

Figure 3.3 Aerial view of the *Greater Phoenix* area as seen from a Landsat 7 image acquired on May 21, 2000. Agricultural pixels are displayed in green, the urban landscape is represented by turquoise pixels, and natural shrubland is shown as varying shades of brown.

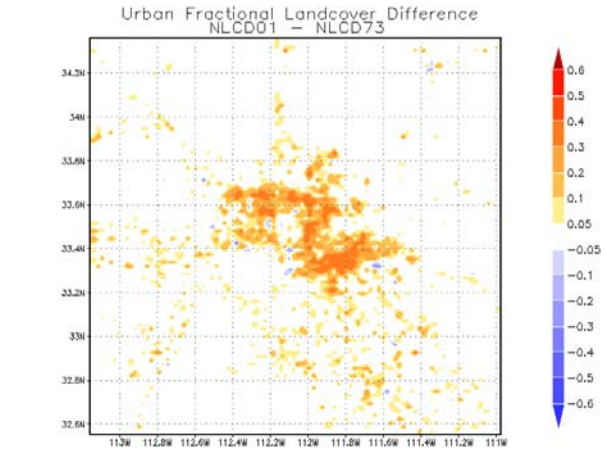

(a)

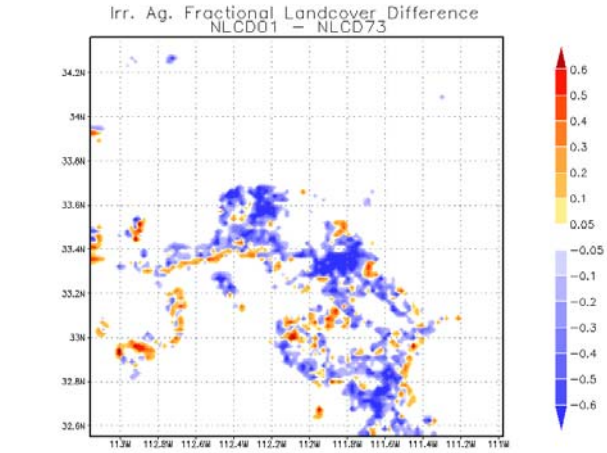

(b)

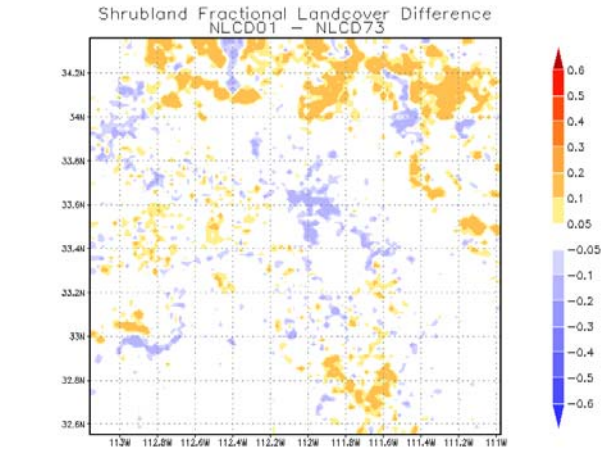

(c)

Figure 3.4 GRID 3 fractional landcover difference (NLCD01 fraction of total area minus NLCD73 fraction of total area), in **(a)** urban land area, **(b)** irrigated agriculture land area, and **(c)** shrubland area.

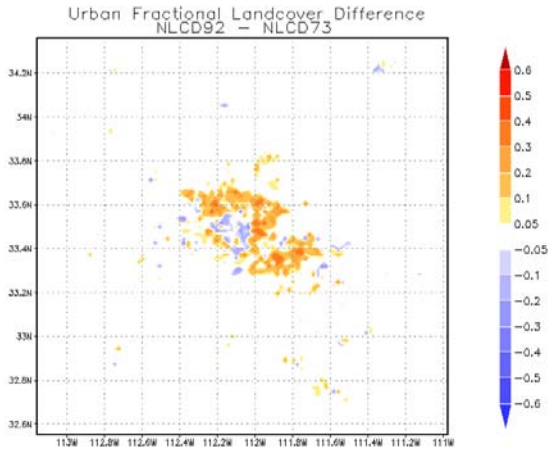

(a)

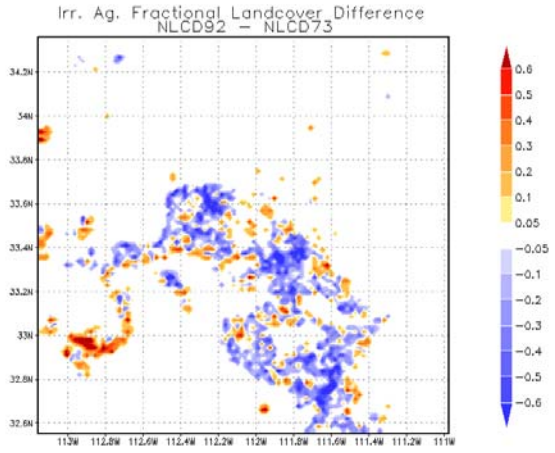

(b)

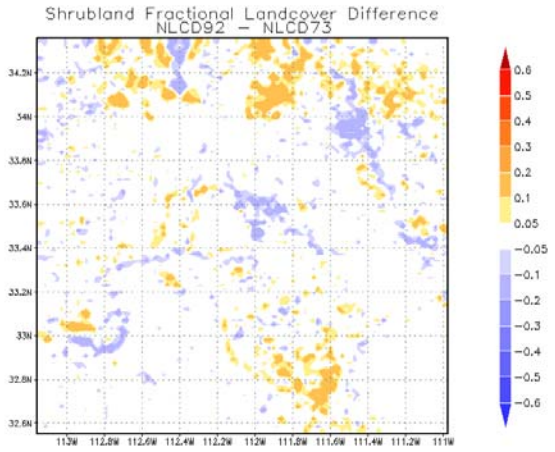

(c)

Figure 3.5 GRID 3 fractional landcover difference (NLCD92 fraction of total area minus NLCD73 fraction of total area) in **(a)** urban land area, (**b)** irrigated agriculture land area, and **(c)** shrubland area.

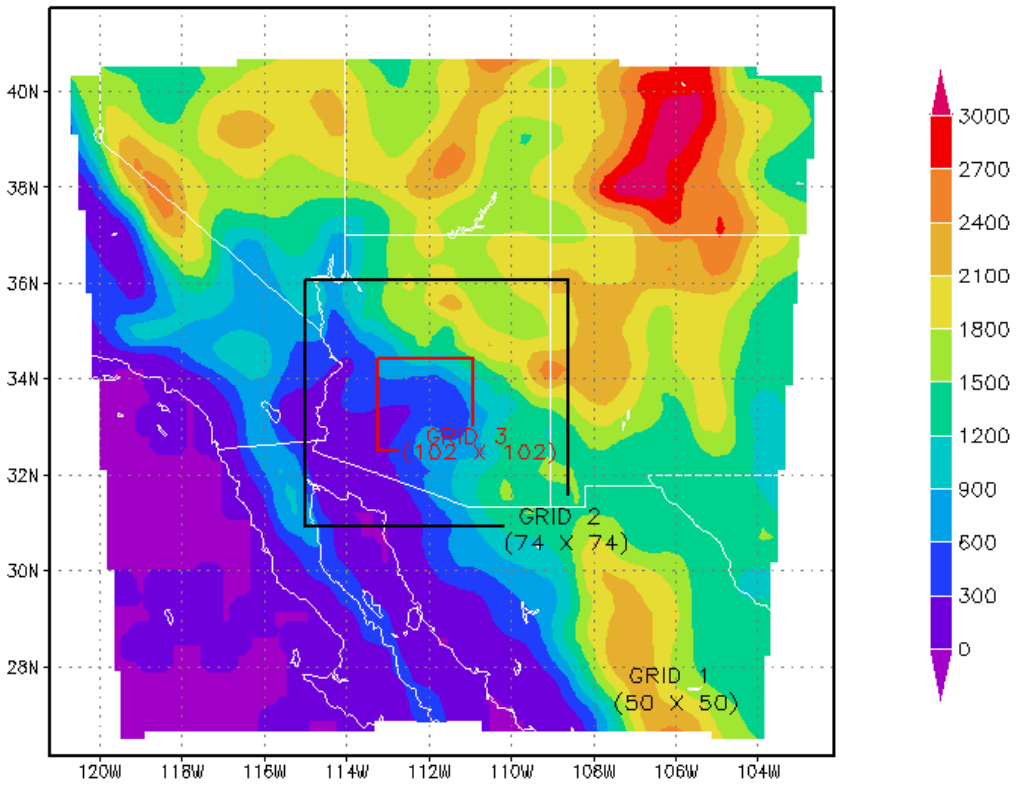

Figure 4.1 Geographical representation of the RAMS nested grid configuration with topography overlaid and the number of grid cells for each grid shown as numbers in parentheses.

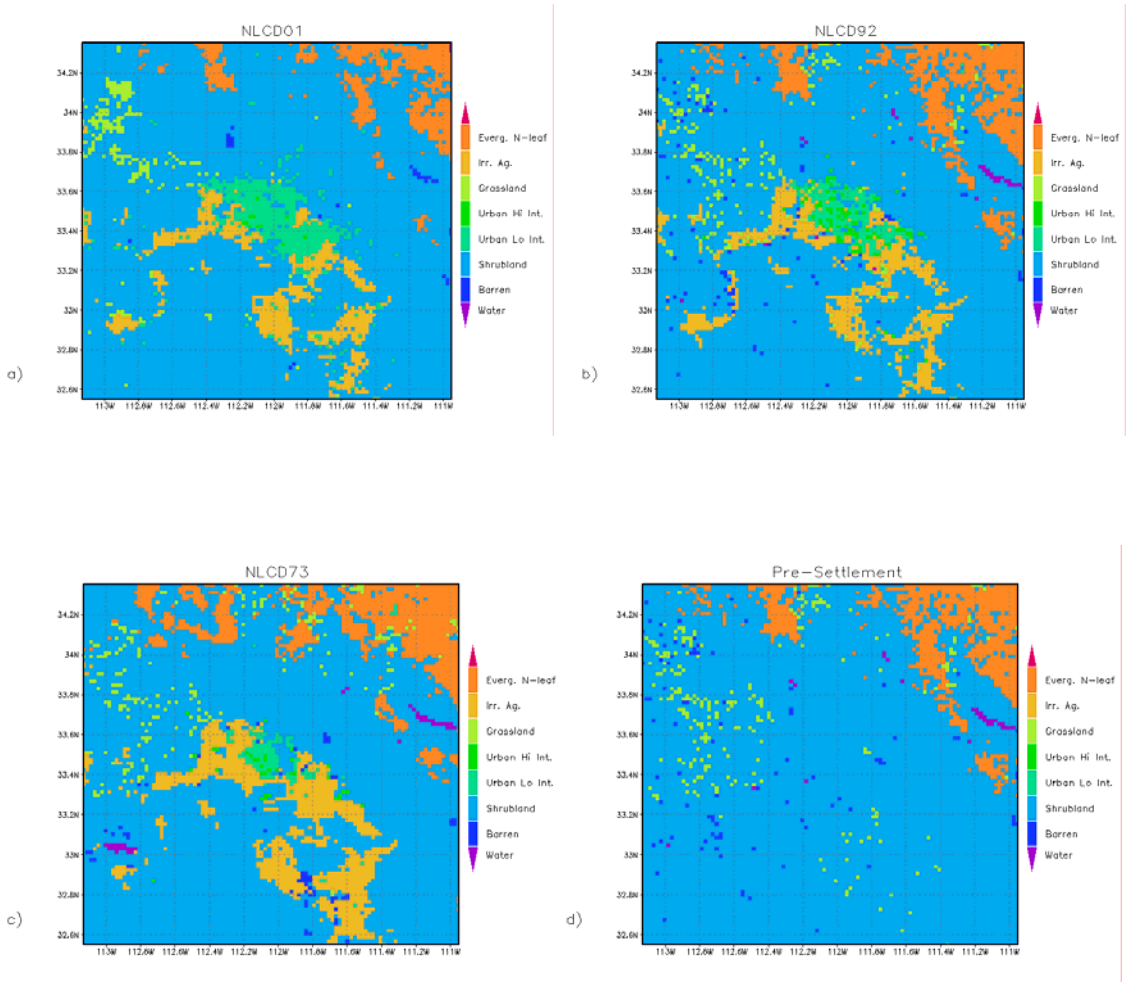

Figure 4.2 Dominant LULC representation for GRID 3 making use of **(a)** NLCD01, **(b)** NLCD92, **(c)** NLCD73, and **(d)** Pre-Settlement landscape conditions used as surface boundary conditions.

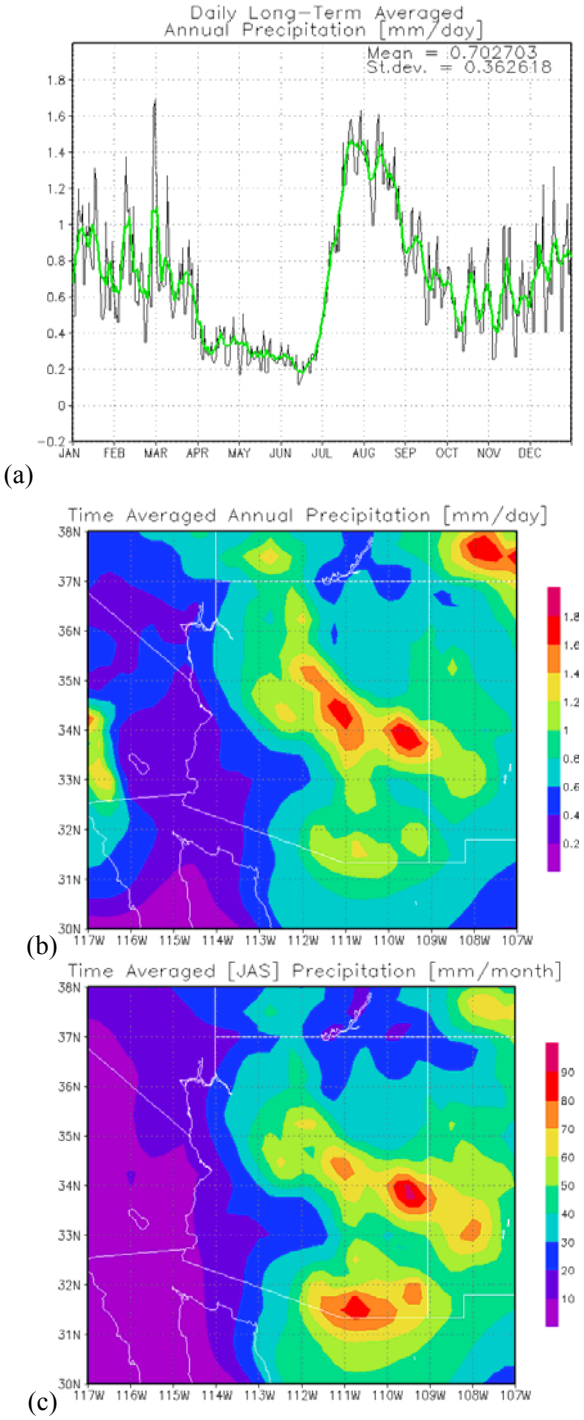

Figure 4.3 (a) Yearly evolution of daily domain-average precipitation (black line) and seven day running-mean (green line) calculated for the period 1948-1998. Mean and standard deviation correspond to yearly evolution of domain average precipitation. Units are mm day $^{-1}$; **(b)** time averaged annual distribution of precipitation calculated for the period 1948-1998. Units are mm day $^{-1}$; **(c)** Time averaged [Jul-Aug-Sep] seasonal distribution of precipitation calculated for the period 1948-1998. Units are mm month $^{-1}$.

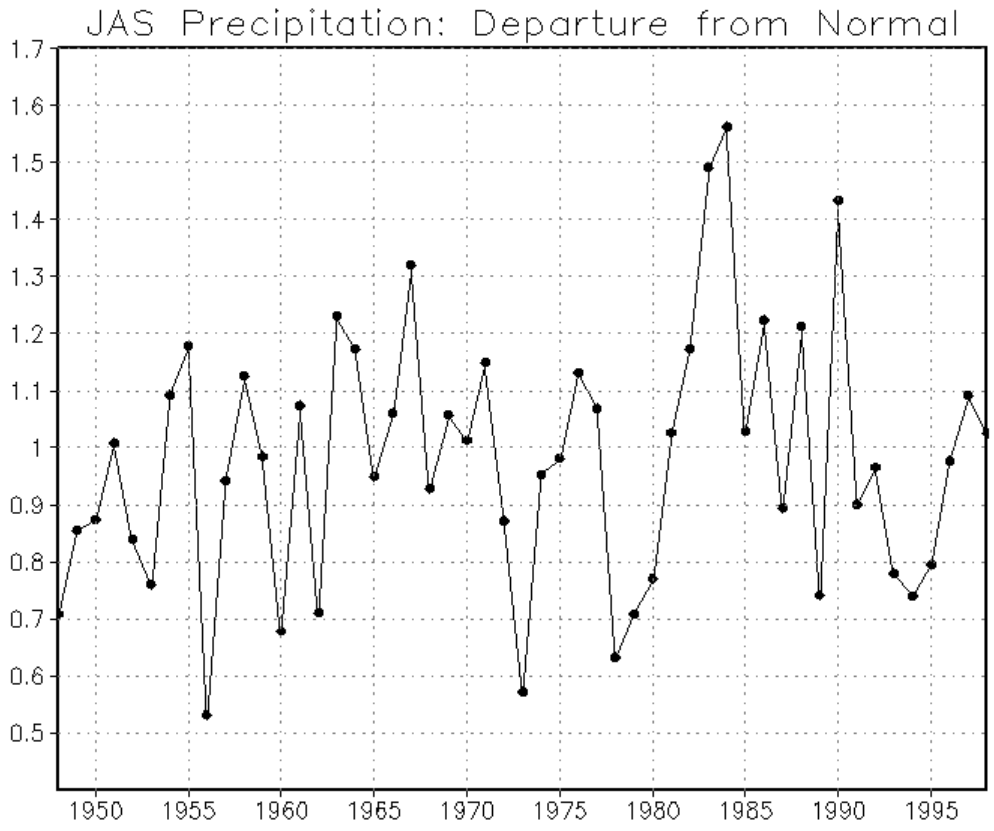

Figure 4.4 Fraction of seasonal (Jul-Aug-Sep) domain-averaged precipitation with respect to 1948-1998 Jul-Aug-Sep mean. Values above one correspond to wetter than normal monsoon periods and values below one correspond to drier than normal monsoon periods.

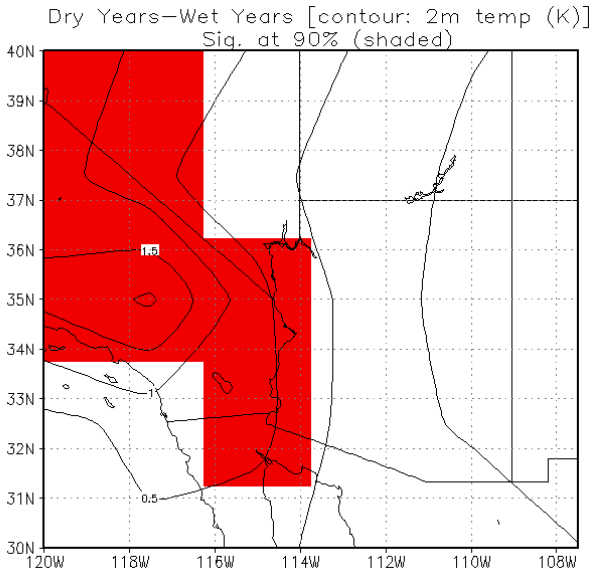

(a)

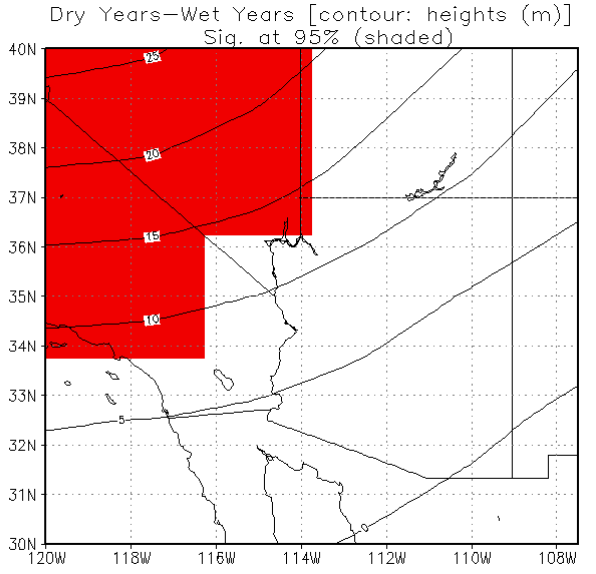

(b)

Figure 4.32: (a) Seasonally averaged [Jul-Aug-Sep] 2-m temperature difference between dry monsoon years and wet monsoon years [see Table 1]. Contour intervals are shown every 0.5 K. Red shading indicates geographical areas where difference between samples is significant at 90% level. **(b)** Seasonally averaged [Jul-Aug-Sep] 500mb geopotential height difference between dry monsoon years and wet monsoon years [see Table 1]. Contour intervals are shown every 5 m. Red shading indicates geographical areas where difference between samples is significant at 95% level.

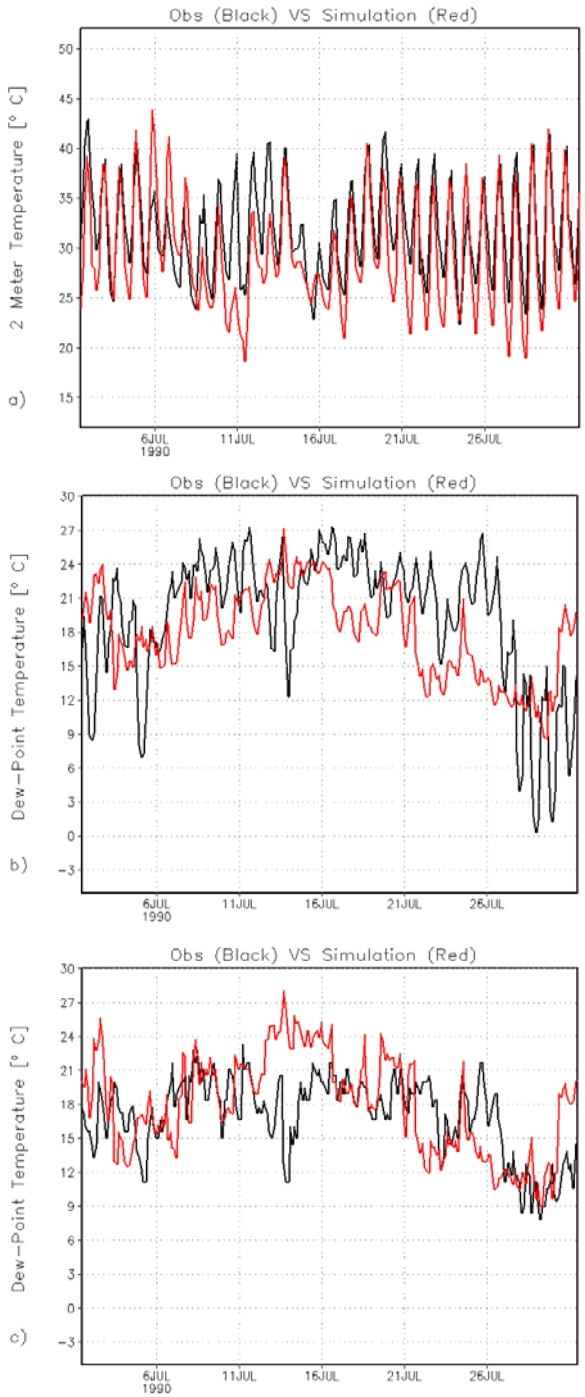

Figure 5.1 (a) Observed (**black**) three-hourly air temperatures and RAMS simulated (**red**) air temperatures from the control run experiment during the period July 1st -12Z to July 31st -12Z, 1990 - the time series represent observations averaged over all AZMET stations and KPHX; **(b)** as (a) but for observed (**black**) and RAMS simulated (**red**) three-hourly dew point averaged only over the AZMET stations; **(c)** as (b) but for observed (**black**) and RAMS simulated (**red**) three-hourly dew point averaged only for KPHX.

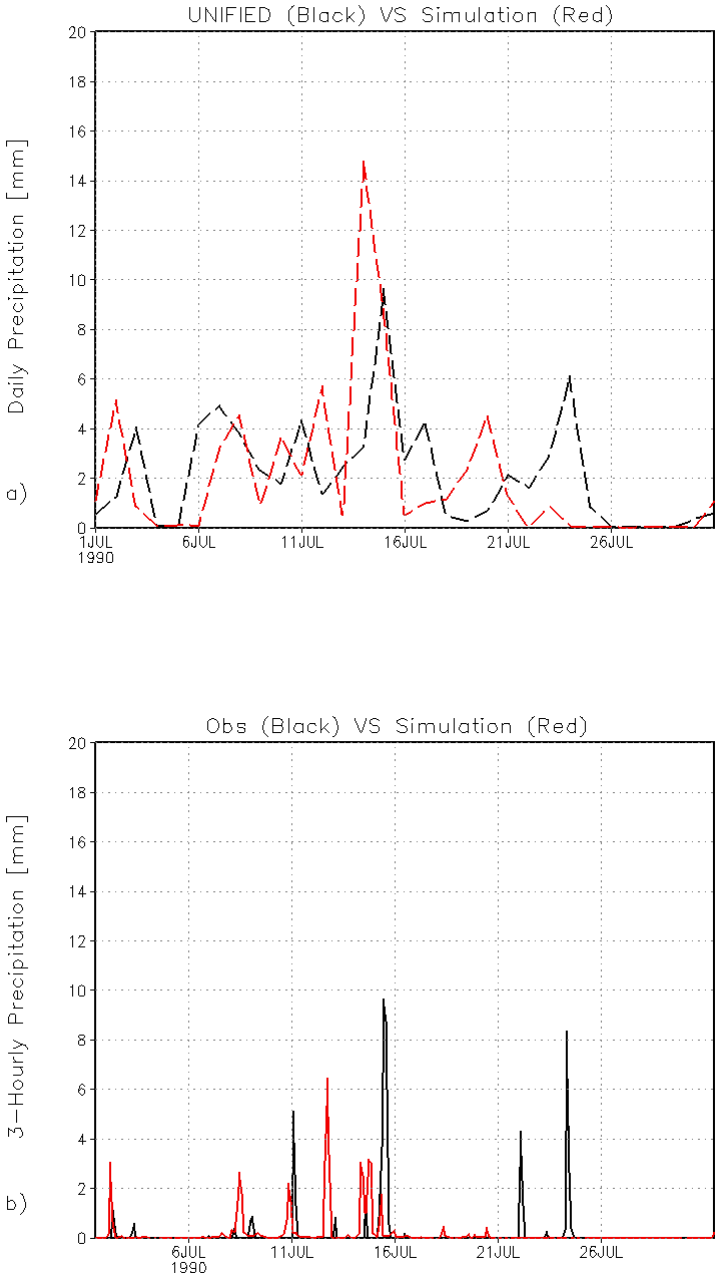

Figure 5.2 (a) UNIFIED dataset daily precipitation accumulation (**black**) and RAMS simulated daily precipitation accumulation (**red**) averaged over the entirety of Grid 3. All units are in [mm]; **(b)** AZMET stations and KPHX (**black**) observed three-hourly precipitation accumulation and RAMS simulated (**red**) three-hourly precipitation accumulation from the control run experiment during the period July 1st - July 31st 1990.

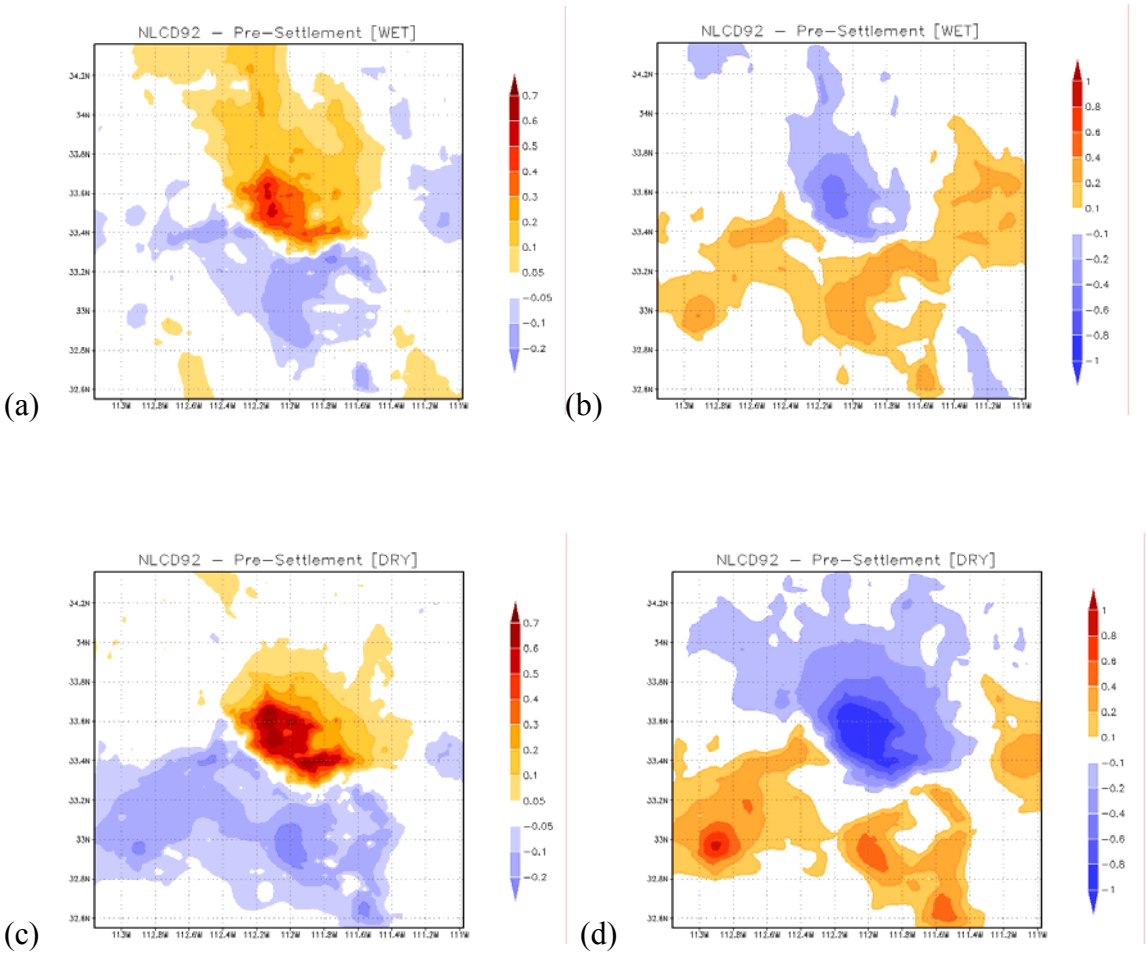

Figure 6.1 RAMS simulated ensemble differences (NLCD92 - Pre-Settlement) in **(a)** first atmospheric level [24.1 m] air temperature [°C] and **(b)** dew point [°C], for the WET years; **(c)** first atmospheric level [24.1 m] air temperature [°C] and **(d)** dew point [°C], for the DRY years. Each calculation is for the analysis period: July 1, 12Z – July 31, 12Z.

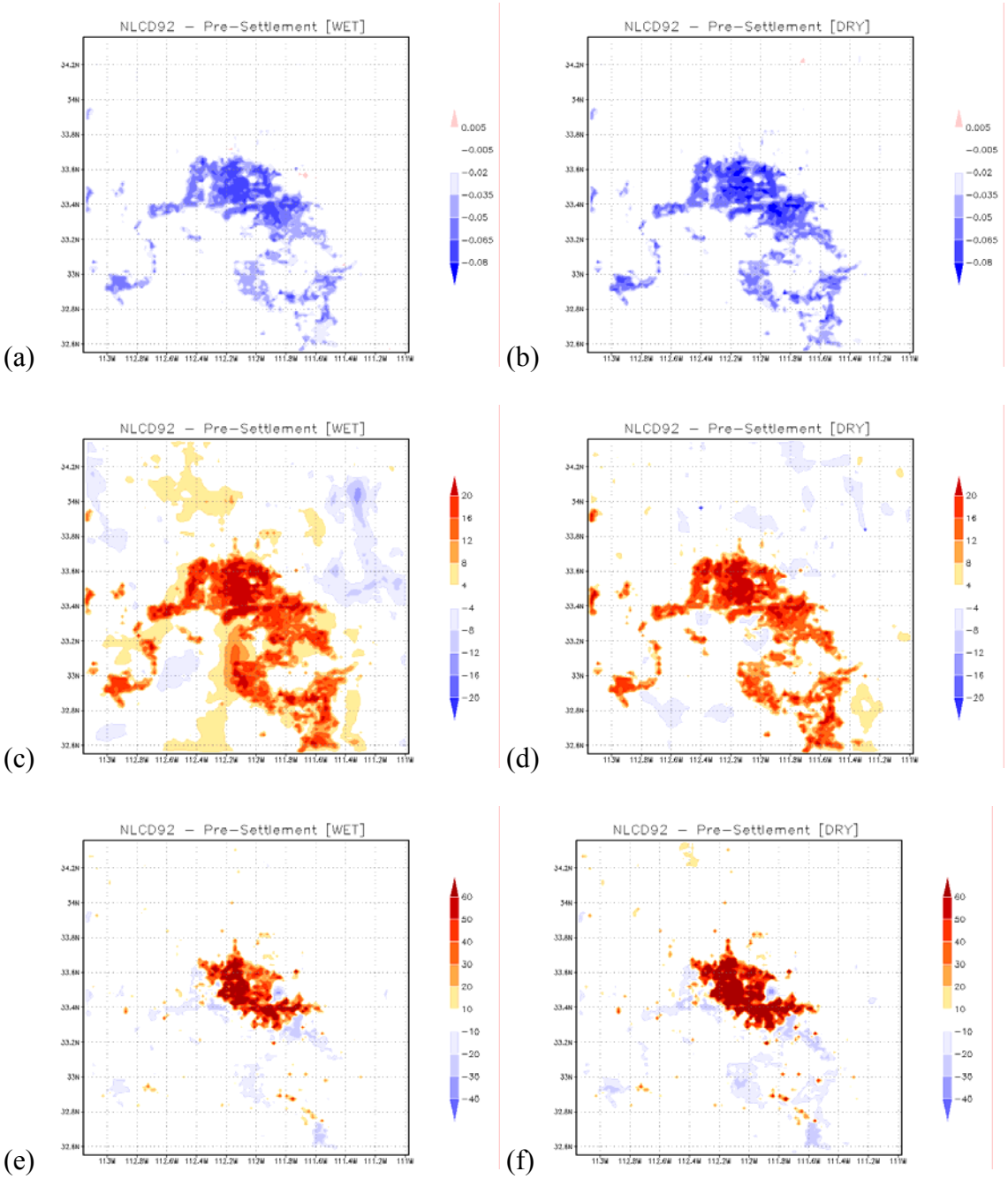

Figure 6.2 RAMS simulated ensemble differences (NLCD92 - Pre-Settlement) in surface albedo for the **(a)** WET years and **(b)** DRY years; as (a) but for **(c)** incident radiation [W m^{-2}] for the WET years and **(d)** as (b) but for incident radiation [W m^{-2}], for the DRY years; as (a) but for **(e)** surface sensible heat flux [W m^{-2}] for the WET years and **(f)** as (b) but for surface sensible heat flux [W m^{-2}] for the DRY years. Each calculation is for the analysis period: July 1, 12Z – July 31, 12Z.

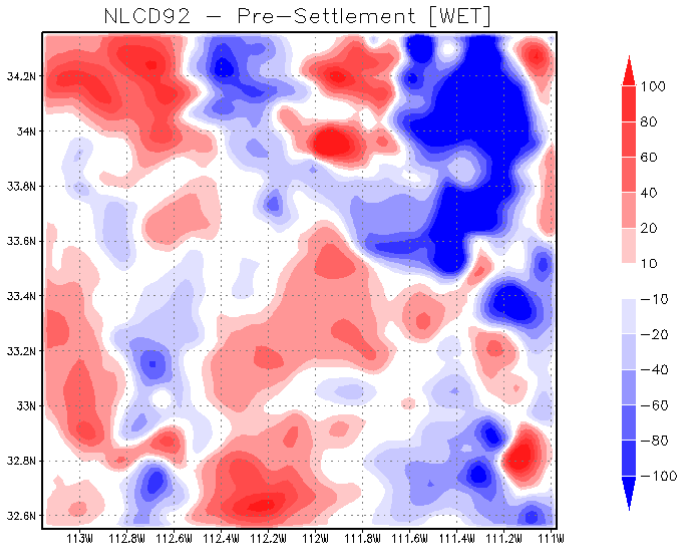

(a)

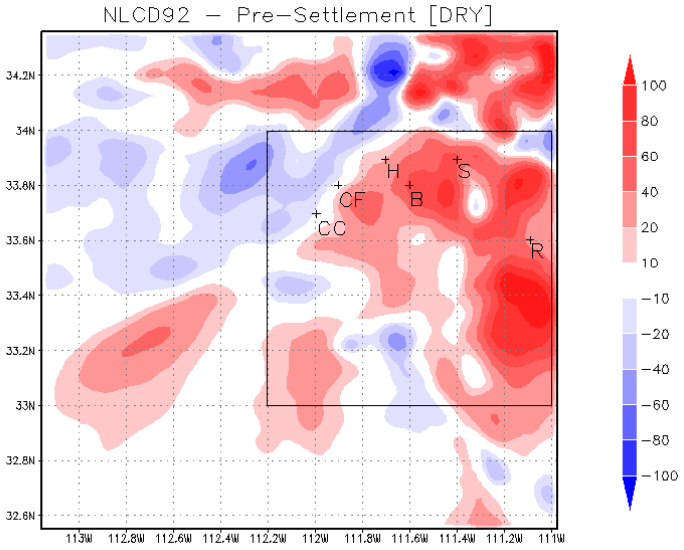

(b)

Figure 6.3 RAMS simulated ensemble differences (NLCD92 - Pre-Settlement) in **(a)** total accumulated precipitation [mm] for all 3 WET years; **(b)** total accumulated precipitation [mm] for all 3 DRY years. The + labels correspond to the station locations analyzed in Shepherd et al. (2006), and each adjacent letter corresponds to the station name: CF – Carefree; CC – Cave Creek; H - Horseshoe Dam; B – Bartlett Dam; S – Sunflower; R: Roosevelt Dam.

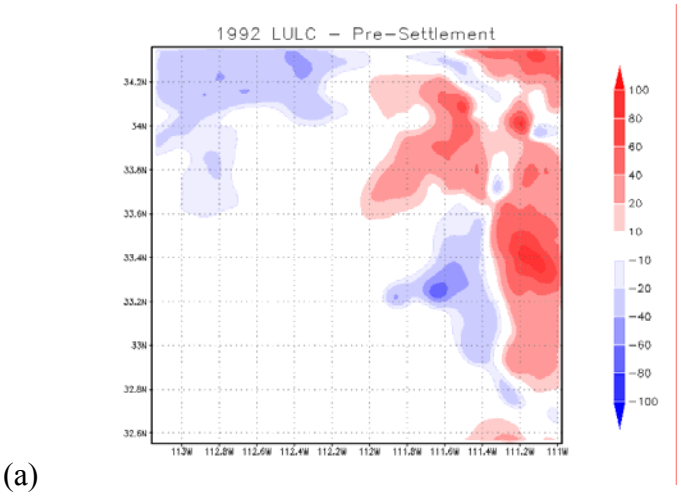

(a)

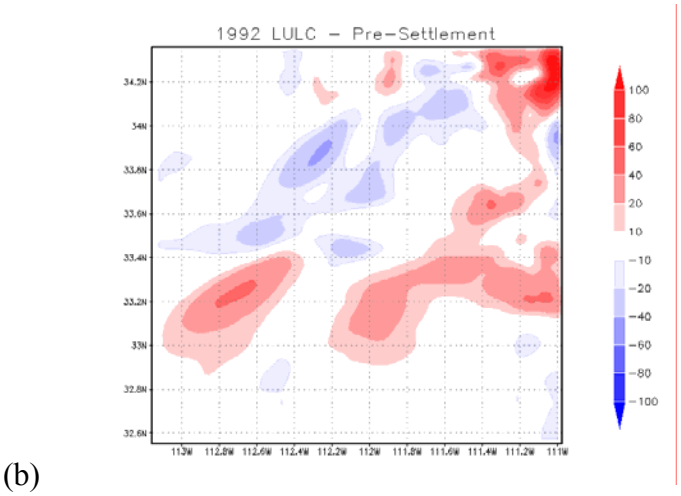

(b)

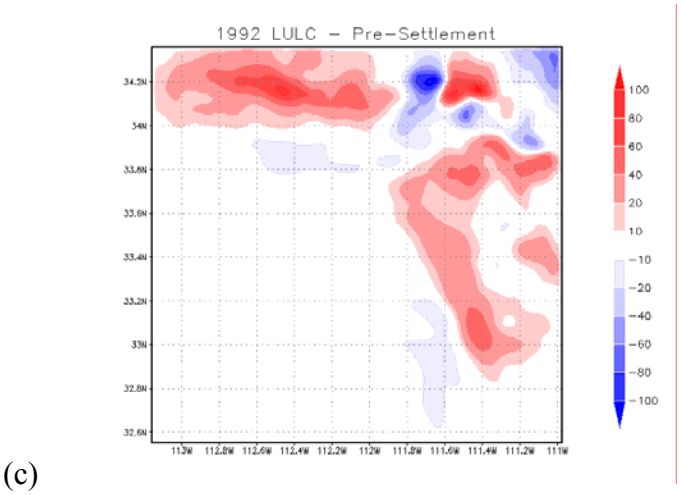

(c)

Figure 6.4 RAMS simulated accumulated precipitation [mm] difference (NLCD92 - Pre-Settlement) for each DRY year: **(a)** 1979 **(b)** 1989, and **(c)** 1994.

(a)

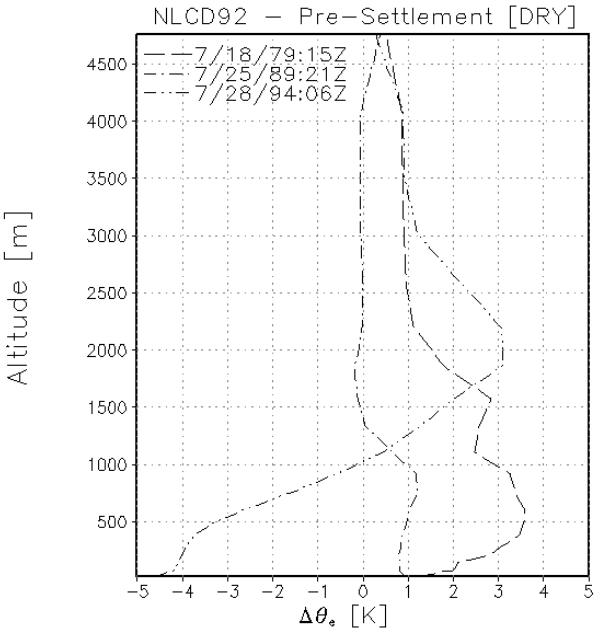

(b)

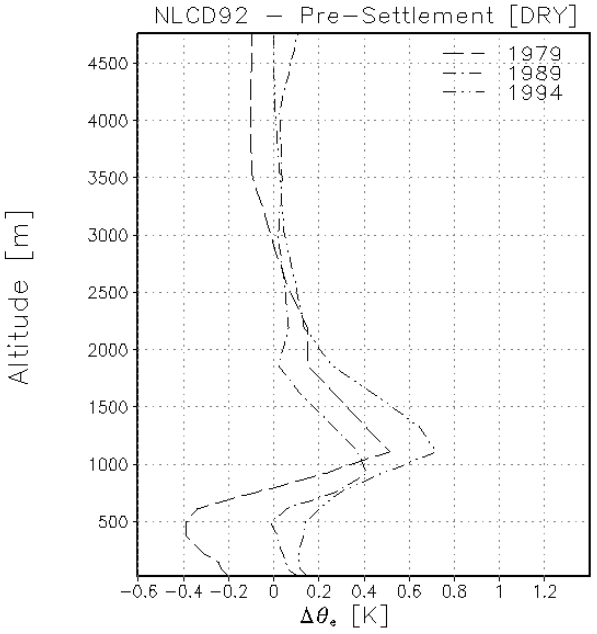

Figure 6.5 RAMS simulated domain-averaged [lat: 33 to 34/lon: -112.2 to -111.0] vertical profile of equivalent potential temperature difference (NLCD92 - Pre-Settlement) for selected DRY year cases **(a)**; **(b)** as (a), but averaged over each DRY year simulation, at 17 LST, for the month of July. See Figure 6.3 [b] for extent of averaging domain.

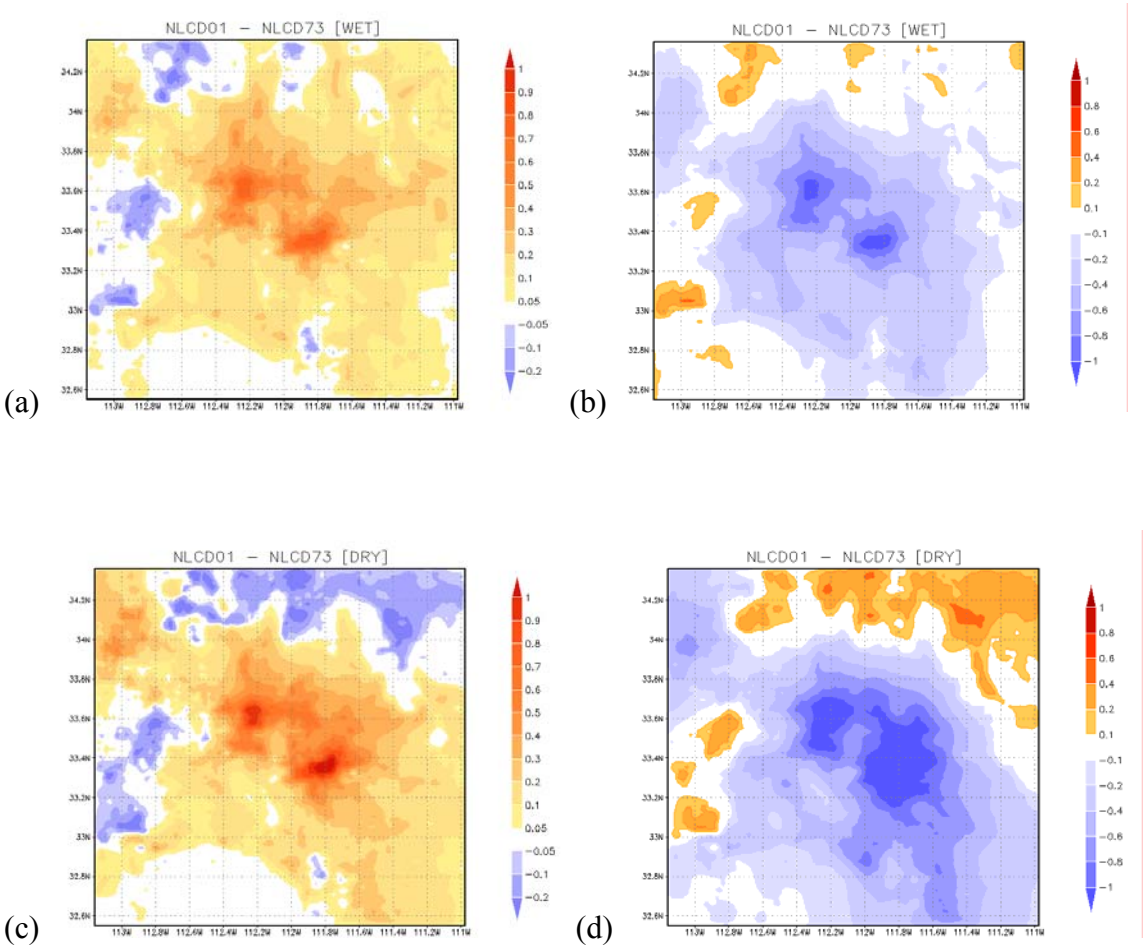

Figure 7.1 RAMS simulated ensemble differences (NLCD01 minus NLCD73) in **(a)** first atmospheric level [24.1 m] air temperature [°C] and **(b)** dew point [°C], for all three *WET* years; **(c)** first atmospheric level [24.1 m] air temperature [°C] and **(d)** dew point [°C], for all three *DRY* years.

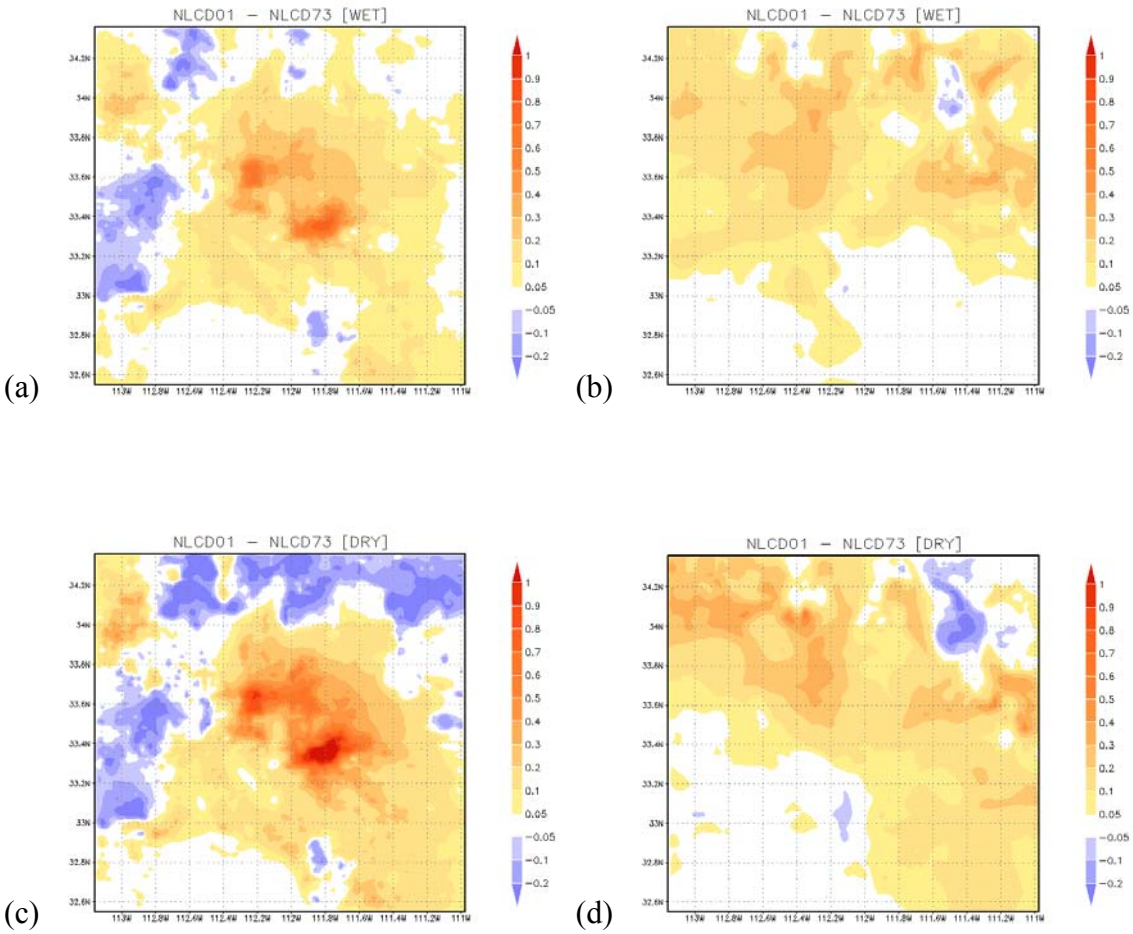

Figure 7.2 RAMS simulated ensemble differences (NLCD01 minus NLCD73) in **(a)** first atmospheric level [24.1 m] daily maximum air temperature [°C] and **(b)** daily minimum air temperature [°C], for all three *WET* years; **(c)** as (a), but for all three *DRY* years, and **(d)** as (b) but for all three *DRY* years.

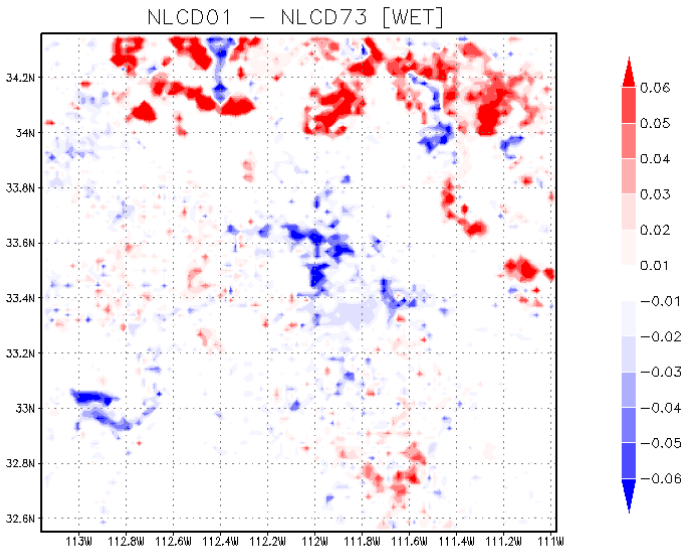

(a)

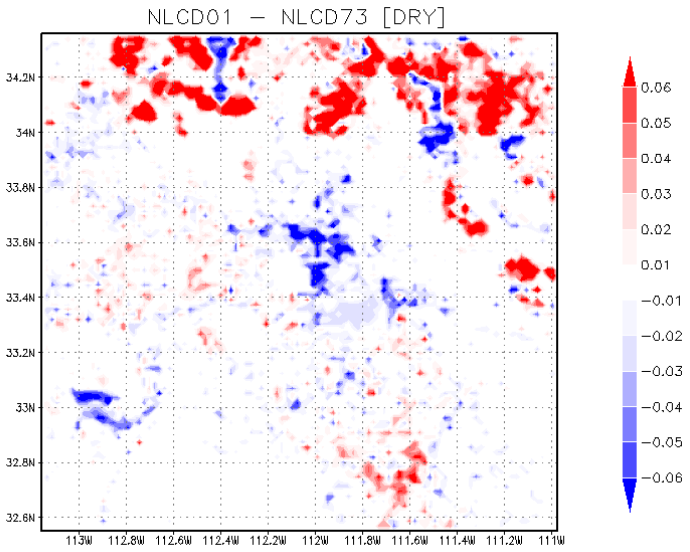

(b)

Figure 7.3 RAMS simulated ensemble differences (NLCD01 – NLCD73) in surface albedo for the **(a)** WET years and **(b)** DRY years.

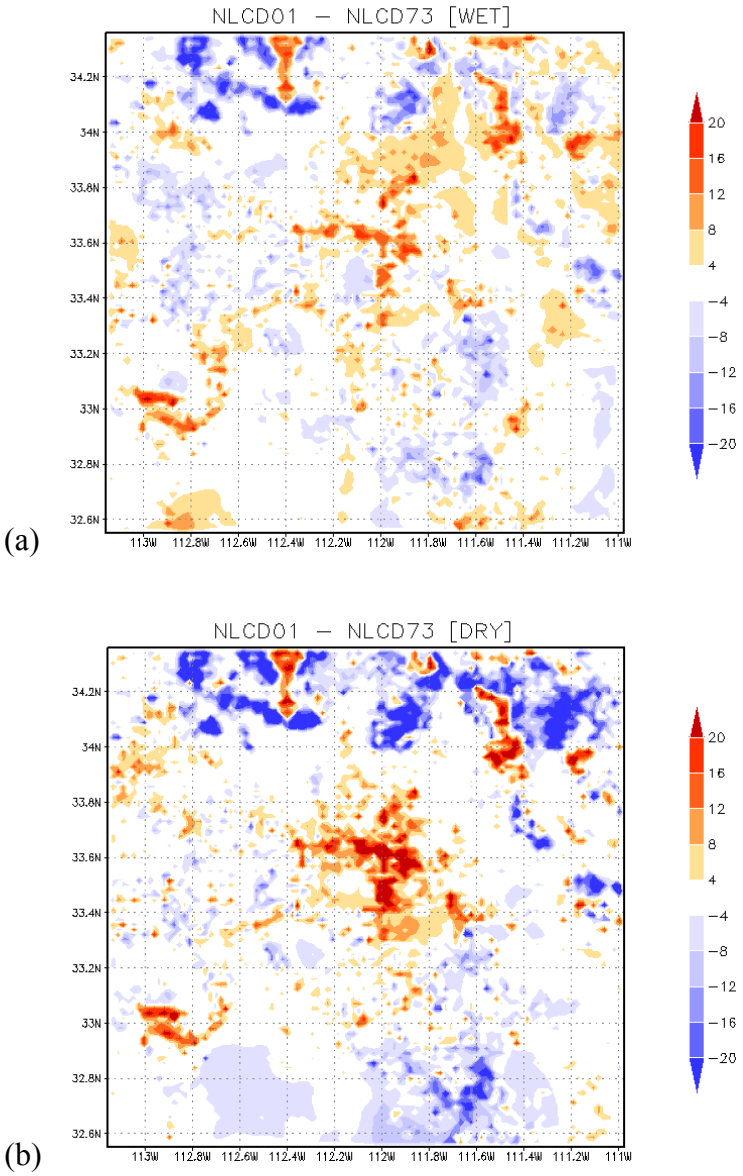

Figure 7.4 RAMS simulated ensemble differences (NLCD01 – NLCD73) in incident radiation [W m^{-2}] for the **(a)** WET years and **(b)** DRY years.

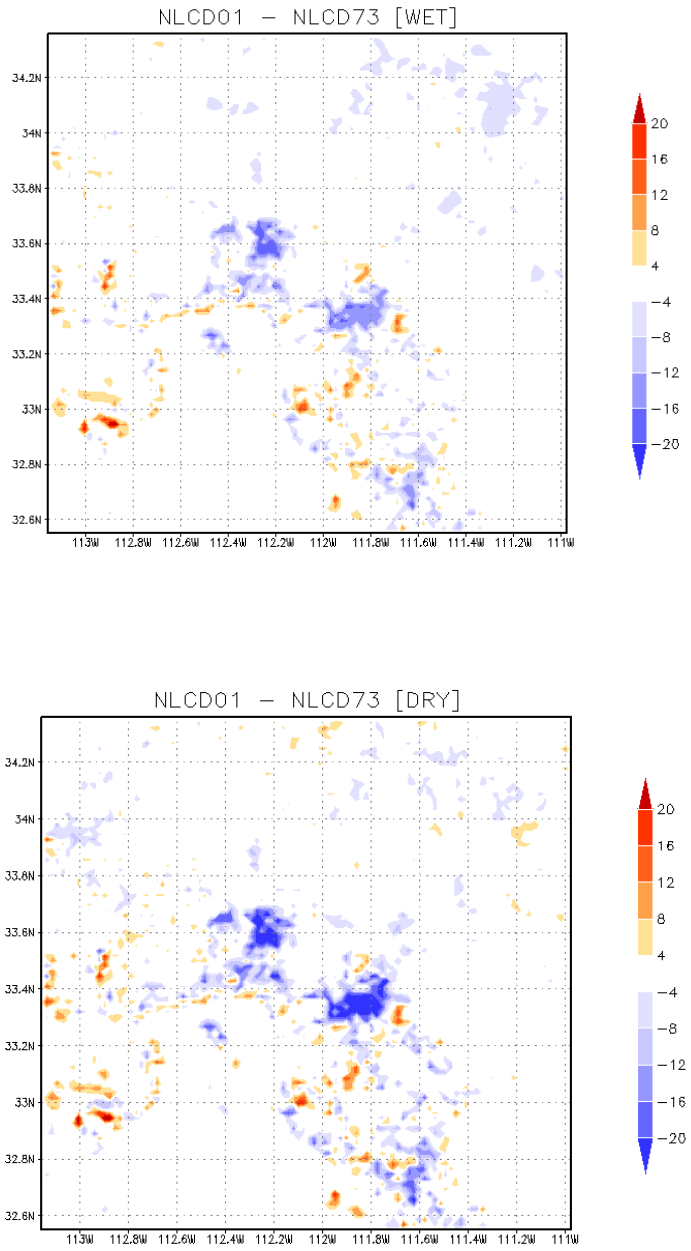

Figure 7.5 RAMS simulated ensemble differences (NLCD01 – NLCD73) in net longwave flux [W m^{-2}] for the **(a)** WET years and **(b)** DRY years.

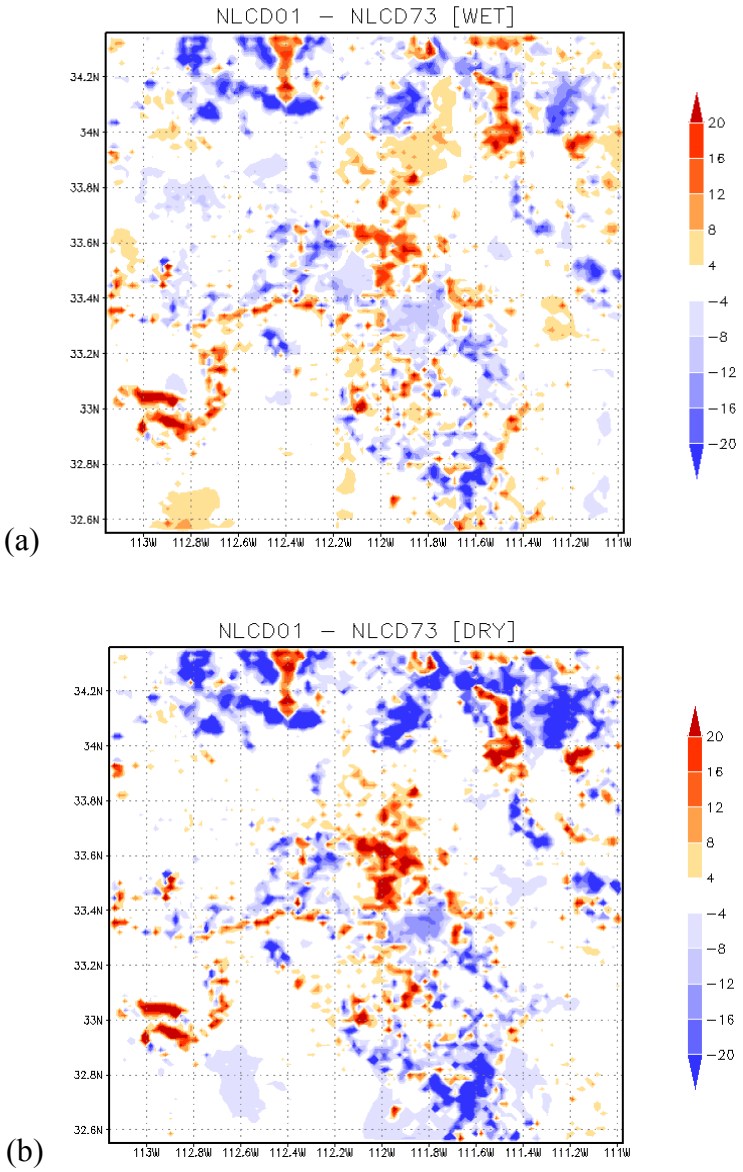

Figure 7.6 RAMS simulated ensemble differences (NLCD01 – NLCD73) in total net radiative flux [W m^{-2}] for the **(a)** WET years and **(b)** DRY years.

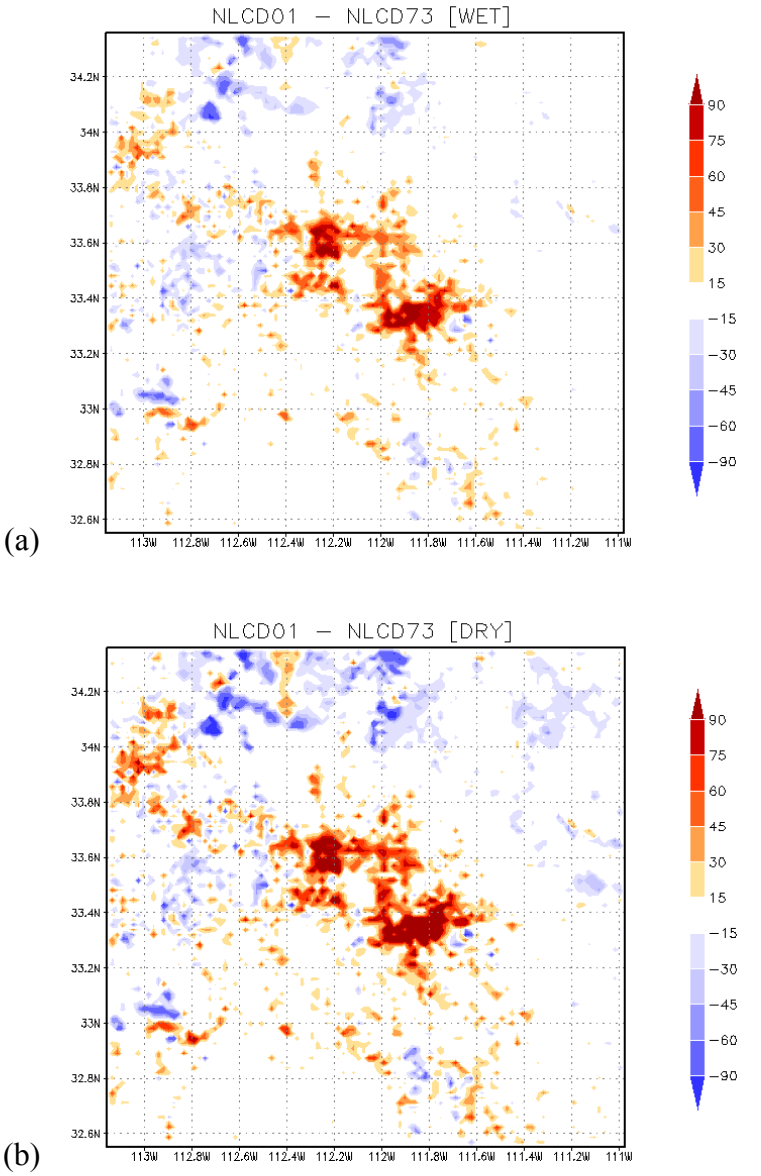

Figure 7.7 RAMS simulated ensemble differences (NLCD01 – NLCD73) in surface sensible heat flux [W m^{-2}] for the **(a)** WET years and **(b)** DRY years.

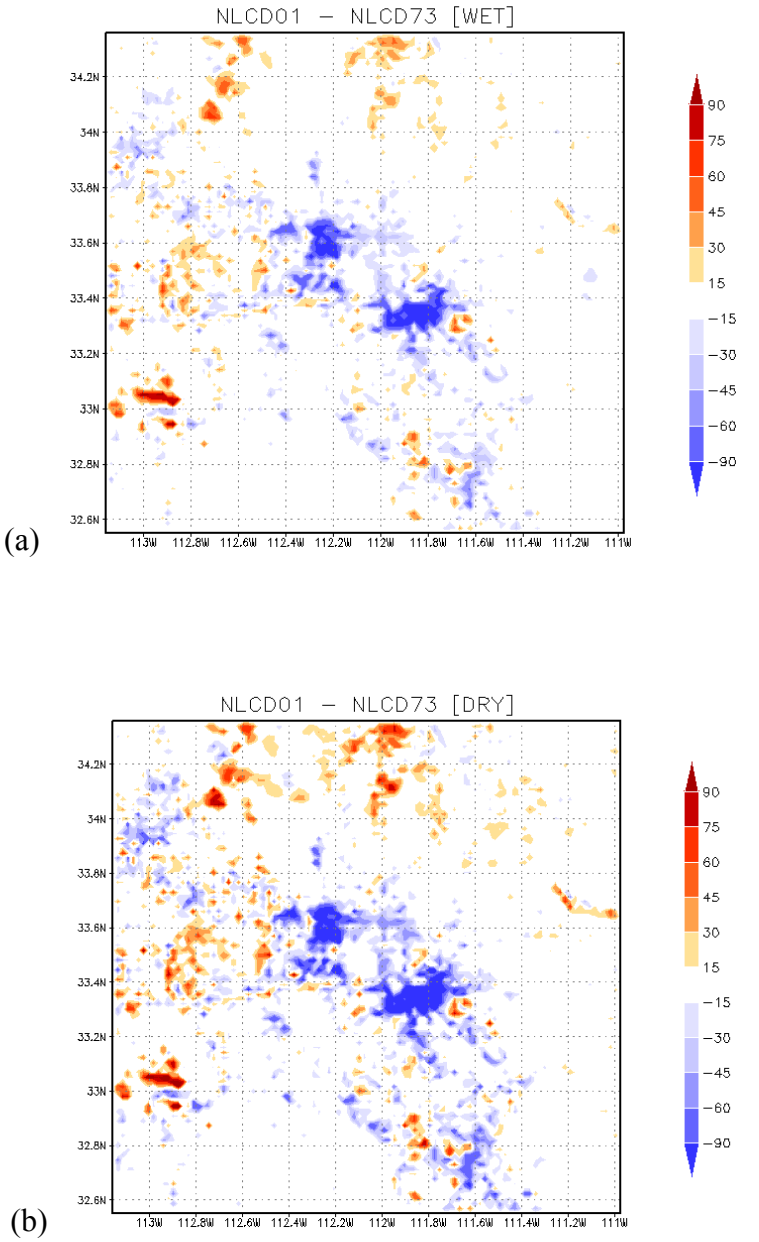

Figure 7.8 RAMS simulated ensemble differences (NLCD01 – NLCD73) in surface latent heat flux [W m^{-2}] for the **(a)** WET years and **(b)** DRY years.

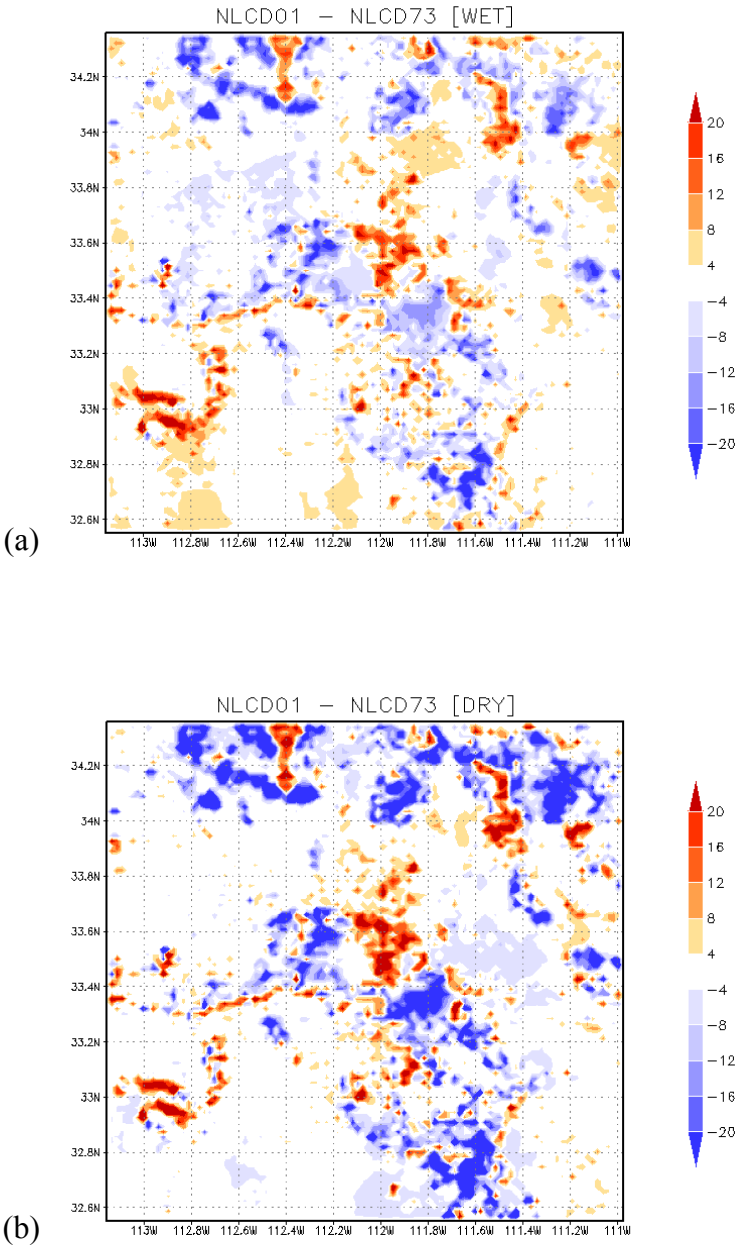

Figure 7.9 RAMS simulated ensemble differences (NLCD01 – NLCD73) in net surface heat flux [W m^{-2}] for the **(a)** WET years and **(b)** DRY years.

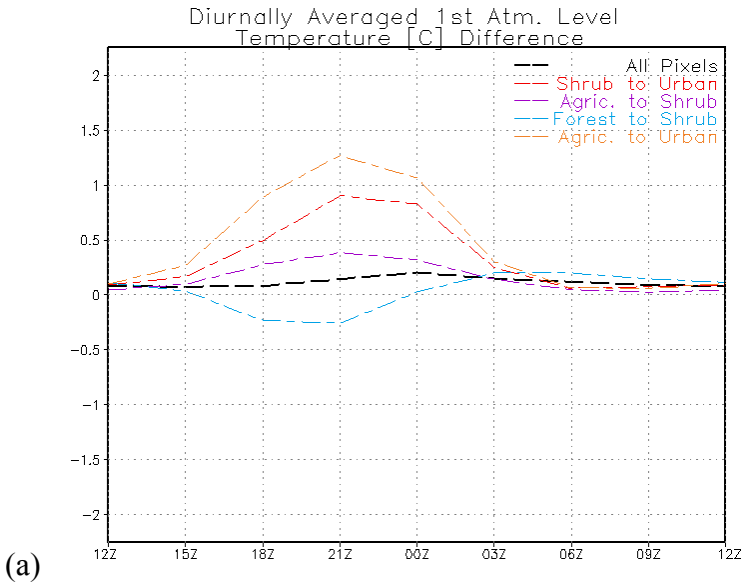

(a)

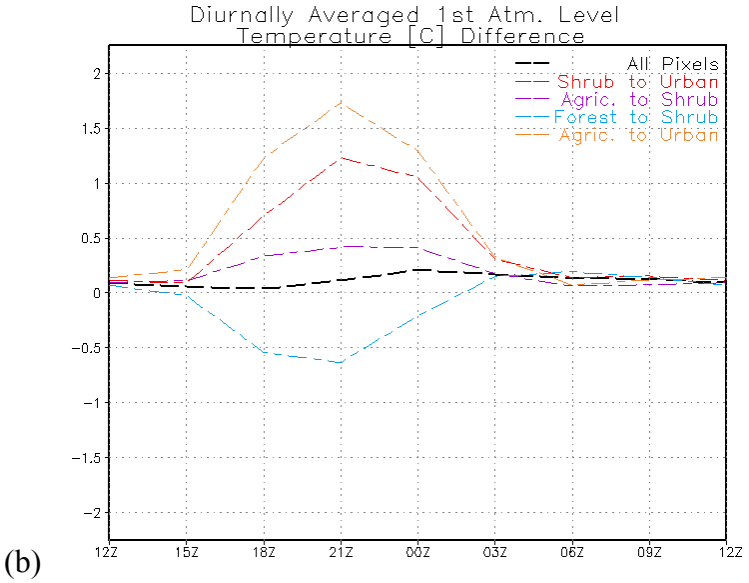

(b)

Figure 7.10 RAMS simulated time series of diurnally-averaged first atmospheric level [24.1 m] temperature differences [°C] (NLCD01 minus NLCD73) for those grid cells that experienced the following shift in dominant land cover type (from NLCD73 to NLCD01): from shrub to urban (red), from irrigated agriculture to shrub (purple), from evergreen needle-leaf to shrub (blue), from irrigated agriculture to urban (orange), and all land points on Grid 3 (black), for all three **(a)** WET years, and for **(b)** all three DRY years.

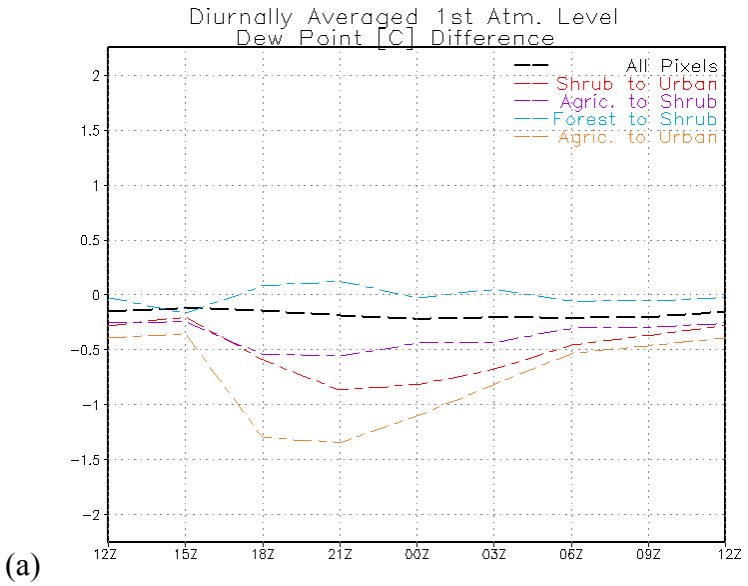

(a)

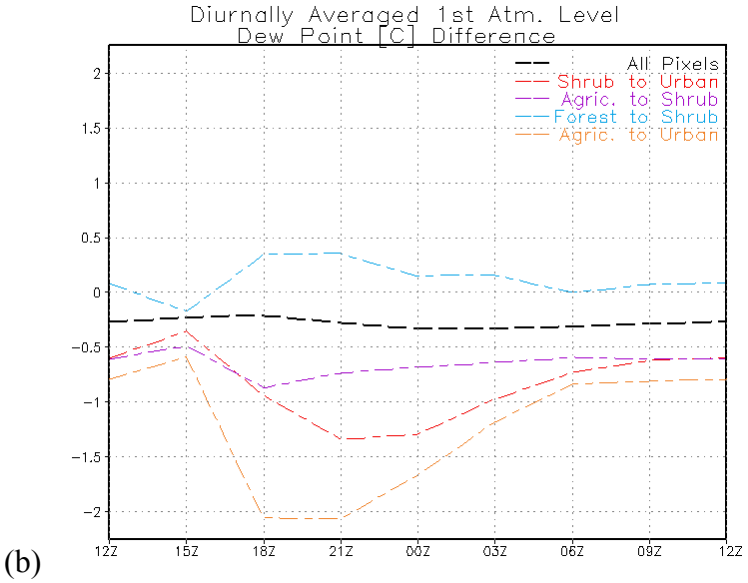

(b)

Figure 7.11 RAMS simulated time series of diurnally-averaged first atmospheric level [24.1 m] dew-point temperature differences [°C] (NLCD01 minus NLCD73) for those grid cells that experienced the following shift in dominant land cover type (from NLCD73 to NLCD01): from shrub to urban (red), from irrigated agriculture to shrub (purple), from evergreen needle-leaf to shrub (blue), from irrigated agriculture to urban (orange), and all land points on Grid 3 (black), for all three **(a)** WET years, and for **(b)** all three DRY years.

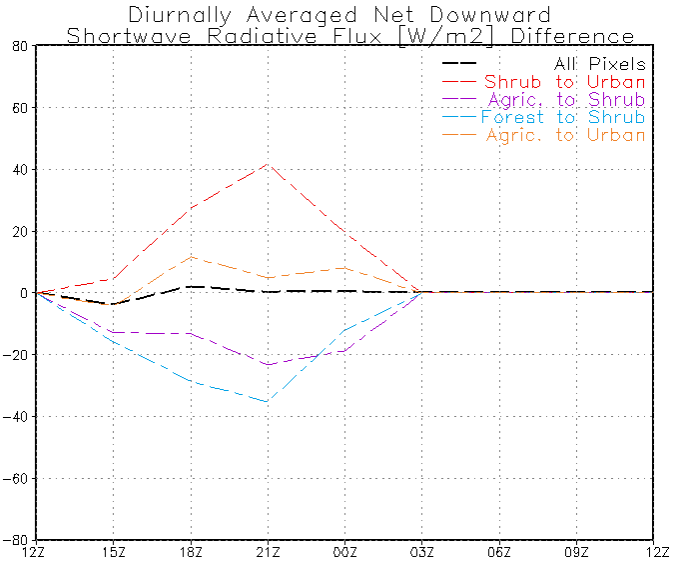

(a)

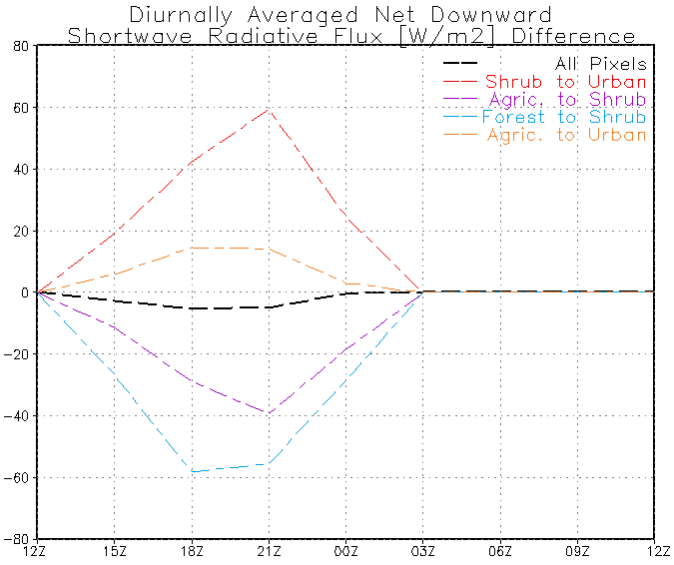

(b)

Figure 7.12 RAMS simulated time series of diurnally-averaged net surface shortwave radiative flux [W m^{-2}] (NLCD01 minus NLCD73) for those grid cells that experienced the following shift in dominant land cover type (from NLCD73 to NLCD01): from shrub to urban (red), from irrigated agriculture to shrub (purple), from evergreen needle-leaf to shrub (blue), from irrigated agriculture to urban (orange), and all land points on Grid 3 (black), for all three **(a)** WET years, and for **(b)** all three DRY years.

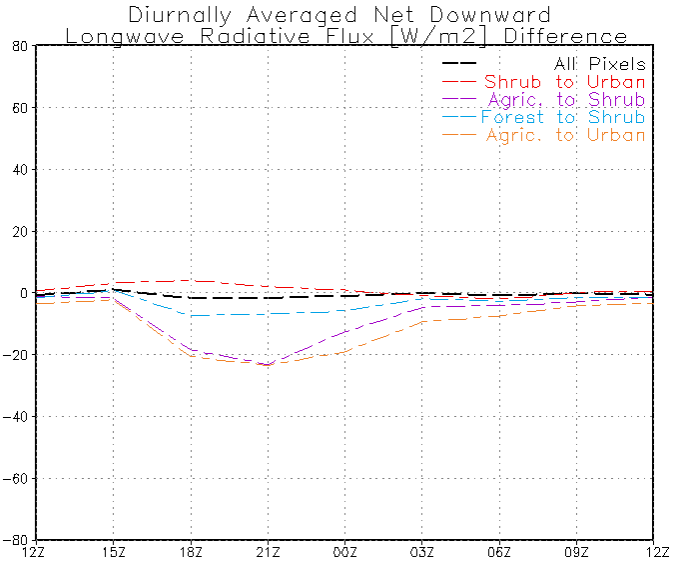

(a)

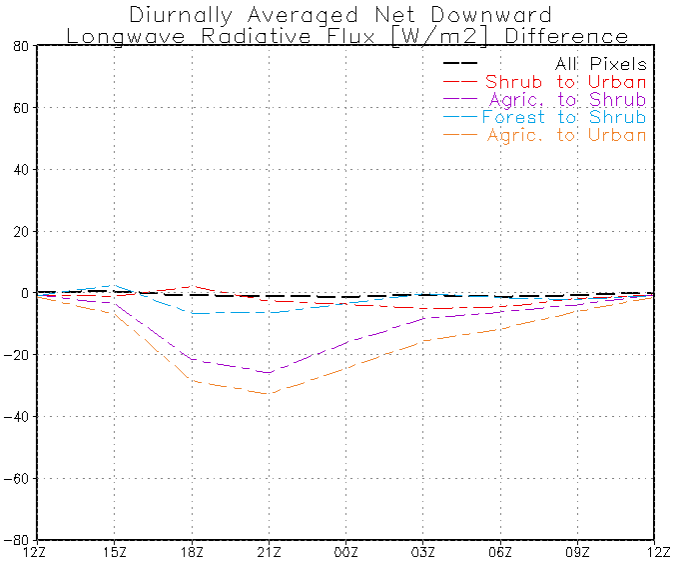

(b)

Figure 7.13 RAMS simulated time series of diurnally-averaged net longwave radiative flux [W m^{-2}] (NLCD01 minus NLCD73) for those grid cells that experienced the following shift in dominant land cover type (from NLCD73 to NLCD01): from shrub to urban (red), from irrigated agriculture to shrub (purple), from evergreen needle-leaf to shrub (blue), from irrigated agriculture to urban (orange), and all land points on Grid 3 (black), for all three **(a)** WET years, and for **(b)** all three DRY years.

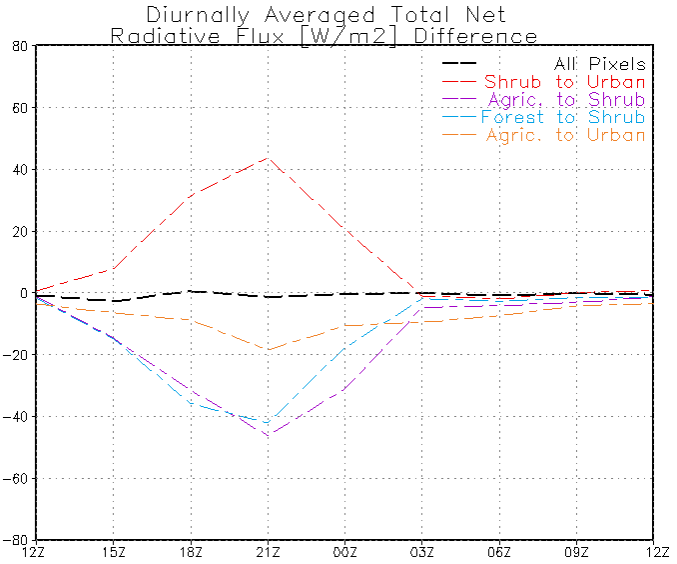

(a)

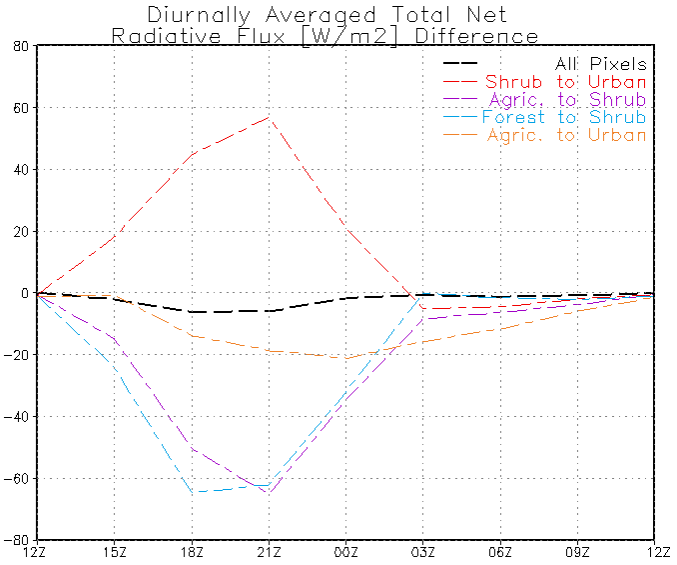

(b)

Figure 7.14 RAMS simulated time series of diurnally-averaged total net radiative flux [W m^{-2}] (NLCD01 minus NLCD73) for those grid cells that experienced the following shift in dominant land cover type (from NLCD73 to NLCD01): from shrub to urban (red), from irrigated agriculture to shrub (purple), from evergreen needle-leaf to shrub (blue), from irrigated agriculture to urban (orange), and all land points on Grid 3 (black), for all three **(a)** WET years, and for **(b)** all three DRY years.

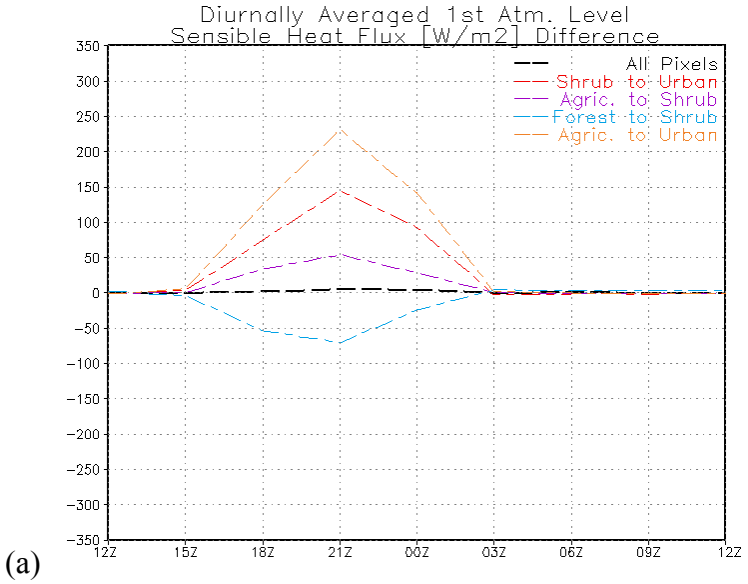

(a)

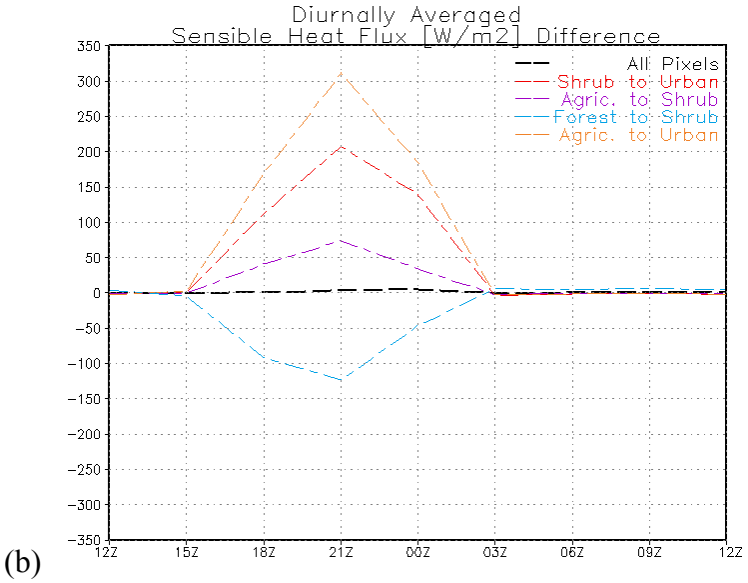

(b)

Figure 7.15 RAMS simulated time series of diurnally-averaged surface sensible heat flux [W m^{-2}] (NLCD01 minus NLCD73) for those grid cells that experienced the following shift in dominant land cover type (from NLCD73 to NLCD01): from shrub to urban (red), from irrigated agriculture to shrub (purple), from evergreen needle-leaf to shrub (blue), from irrigated agriculture to urban (orange), and all land points on Grid 3 (black), for all three **(a)** WET years, and for **(b)** all three DRY years.

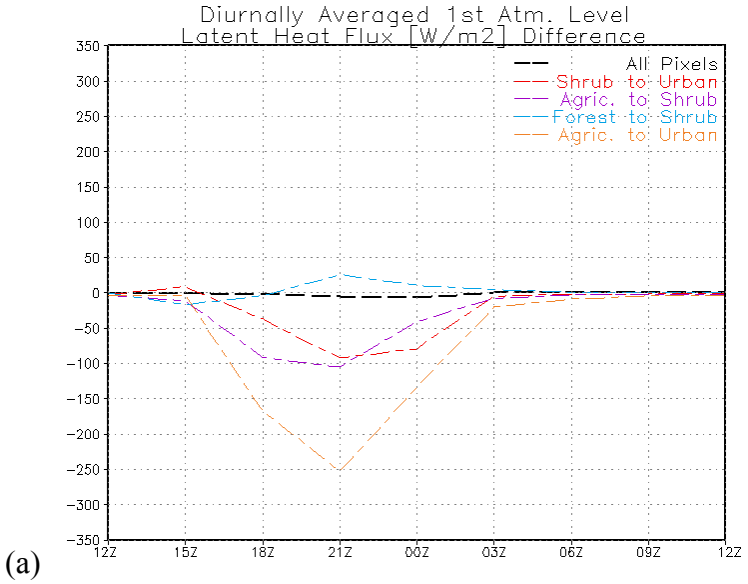

(a)

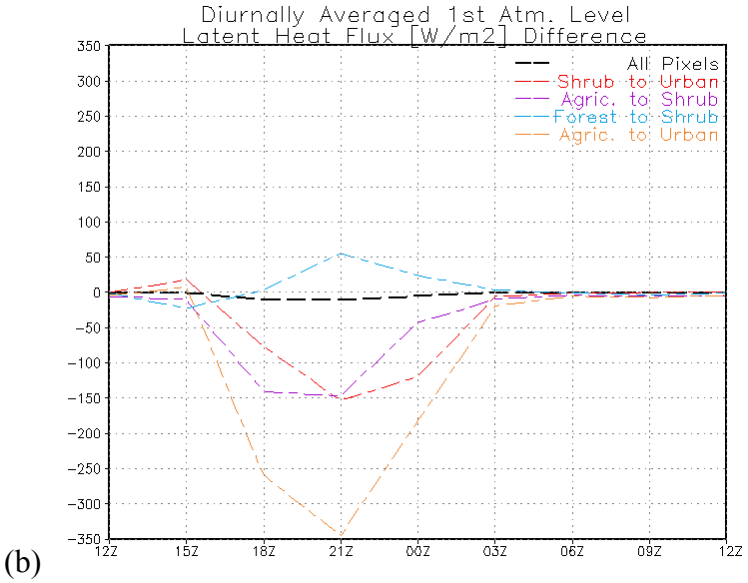

(b)

Figure 7.16 RAMS simulated time series of diurnally-averaged surface latent heat flux [W m^{-2}] (NLCD01 minus NLCD73) for those grid cells that experienced the following shift in dominant land cover type (from NLCD73 to NLCD01): from shrub to urban (red), from irrigated agriculture to shrub (purple), from evergreen needle-leaf to shrub (blue), from irrigated agriculture to urban (orange), and all land points on Grid 3 (black), for all three **(a)** WET years, and for **(b)** all three DRY years.

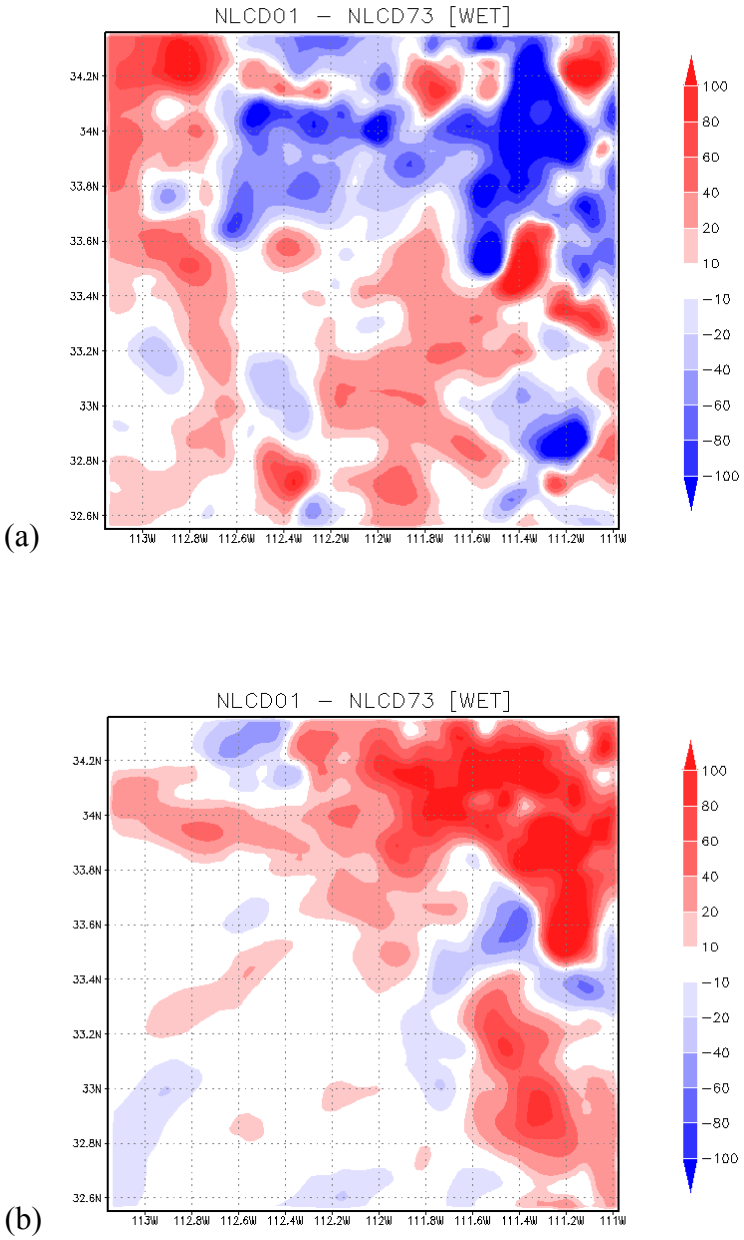

Figure 8.1 RAMS simulated ensemble differences (NLCD01 minus NLCD73) in **(a)** total accumulated precipitation [mm] for all 3 *WET* years, and **(b)** total accumulated precipitation [mm] for all 3 *DRY* years.

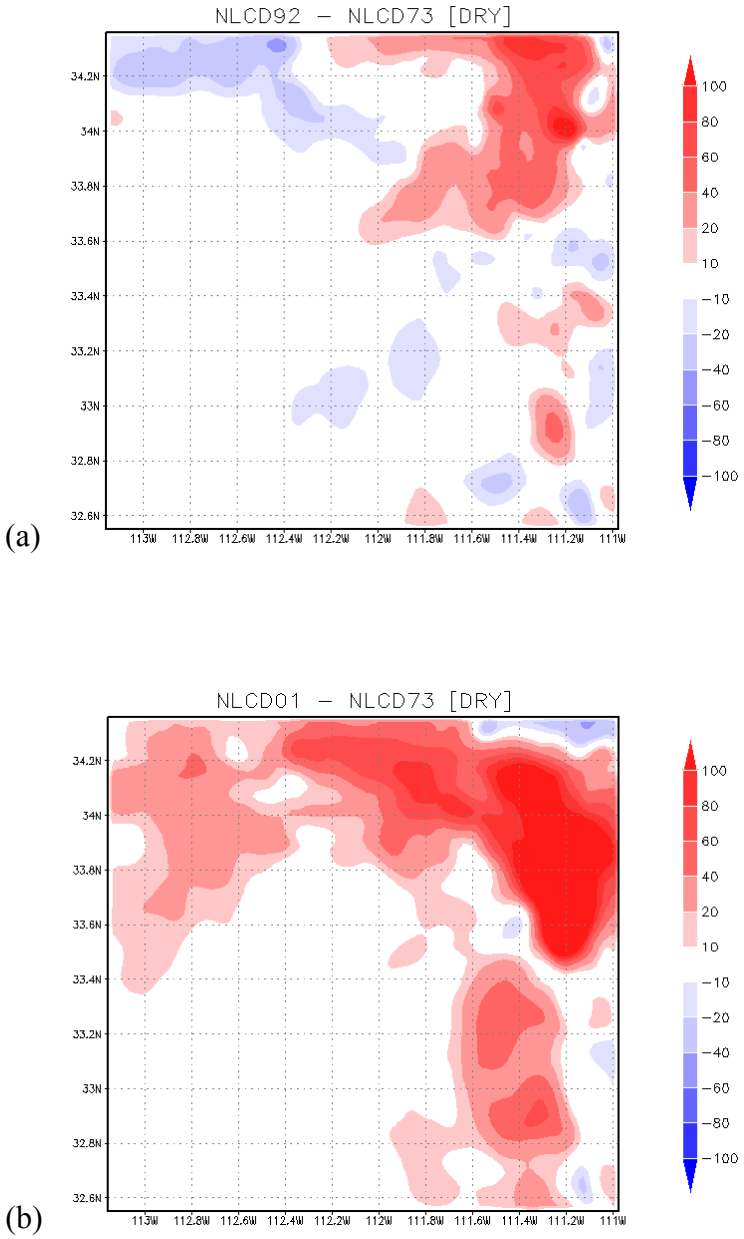

Figure 8.2 RAMS simulated accumulated precipitation [mm] difference for 1979: **(a)** NLCD92 – NLCD73 and **(b)** NLCD01 – NLCD73.

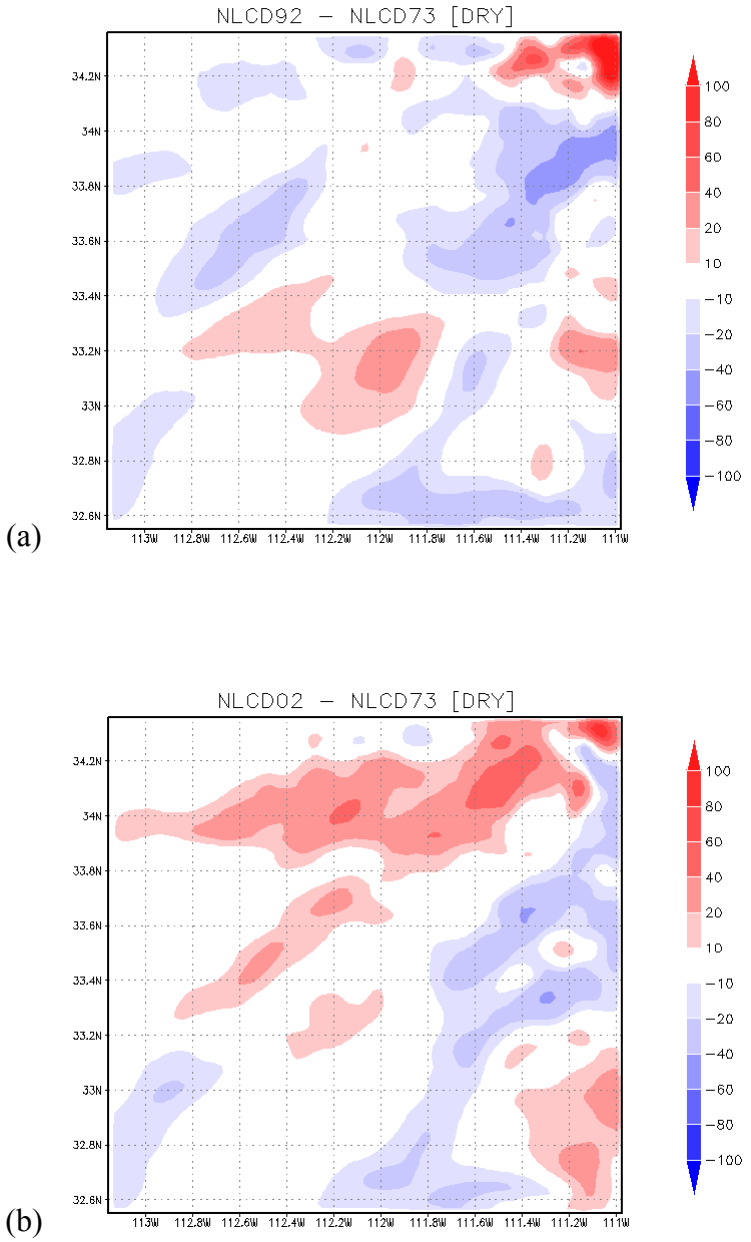

Figure 8.3 RAMS simulated accumulated precipitation [mm] difference for 1989: **(a)** NLCD92 – NLCD73 and **(b)** NLCD01 – NLCD73.

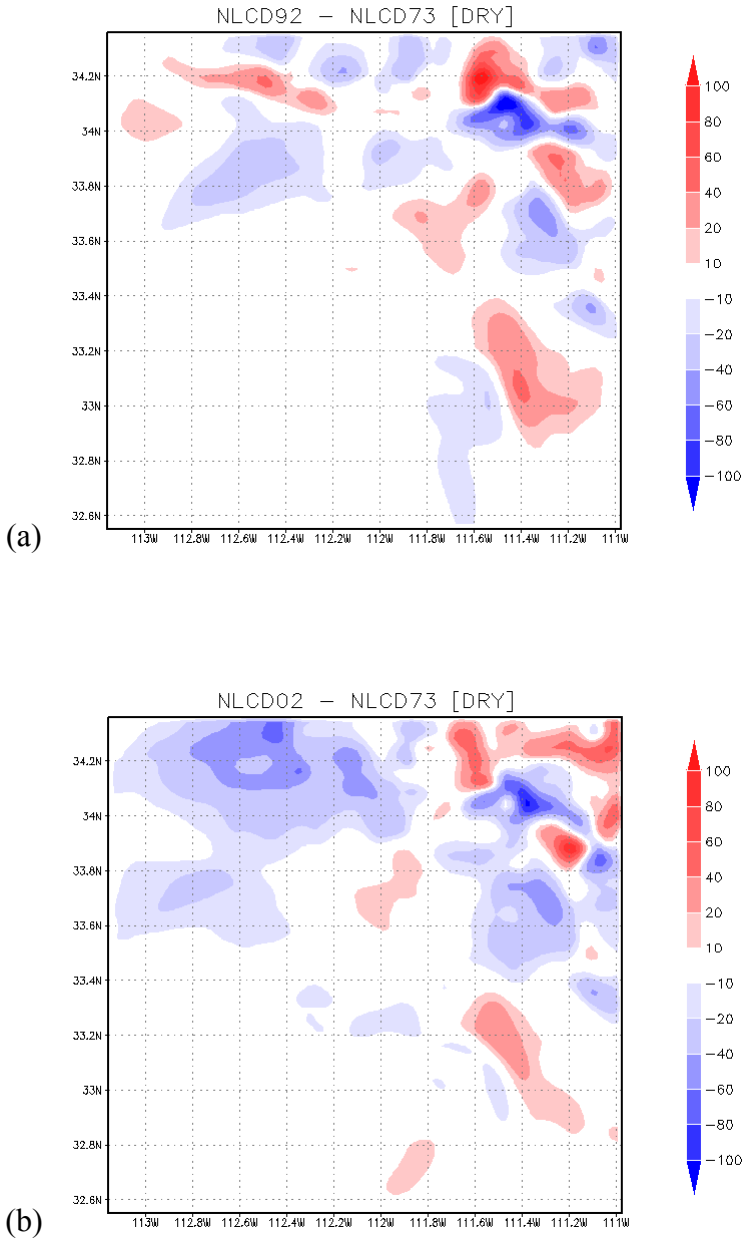

Figure 8.4 RAMS simulated accumulated precipitation [mm] difference for 1994: **(a)** NLCD92 – NLCD73 and **(b)** NLCD01 – NLCD73.

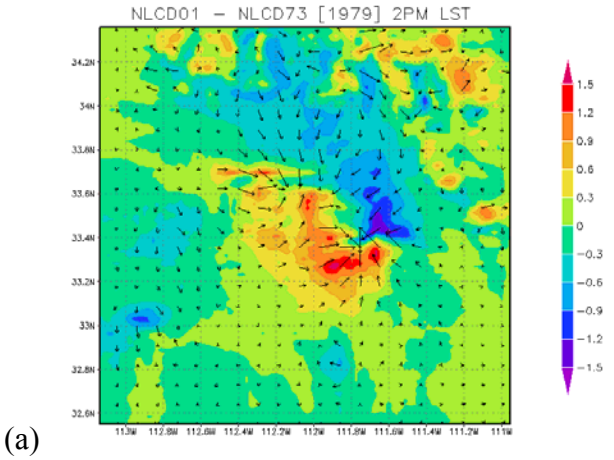

(a)

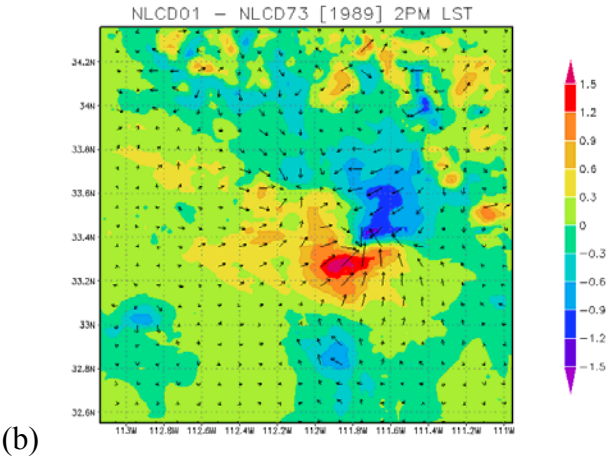

(b)

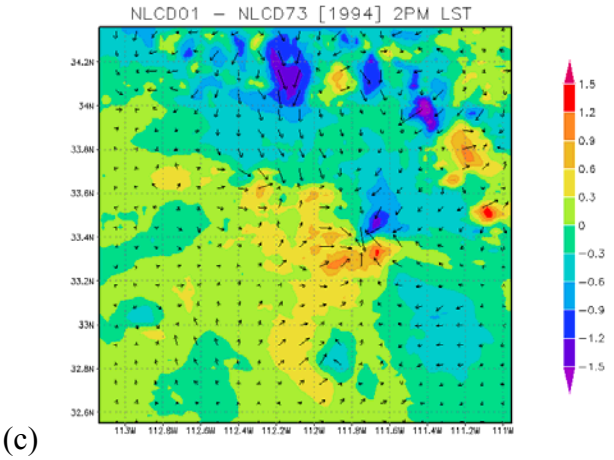

(c)

Figure 8.5 (a) RAMS simulated monthly averaged wind speed with wind vector differences overlaid (NLCD01 – NLCD73) for 1979; **(b)** as (a) but for 1989; **(c)** as (a) but for 1994. All calculations are at 14 LST.

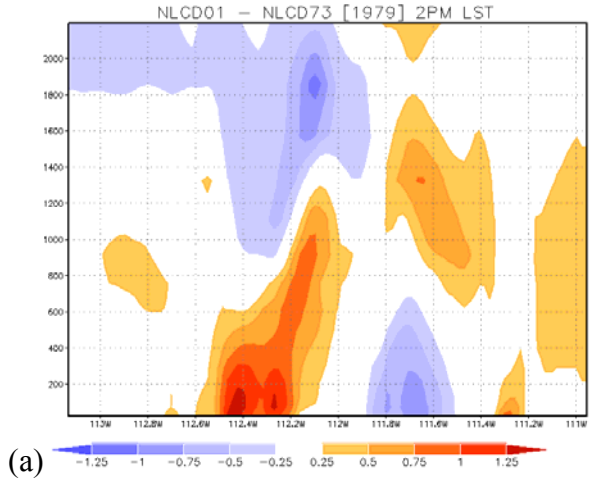

(a)

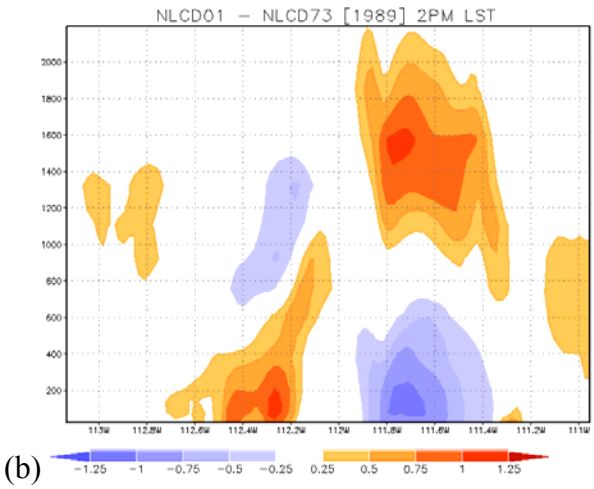

(b)

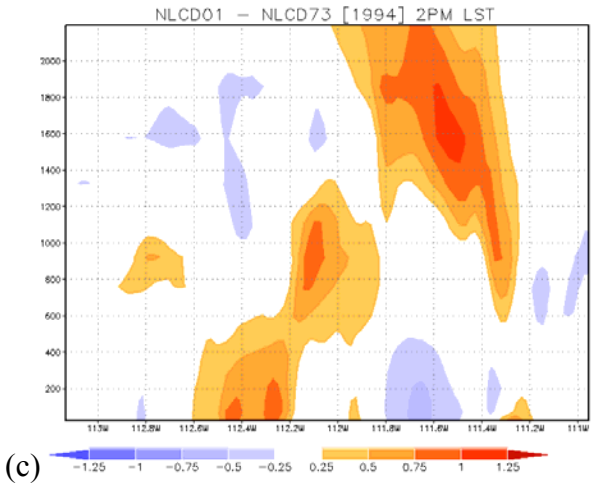

(c)

Figure 8.6 Altitude-longitude cross-section of RAMS simulated monthly averaged u-wind (m s^{-1}) speed difference (NLCD01 – NLCD73) for **(a**) 1979; **(b)** as (a) but for 1989; **(c)** as (a) but for 1994. All calculations are at 14 LST and at 33.65° N.

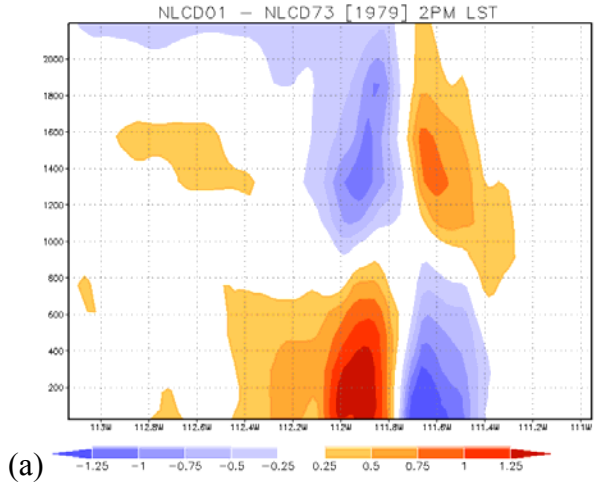

(a)

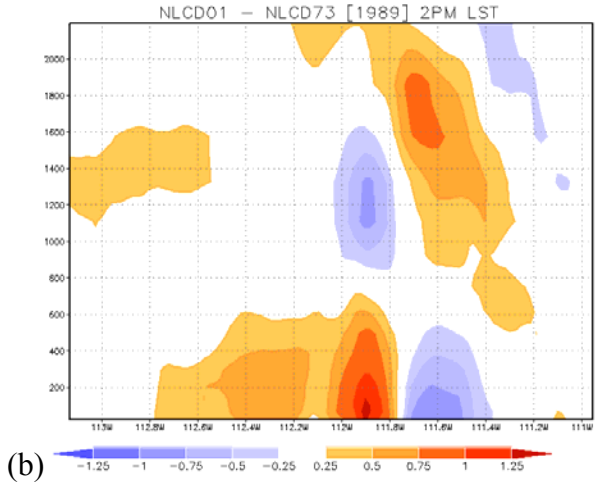

(b)

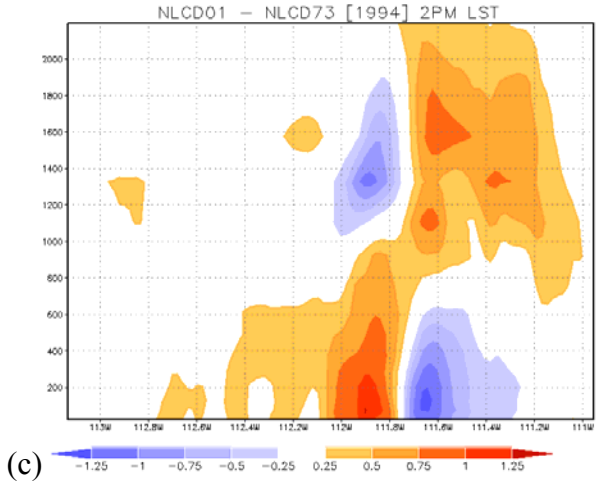

(c)

Figure 8.7 Altitude-longitude cross-section of RAMS simulated monthly averaged u-wind (m s^{-1}) speed difference (NLCD01 – NLCD73) for **(a)** 1979; **(b)** as (a) but for 1989; **(c)** as (a) but for 1994. All calculations are at 14 LST and at 33.4° N.

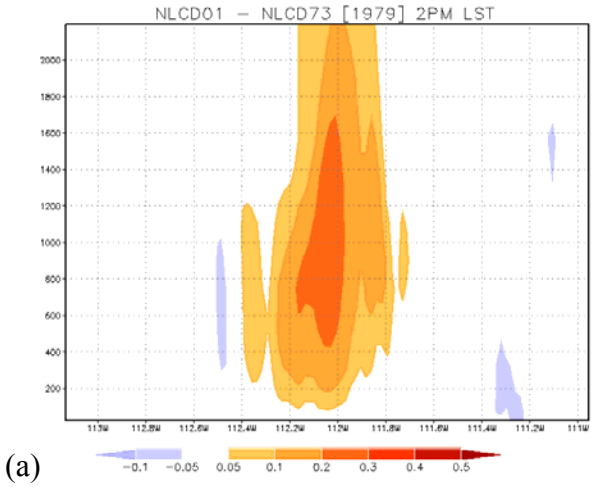

(a)

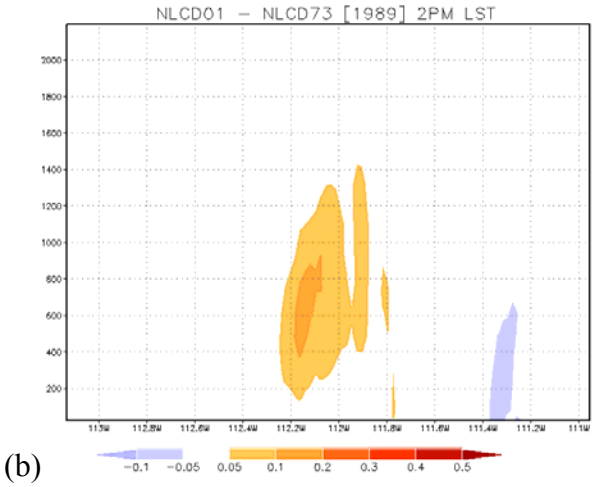

(b)

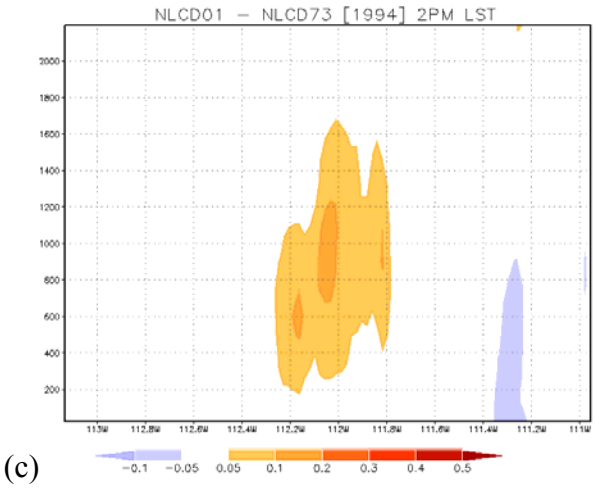

(c)

Figure 8.8 Altitude-longitude cross-section of RAMS simulated monthly averaged w-wind (m s^{-1}) speed difference (NLCD01 – NLCD73) for **(a)** 1979; **(b)** as (a) but for 1989; **(c)** as (a) but for 1994. All calculations are at 14 LST and at 33.65° N.

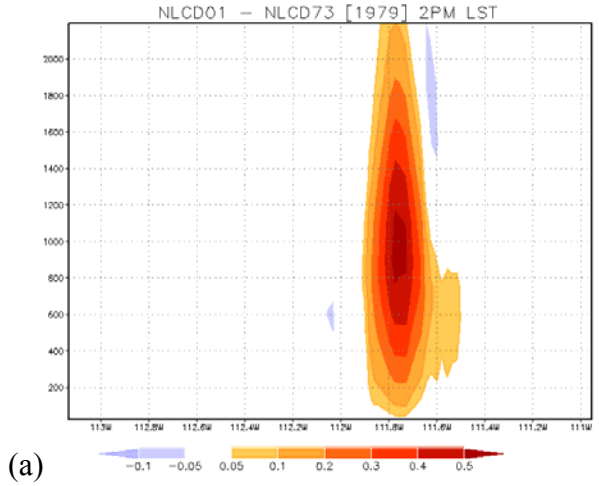

(a)

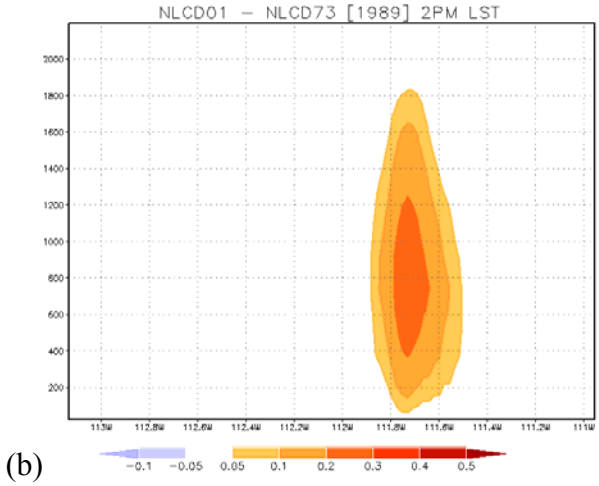

(b)

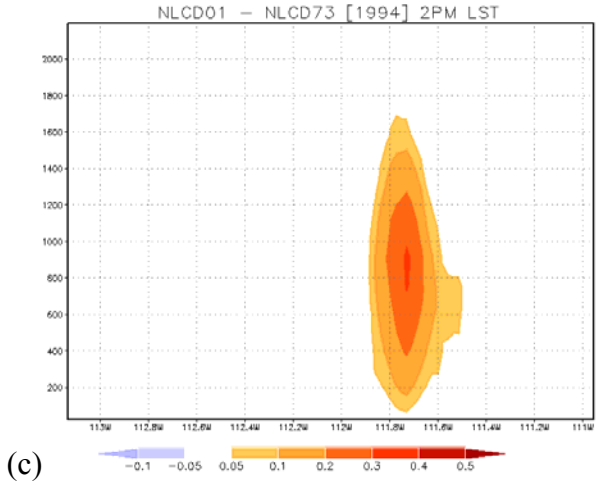

(c)

Figure 8.9 Altitude-longitude cross-section of RAMS simulated monthly averaged w-wind (m s^{-1}) speed difference (NLCD01 – NLCD73) for **(a**) 1979; **(b)** as (a) but for 1989; **(c)** as (a) but for 1994. All calculations are at 14 LST and at 33.4° N.

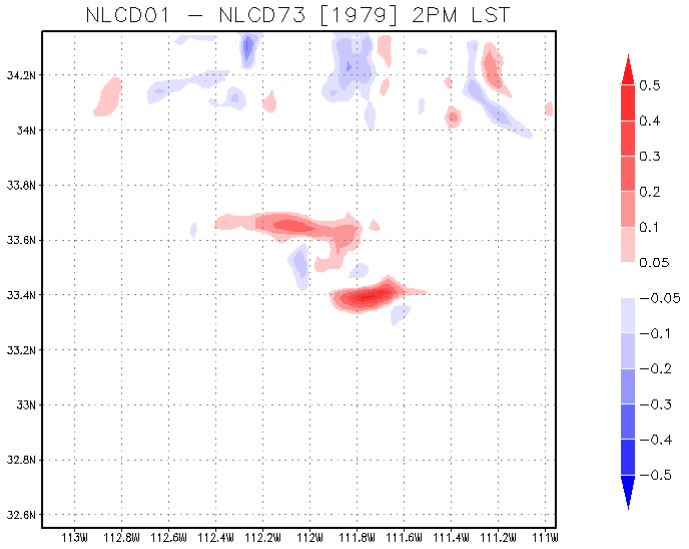

(a)

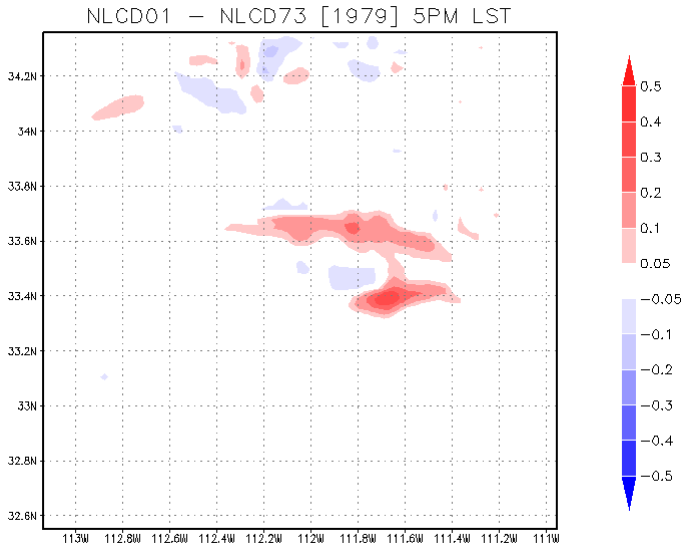

(b)

Figure 8.10 RAMS simulated monthly averaged w-wind (m s^{-1}) speed difference (NLCD01 – NLCD73) at 924-m altitude at **(a)** 14 LST and **(b)** 17 LST, for 1979.

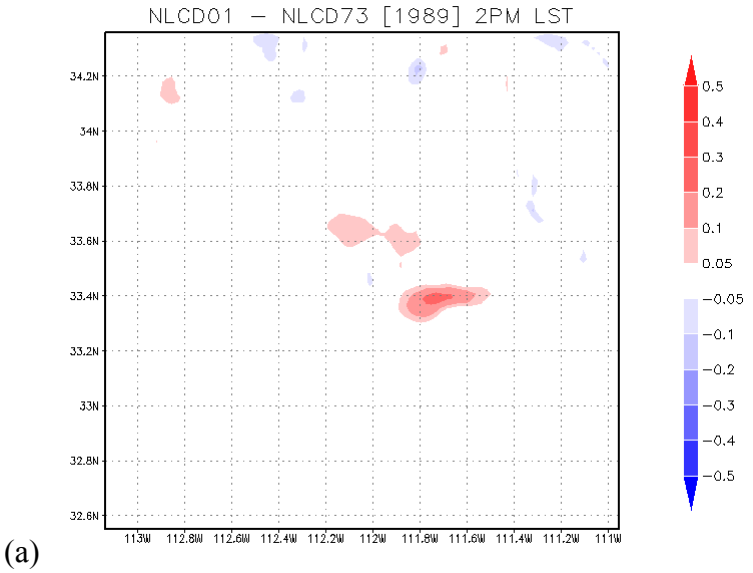

(a)

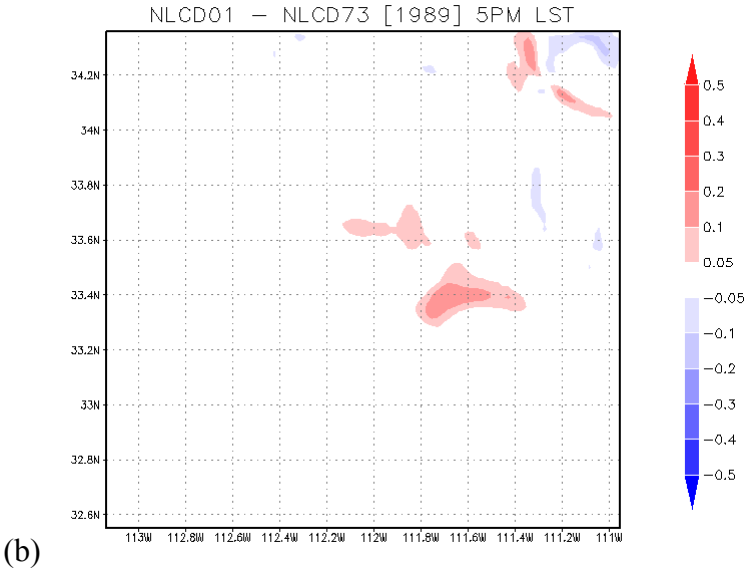

(b)

Figure 8.11: RAMS simulated monthly averaged w-wind (m s^{-1}) speed difference (NLCD01 – NLCD73) at 924-m altitude at **(a)** 14 LST and **(b)** 17 LST, for 1989.

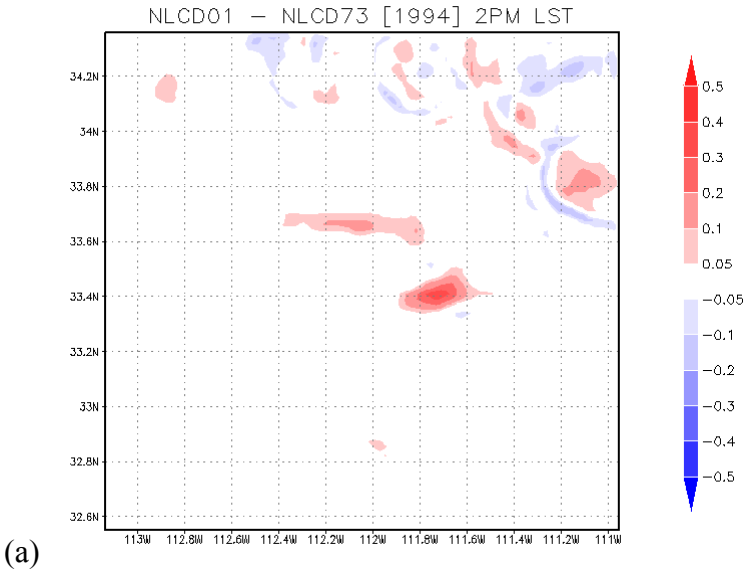

(a)

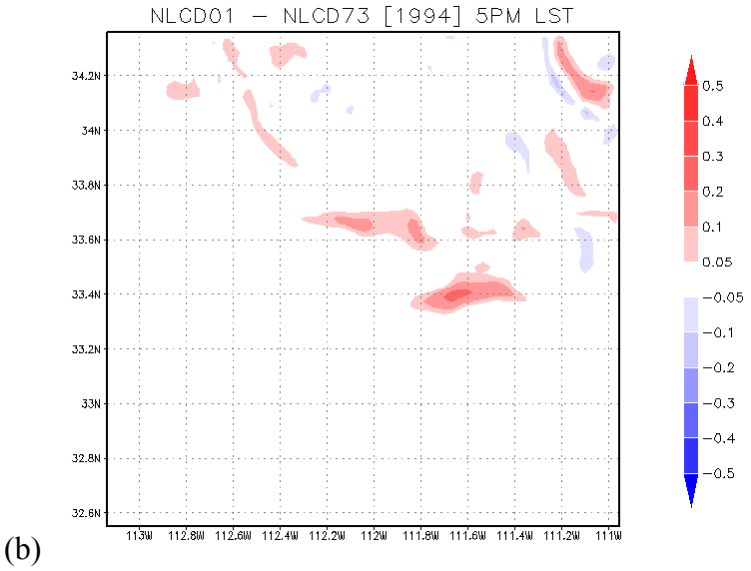

(b)

Figure 8.12 RAMS simulated monthly averaged w-wind (m s^{-1}) speed difference (NLCD01 – NLCD73) at 924-m altitude at **(a)** 14 LST and **(b)** 17 LST, for 1994.

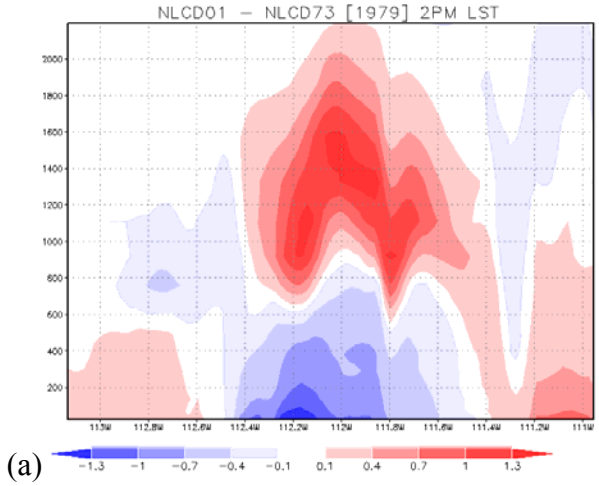

(a)

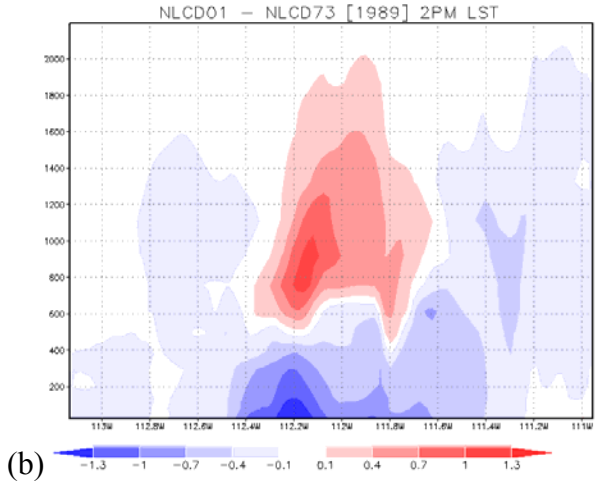

(b)

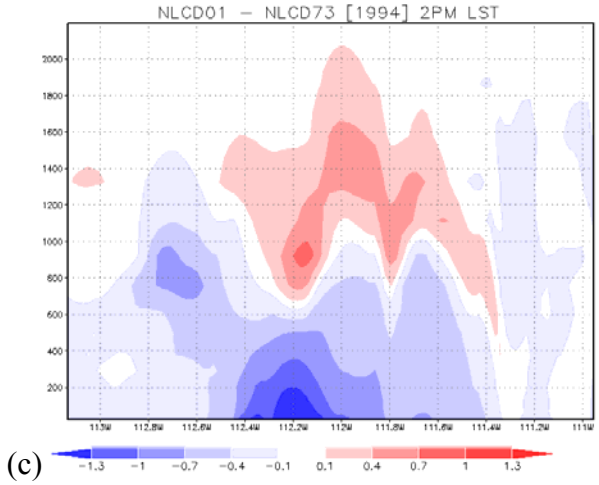

(c)

Figure 8.13 Altitude-longitude cross-section of RAMS simulated monthly averaged water vapor mixing ratio (g kg^{-1}) difference (NLCD01 – NLCD73) for **(a)** 1979; **(b)** as (a) but for 1989; **(c)** as (a) but for 1994. All calculations are at 14 LST and at 33.65° N.

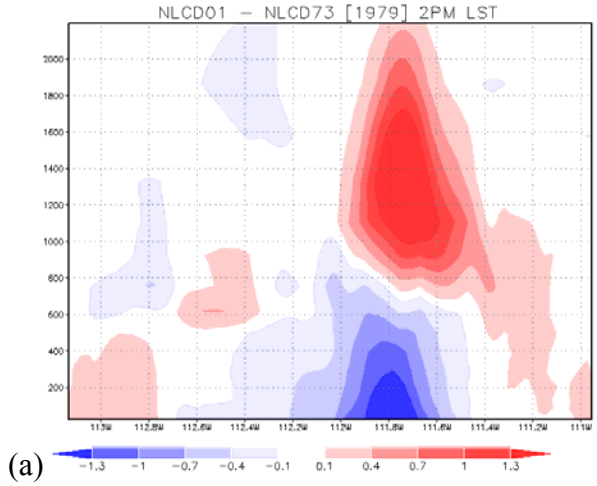

(a)

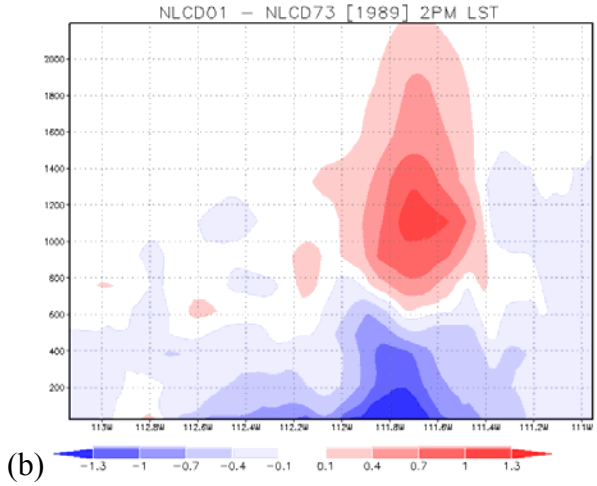

(b)

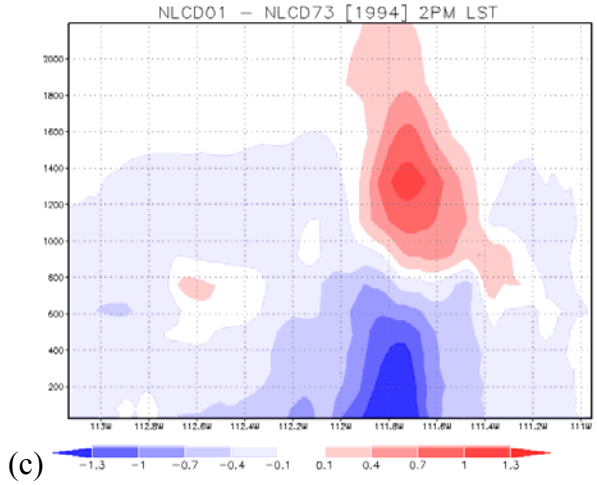

(c)

Figure 8.14 Altitude-longitude cross-section of RAMS simulated monthly averaged water vapor mixing ratio (g kg^{-1}) difference (NLCD01 – NLCD73) for **(a)** 1979; **(b)** as (a) but for 1989; **(c)** as (a) but for 1994. All calculations are at 14 LST and at 33.4° N.

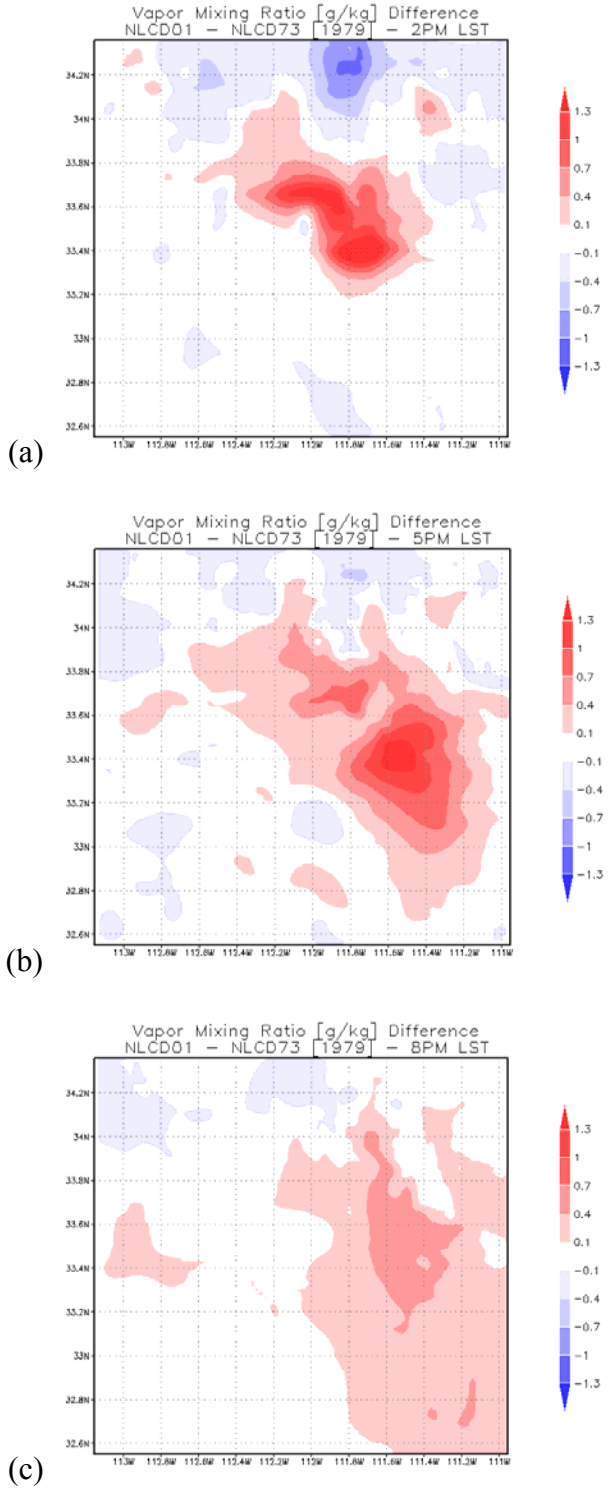

(a)

(b)

(c)

Figure 8.15 RAMS simulated monthly averaged water vapor mixing ratio (g kg^{-1}) difference (NLCD01 – NLCD73) at 1330-m altitude at **(a)** 14 LST, **(b)** 17 LST, and **(c)** 20 LST, for 1979.

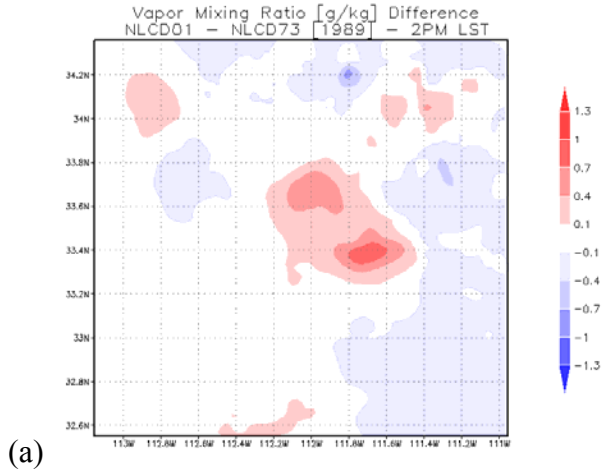

(a)

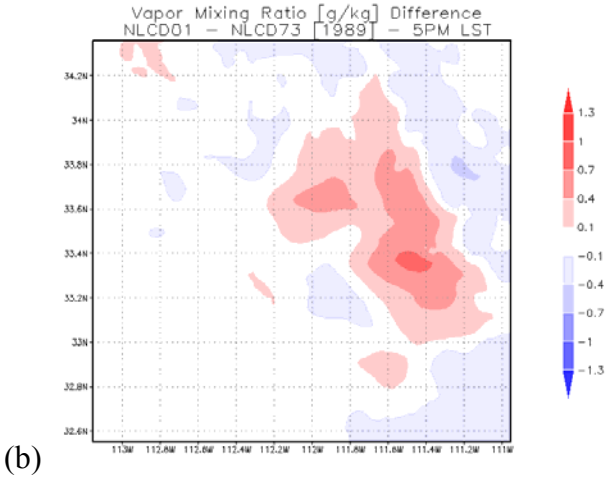

(b)

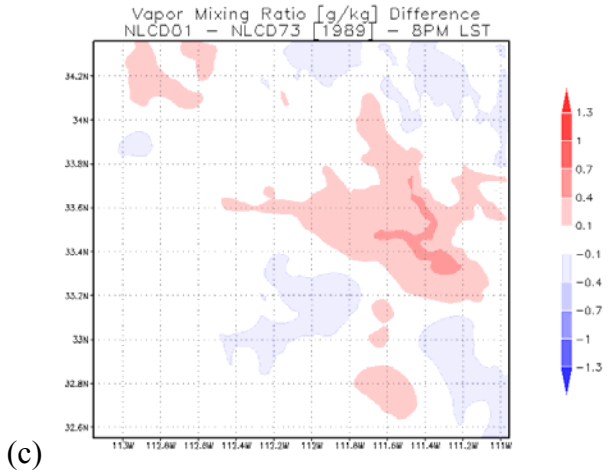

(c)

Figure 8.16 RAMS simulated monthly averaged water vapor mixing ratio (g kg^{-1}) difference (NLCD01 – NLCD73) at 1330-m altitude at **(a)** 14 LST, **(b)** 17 LST, and **(c)** 20 LST, for 1989.

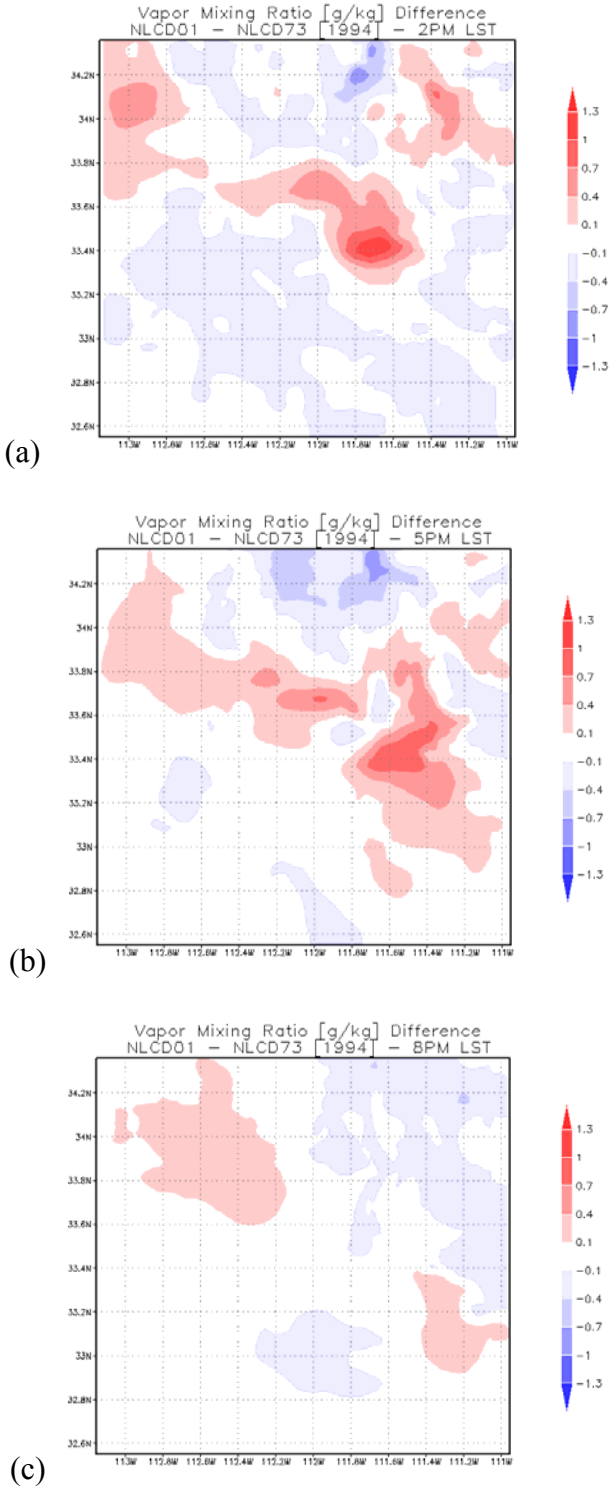

(a)

(b)

(c)

Figure 8.17 RAMS simulated monthly averaged water vapor mixing ratio (g kg^{-1}) difference (NLCD01 – NLCD73) at 1330-m altitude at **(a)** 14 LST, **(b)** 17 LST, and **(c)** 20 LST, for 1994.

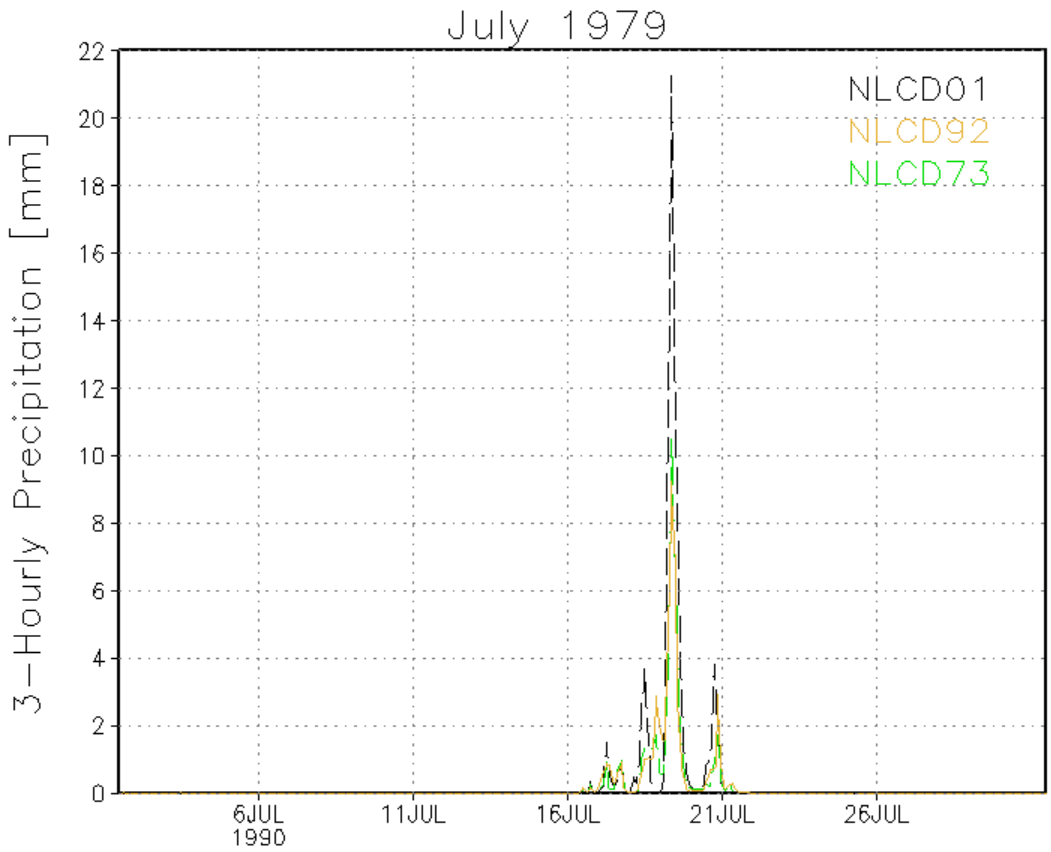

Figure 8.18 RAMS simulated 3-hourly accumulated precipitation for July 1979, for each of the three landscape reconstructions.

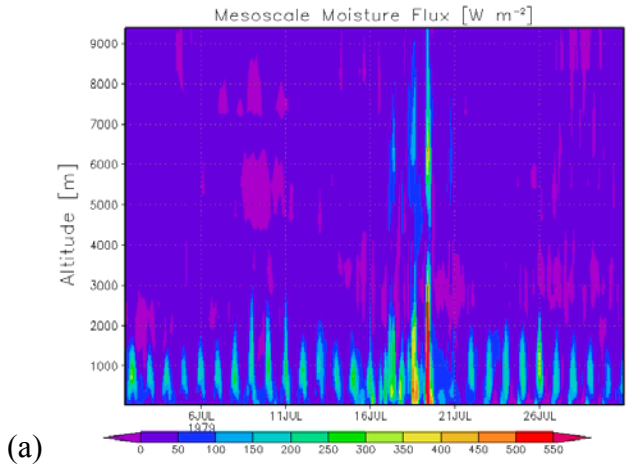

(a)

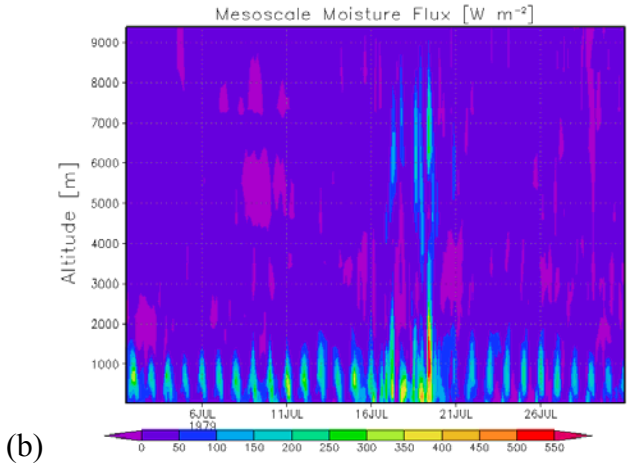

(b)

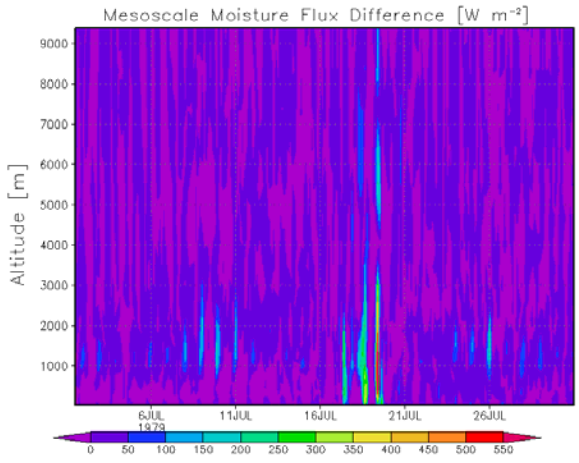

(c)

Figure 8.19 RAMS simulated domain-averaged [lat: 33 to 34/lon: -112.2 to -111.0; See Figure 6.3 [b] for extent of averaging domain] vertical profiles of RAMS simulated mesoscale moisture flux (W m^{-2}) for 1979 for **(a)** NLCD01, **(b)** NLCD73, and **(c)** the NLCD01 – NLCD73 difference.

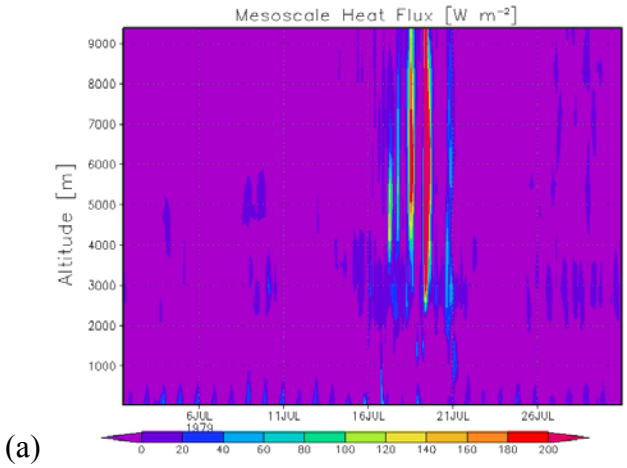

(a)

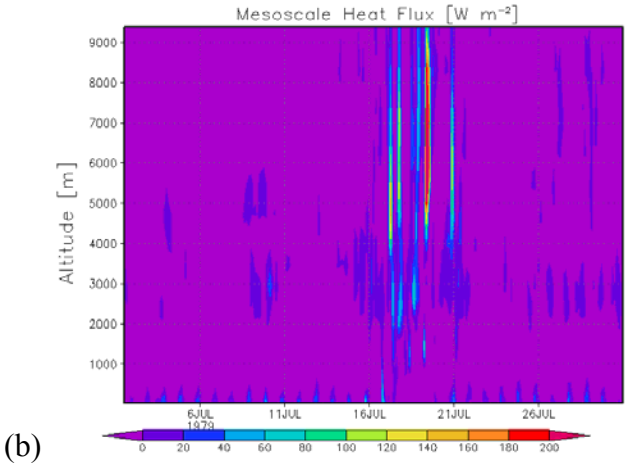

(b)

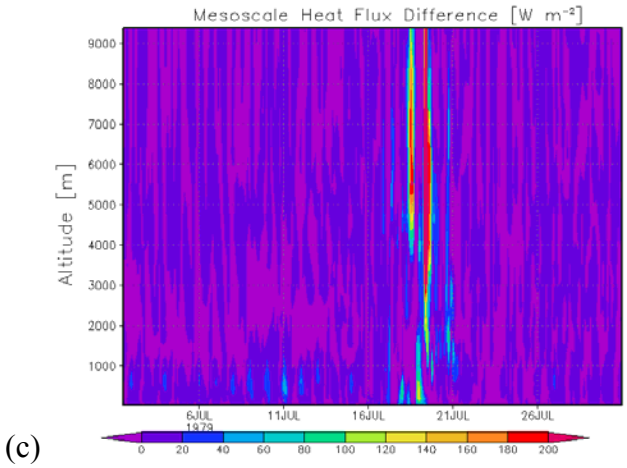

(c)

Figure 8.20 Same as Figure 8.19 but for mesoscale heat flux (W m^{-2}).

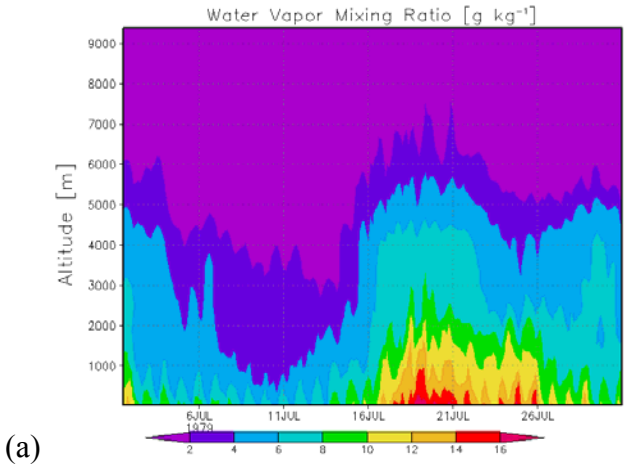

(a)

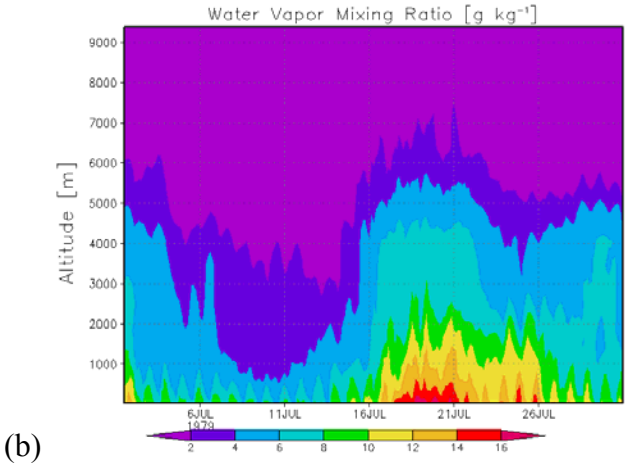

(b)

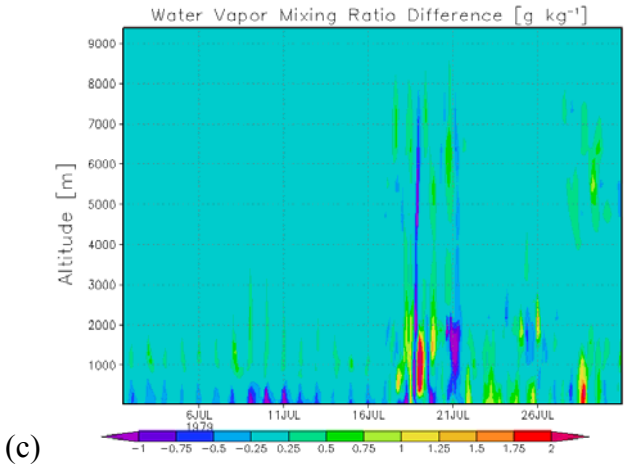

(c)

Figure 8.21 Same as Figure 8.19 but for water vapor mixing ratio (g kg^{-1}).

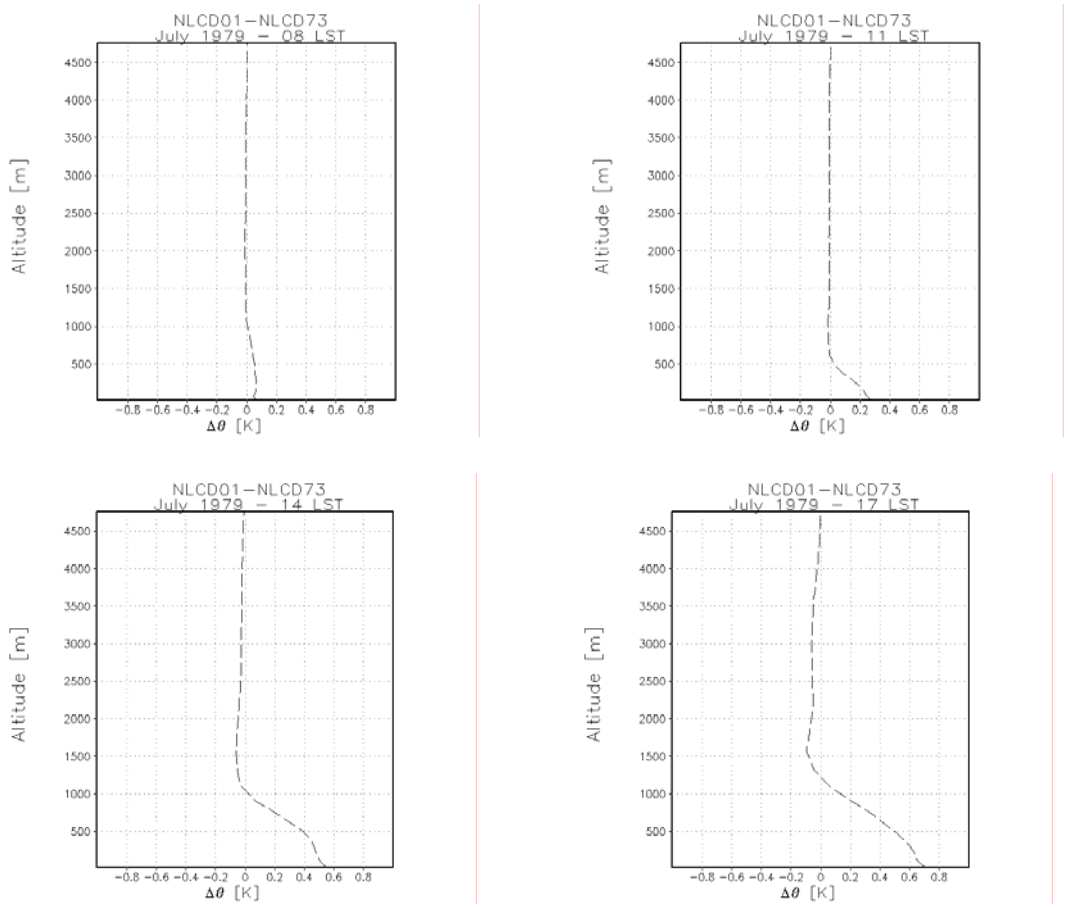

Figure 8.22 RAMS simulated domain-averaged [lat: 33 to 34/lon: -112.2 to -111.0; See Figure 6.20 [b] for extent of averaging domain] diurnal evolution of θ difference for July 1 – 16, 1979. Top left image corresponds to 08 LST; top right image to 11 LST; bottom left image to 14 LST; bottom right image to 17 LST.

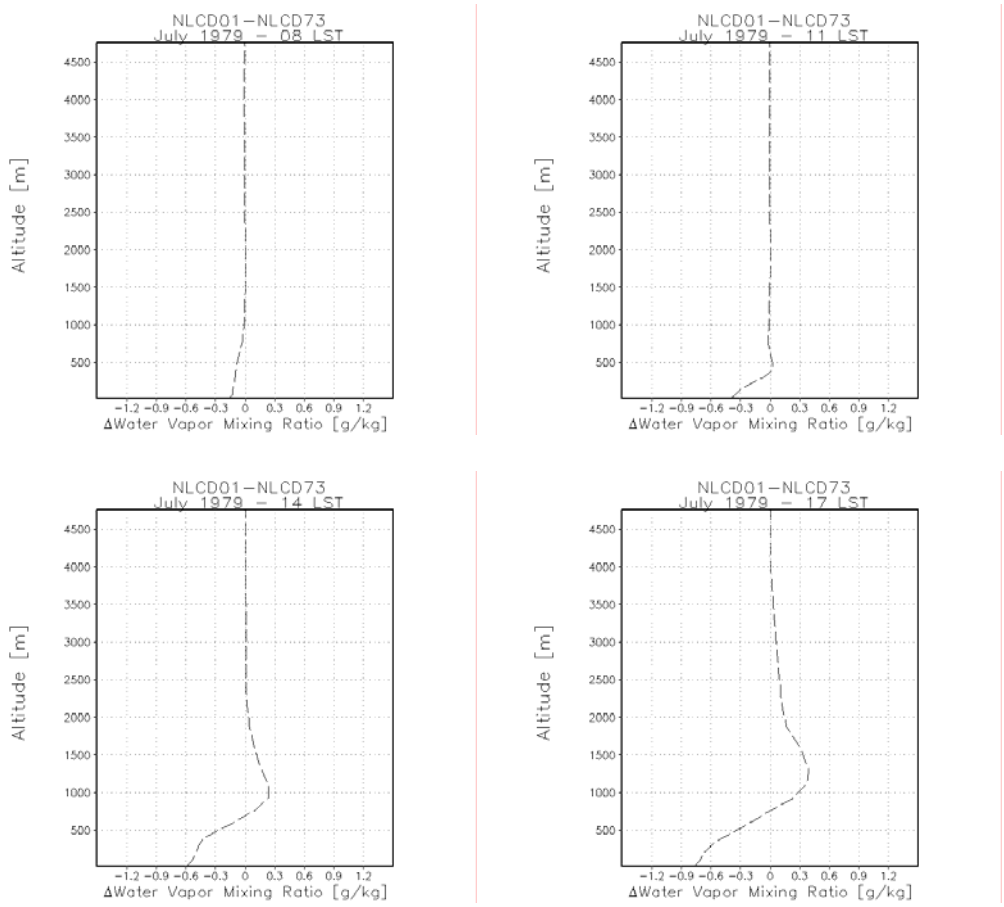

Figure 8.23: Same as Figure 8.22 but for water vapor mixing ratio difference.

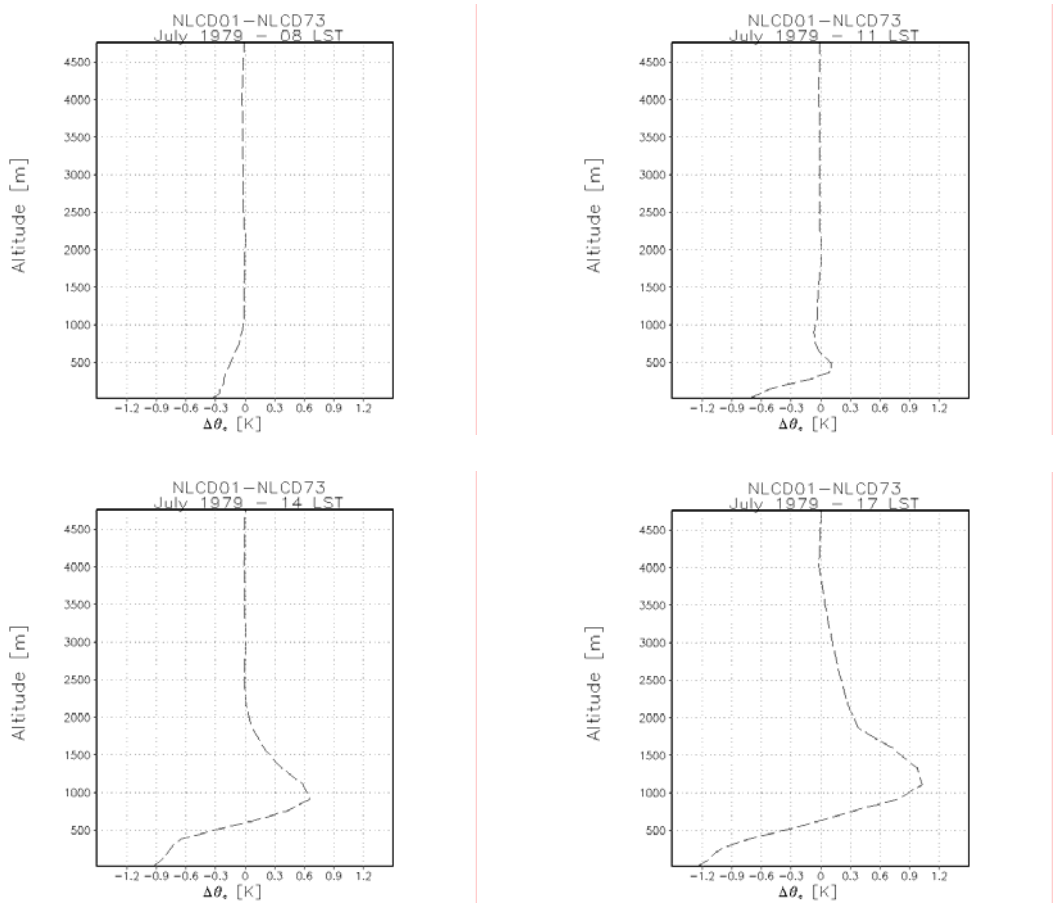

Figure 8.24 Same as Figure 8.22 but for θ_e difference.

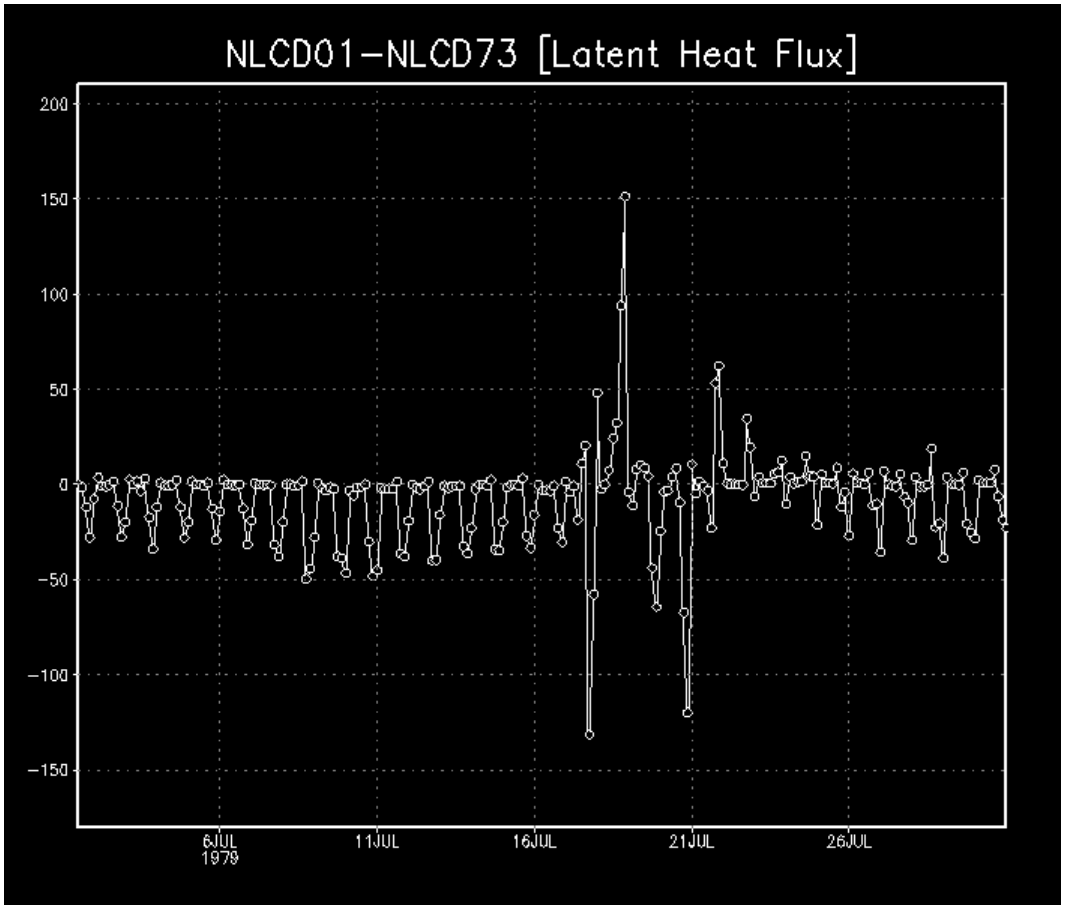

Figure 8.25 RAMS simulated domain-averaged [lat: 33 to 34/lon: -112.2 to -111.0; See Figure 6.3 [b] for extent of averaging domain] latent heat flux (W m^{-2}) difference (NLCD01-NLCD73) for 1979.

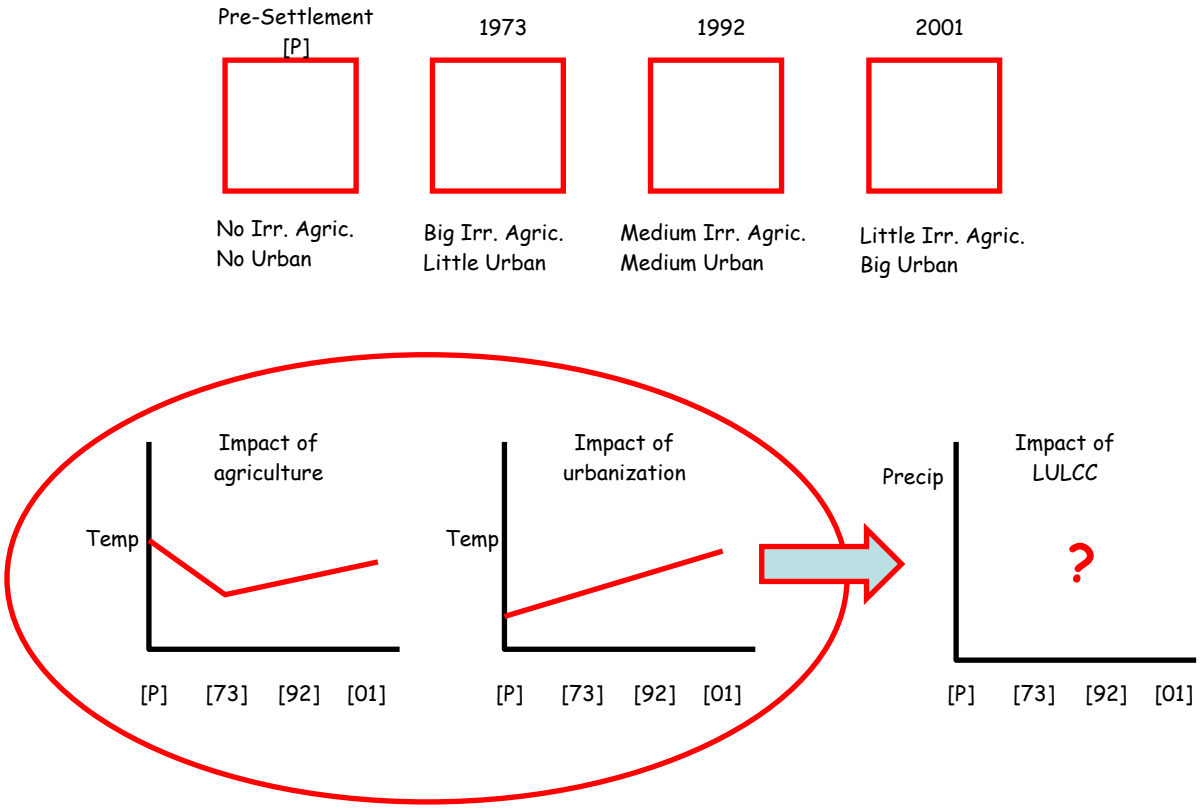

Figure 8.26 Cartoon diagram reflecting principal results. Top row defines extent of the fine grid domain and illustrates, qualitatively, the quantity of irrigated agriculture and urban land (i.e. the two chief landscapes considered in this work) contained therein. The bottom row shows the thermal effect of changing irrigated agriculture (as defined in the top row) and of changing urban land (as defined in the top row). The effect on precipitation is less clear (see text for details).

Curriculum Vita

Matei Georgescu

EDUCATION:

B.S. in Meteorology, Rutgers University, May 1999
M.S. in Environmental Sciences, Rutgers University, January 2003
Ph.D. in Atmospheric Sciences, Rutgers University, May 2008

EMPLOYMENT:

NASA Fellow — 2004 - Present
Rutgers University
Department of Environmental Sciences

Graduate Assistant — 2001-2004
Rutgers University
Department of Environmental Sciences

Teaching Assistant — 1999 – 2001
Rutgers University
Department of Environmental Sciences

REFEREED PUBLICATIONS:

Georgescu, M., G. Miguez-Macho, L. T. Steyaert, and C.P. Weaver, 2008: Sensitivity of summer climate to anthropogenic land cover change over the Greater Phoenix, AZ, Region, *J. Arid Env.,* In Press.

Georgescu, M., C.P. Weaver, R. Avissar, R.L. Walko, and G. Miguez-Macho, 2003: Sensitivity of model-simulated summertime precipitation over the Mississippi River basin to the spatial distribution of initial soil moisture. *J. Geophys. Res.* **108**, 8855, doi:10.1029/2002JD003107.

Harnack, R.P., Apffel, K., Georgescu, M., and Baines, S., 2001: The Determination of Observed Atmospheric Differences Between Heavy and Light Precipitation Events in New Jersey, USA. *International J. of Climatology* , **21**, 1529-1560.